UNIVERSITÉ DE STRASBOURG

THÈSE présentée par :

Vira ZAKUSILOVA

soutenue le : **19 septembre 2022**

pour obtenir le grade de : **Docteur de l'Université de Strasbourg**

Discipline/ Spécialité : **Chimie Physique**

Characterization and Application of Alkanethiolate Self-Assembled Monolayers on Gold-Coated Silicon Detectors for the Metal Sorption

---

THÈSE dirigée par :

BOLTOEVA Maria   Chargée de Recherche, CNRS, University of Strasbourg, France

RAPPORTEURS :

JOHN Jan   Professor, Head of the Department of Nuclear Chemistry, Czech Technical University in Prague, Czech Republic

SCHERER Ulrich W.   Professor, Radiation protection officer at Mannheim University of Applied Sciences, Head of the Institute of Physical Chemistry and Radiochemistry, Mannheim, Germany

AUTRE MEMBERS DU JURY

YENNELLO Sherry J   Regent's Professor of Chemistry, Bright Chair in Nuclear Science, Director of the Cyclotron Institute, Texas A&M University, College Station, United States

OUADI Ali   Ingénieur de Recherche, CNRS, University of Strasbourg, France

ABSTRACT

In the field of superheavy elements, one of the first attempts to use gold-coated silicon was reported during the chemical characterization of element 112, Cn [1, 2]. Better chemical sorption of this element was observed on gold-modified surfaces rather than non-modified ones. In the case of element 113, Nh, an enhanced reactivity towards gold was observed, which prevented the proper chemical characterization of this element [3, 4]. Therefore, a need for new chemically modified gold-coated silicon detectors has emerged. The goal of such detectors is to selectively bind the atoms of interest but with weaker interactions.

Element 109, meitnerium, which is expected to be a member of group 9 of the Periodic Table, has never been chemically characterized before. Therefore, this project aimed to study the adsorption of meitnerium's two closest homologs, namely iridium and rhodium, on functionalized surfaces.

In the first part of this project, the functionalization of gold-coated chips with 1-(11-mercaptoundecyl)imidazole and 12-mercaptododecanoic acid SAMs, as well as the iridium(IV) and rhodium(III) sorption from hydrochloric acid solutions on the functionalized surfaces have been investigated. The functionalized surfaces were characterized off-line via several surface science techniques: atomic force microscopy, nanoprojectile secondary-ion mass spectrometry, X-ray photoelectron spectroscopy, ellipsometry, and instrumental neutron activation analysis. The studied surfaces mimic functionalized gold-coated silicon detectors. The main goal of the devices of such kind is to compare the sorption properties of the superheavy element and its lighter homolog(s) during online cyclotron-based experiments.

In the second part of this project, the sorption of iridium, erbium (non-volatile elements), and astatine (a volatile element) on non-functionalized and thiolate-functionalized gold-coated

silicon detectors have been studied during online cyclotron-based experiments. There is an interest in studying the sorption of iridium because it will help better the understanding of the chemistry of meitnerium in the future. By studying the sorption of iridium, erbium, and astatine, the comparison of the chemical behavior of the members of non-volatile and volatile elements, respectively, was performed. It was found that the detector position and material influence the sorption of these elements within the detector setup.

RESUME

Dans le domaine de la synthèse des éléments super-lourds (Z = 104 et plus lourds) et les études expérimentales de leurs propriétés chimiques et physiques, l'une des premières tentatives d'utilisation de silicium recouvert d'une couche mince d'or a été annoncé lors de la caractérisation chimique de l'élément 112, le copernicium (symbole Cn) [1, 2]. Une meilleure sorption chimique de cet élément a été observée sur les surfaces modifiées à l'or plutôt que sur les surfaces non modifiées. Dans le cas de l'élément 113, le nihonium (symbole Nh), une réactivité accrue *vis-à-vis* de l'or a été observée, ce qui a empêché la caractérisation chimique adéquate de ce nouvel élément [3, 4]. Par conséquent, il faudrait développer de nouveaux détecteurs silicium recouverts d'or modifié chimiquement. Ces détecteurs ont pour le but de lier sélectivement les atomes d'intérêt mais avec des interactions plus faibles.

L'élément 109, le meitnerium, qui devrait être un membre du groupe 9 du tableau périodique des éléments, n'a jamais été caractérisé chimiquement auparavant. Par conséquent, ce travail de thèse de doctorat vise à étudier l'adsorption de deux homologues les plus proches du meitnerium, l'iridium et le rhodium, sur des surfaces fonctionnalisées.

Dans la première partie de cette thèse, nous avons réalisé la fonctionnalisation de puces silicium recouvertes d'or avec des monocouches auto-assemblées de molécules organiques, 1-(11-mercaptoundecyl)imidazole ou d'acide 12-mercaptodecanoïque. Les surfaces fonctionnalisées ont été caractérisées par plusieurs techniques d'analyse de surface, notamment par microscopie à force atomique, spectrométrie de masse à ions secondaires par nanopjectiles, spectroscopie photoélectronique à rayons X, ellipsométrie et analyse instrumentale par activation neutronique. Puis la sorption d'iridium(IV) et de rhodium(III) à partir de solutions d'acide chlorhydrique sur les surfaces fonctionnalisées a été étudiée. Les surfaces étudiées donc imitent des détecteurs siliciums recouverts d'or fonctionnalisé.

L'objectif principal des dispositifs de ce type est de comparer les propriétés de sorption de l'élément super-lourd et de son ou ses homologues plus légers lors d'expériences online au cyclotron.

Dans la deuxième partie de ce travail, la sorption de l'iridium et de l'erbium (éléments non volatils) ainsi que de l'astate (élément volatil) sur des détecteurs silicium recouverts d'or non fonctionnalisés et fonctionnalisés par des thionates a été étudiée au cours d'expériences online au cyclotron. Nous nous intéressons à l'étude de la sorption de l'iridium car elle permettra à l'avenir de mieux comprendre la chimie du meitnerium. Les résultats de l'étude de la sorption de l'iridium, de l'erbium et de l'astate nous ont permis de comparer le comportement chimique des membres des éléments non volatils et volatils, respectivement. Il a été constaté que la position et le matériau du détecteur influencent la sorption de ces éléments dans la configuration du détecteur.

CHAPITRE I

INTRODUCTION

1.2   Monocouches auto-assemblées de molécules organiques

Une approche bien connue de la fonctionnalisation de métaux, des oxydes métalliques et des semi-conducteurs est la formation de monocouches auto-assemblées (self-assembled monolayers en anglais, SAMs) à leur surface [5-10]. Les SAMs sont des arrangements de molécules qui peuvent être adsorbées spontanément sur des surfaces solides à partir d'une solution ou d'une phase gazeuse [6].

Les molécules de SAM sont composées de trois parties : un groupement de "tête" qui s'adsorbe en surface, une chaîne "séparatrices" (chaine aliphatique) et un groupement

terminal fonctionnel [6]. Différents groupes de tête peuvent se lier à des métaux, oxydes métalliques et semi-conducteurs spécifiques [7-10].

Les SAM d'alcanethiolate sur les surfaces de métaux tels que or, argent, cuivre, palladium, platine, nickel constituent la classe de SAMs la plus largement étudiée et la plus connue [5-10].
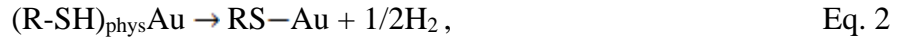
Parmi tous les métaux cités, la préférence est donnée à l'or (Au), en particulier Au(111). Comme les métaux cubiques à faces centrées orientés (111) ont l'énergie libre de surface la plus faible, ces surfaces sont plus stables, contrairement aux surfaces métalliques orientées (100) qui subissent des reconstructions massives [11, 12]. L'or est le métal le plus utilisé lors de l'adsorption de SAMs car il est facile à obtenir sous forme de couches minces, raisonnablement inerte, et forme des SAMs de bonne qualité [5, 7].

Les thiols peuvent former de fortes liaisons covalentes thiolate-Au de 50 kcal/mol pendant la formation des SAMs [6], et ces SAMs peuvent être facilement préparés en phase liquide par l'immersion d'un substrat dans une solution éthanolique de thiol pendant 24 heures [6, 7].

L'adsorption des thiols sur la surface de l'or se produit en deux étapes, commençant par la physisorption suivie de la chimisorption illustrée par l'équation 1 et l'équation 2, respectivement [6]. Au cours de cette dernière, une molécule de thiol, à savoir R-SH, est déprotonée et se transforme en un thiolate (RS-Au) [6].

Le processus d'adsorption peut être décrit comme suit :

$$R\text{-}SH + Au \rightarrow (R\text{-}SH)_{phys}Au \qquad\qquad \text{Eq. 1}$$

$$(R\text{-}SH)_{phys}Au \rightarrow RS-Au + 1/2H_2 \,, \qquad\qquad \text{Eq. 2}$$

où R est un radical organique, dans le cas des alcanethiolates, $R=CH_3(CH_2)_n$, où n est le nombre d'atomes de carbone présents dans une molécule [6].

Le schéma de l'auto-assemblage des alcanes thiolates est présenté dans la Figure 1 [6]. Il est important d'effectuer le dépôt de SAMs pendant 24 heures en raison de plusieurs étapes qui ont lieu pendant l'auto-assemblage. Comme il a été dit, la physisorption se produit d'abord, puis, au début de la chimisorption, les molécules sont principalement couchées. Au fil du temps, elles se redressent et finissent par former des molécules bien ordonnées dans une configuration dense [6].
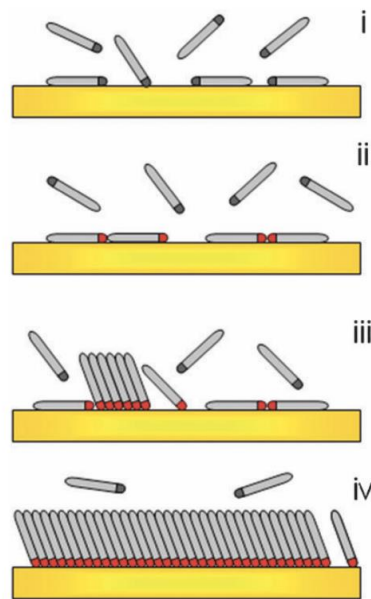
Figure 1. Schéma de la formation de SAMs d'alcanethiolate sur Au(111) : physisorption (i), formation de la phase de dépôt (ii), nucléation de la phase de maintien (iii), achèvement de la phase de maintien (iv). Illustration utilisée avec la permission de la réf. [6]

La grande affinité des thiols pour l'Au permet de créer des substrats organiques bien définis avec des fonctionnalités chimiques utiles et des propriétés qui peuvent être modifiées à l'avance en fonction de l'application [7].

L'alcanethiol à terminaison imidazole, 1-(11-mercaptoundecyl)imidazole (Im-C$_{11}$-SH), étudié dans cette thèse a été choisi pour plusieurs raisons. L'objectif était de générer un substrat à base de SAMs alcanethiolate ayant des propriétés prédéfinies de fixation de Ir et Rh à partir de solutions d'acide chlorhydrique. Tout d'abord, il est bien connu que les liquides ioniques à base d'imidazolium ont déjà été utilisés dans l'extraction de Ir(IV) à partir de solutions d'acide chlorhydrique, atteignant des rapports de distribution élevés allant jusqu'à 71,4 [13]. Nous avons supposé que l'alcanethiol à terminaison imidazole serait également efficace pour la fixation de Ir(IV). D'autre part, le Rh(III) est extrait par les liquides ioniques à base d'imidazolium à un degré moindre, et les efficacités d'extraction ont été rapportées comme étant inférieures à 10% [14]. Néanmoins, l'idée était de comparer les efficacités de sorption de ces deux métaux en utilisant les SAMs Im-C$_{11}$-SH. Deuxièmement, Im-C$_{11}$-SH est un composé disponible dans le commerce qui simplifie la procédure de préparation des SAMs. Troisièmement, la revue de la littérature a montré que plusieurs tentatives réussies ont déjà été faites pour préparer des SAMs d'Im-C$_{11}$-SH sur des surfaces d'or [15-18].

Le second thiol, l'acide 12-mercaptododécanoïque (MDDA), a été choisi pour comparer la sorption des métaux sur des SAMs avec différents groupes fonctionnels.

1.3   Objectif

Dans la première partie de ce travail de thèse, la fonctionnalisation de puces recouvertes d'or avec des SAMs Im-C$_{11}$-SH et MDDA, ainsi que la sorption de Ir(IV) et Rh(III) de solutions d'acide chlorhydrique sur des SAMs Im-C$_{11}$-SH ont été étudiées. Les

résultats de cette étude ont été importants pour la conception de nouveaux détecteurs en silicium recouverts d'or fonctionnalisé.

Dans la deuxième partie de cette thèse, les détecteurs cités ont été utilisés lors d'expériences online au cyclotron visant à étudier la sorption de l'iridium, de l'erbium et de l'astate sur des détecteurs en silicium non fonctionnalisés et fonctionnalisés.

Les résultats de cette étude pourront éventuellement être utilisés pour développer un système chimique adapté à la caractérisation chimique du Mt dans le futur.

CHAPITRE III

RESULTATS ET DISCUSSION

3.1   Caractérisation de Im-C$_{11}$-SH et MDAA SAMs sur les surfaces recouvertes d'or

Les techniques de caractérisation de surface utilisées pour mesurer la rugosité, la couverture de surface, l'état chimique des SAMs, la cinétique de dégradation des SAMs, l'épaisseur des SAMs et de la saturation de surface ont décrites. Les détails techniques sont fournis dans le Chapitre 2.

3.3   Conclusion

Dans ce travail, la caractérisation de la surface de puces de silicium recouvertes d'or et fonctionnalisées   avec   des   monocouches   auto-assemblées   de   1-(11-mercaptoundécyl)imidazole et d'acide 12-mercaptodécanoïque a été réalisée (Figure 2).

Figure 2. Représentation schématique du système étudié.

Pour les SAMs Im-C_{11}-SH, l'AFM a révélé que le dépôt des SAMs, ainsi que le traitement liquide-UVPO, n'affectent pas la morphologie et la topologie de la surface. Les valeurs de rugosité de surface restent de l'ordre de 1,20-1,25 nm. Les NP-SIM ont montré que la plus grande couverture de surface de (99 ± 6) % a été atteinte lorsque le dépôt de SAMs a été effectué à partir d'une solution 5mM Im-C_{11}-SH. Le nettoyage préalable des puces de silicium recouvertes d'or à l'aide du traitement liquide-UVPO a permis d'utiliser des surfaces exemptes de nombreux contaminants. L'étude de stabilité par la technique XPS des SAMs d'Im-C_{11}-SH et de MDDA dans des conditions ambiantes de laboratoire a indiqué que les puces recouvertes d'or fonctionnalisées restent stables pendant au moins un mois après leur stockage dans des plateaux de support de plaquettes fermés, enveloppés de papier d'aluminium. Il est donc possible d'utiliser les SAMs d'Im-C_{11}-SH et de MDDA pour la fonctionnalisation de détecteurs en silicium recouverts d'or utilisés lors d'expériences online au cyclotron. De plus, le traitement UVPO liquide s'est avéré être une technique efficace pour régénérer les surfaces en or recouvertes de SAMs Im-C_{11}-SH. Enfin, les résultats de l'ellipsométrie ont prouvé la présence d'une monocouche de thiolate unique d'une épaisseur de $1,690 \pm 0,014$ nm sur la surface de l'or. Après une semaine de stockage des échantillons, l'épaisseur est restée relativement la même, ce qui exclut les processus de dégradation pendant

cette période. NP-SIMS et INAA ont illustré la sorption réussie de Rh(III) et Ir(IV),

respectivement, sur les puces pré-nettoyées et fonctionnalisées recouvertes d'or. La couverture

des SAMs Im-C$_{11}$-SH avec Rh(III) a été mesurée à (81.3 ± 3.8)% en utilisant NP-SIMS. Les

résultats de l'INAA ont permis de conclure que Ir(IV) peut être adsorbé à partir de solutions

de 5,4 μM de Ir(IV) dans du HCl 0,55 M sur des puces de silicium recouvertes d'or

fonctionnalisées avec des SAMs Im-C$_{11}$-SH et des puces de verre recouvertes d'or

fonctionnalisées avec des SAMs MDDA avec la saturation de surface de (77 ± 12)% et

(84 ± 16)%, respectivement (Figure 3).
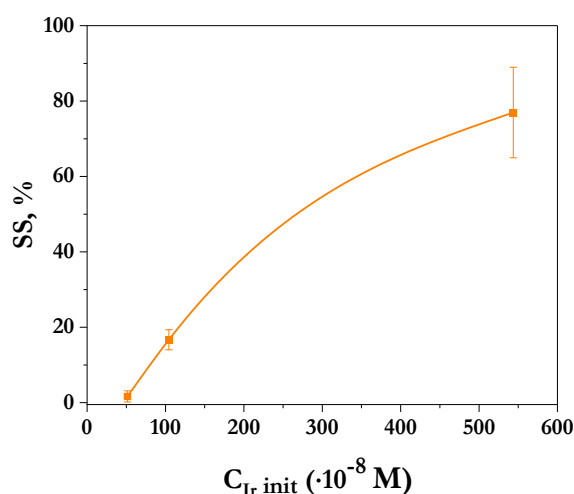
Figure 3 La saturation de surface des SAMs Im-C$_{11}$-SH avec Ir (IV) en fonction de la
concentration initiale d'Ir (IV) dans des solutions de HCl 0,55 M.

La sensibilité observée des puces recouvertes d'or fonctionnalisé à la sorption de

Rh(III) et Ir(IV) permet d'utiliser les détecteurs en silicium recouverts d'or fonctionnalisé lors

d'expériences online au cyclotron.

3.4   Expérience online au cyclotron

Les résultats de l'expérience ont porté sur trois réactions de fusion-évaporation :

^{118}Sn(^{40}Ar, 5n)^{153}Er, ^{165}Ho(^{40}Ar, 5n)^{200}At, and ^{141}Pr(^{40}Ar, 5n)^{176}Ir en utilisant des détecteurs

en silicium non fonctionnalisés et fonctionnalisés sont discutés dans ce chapitre. Les détails des réactions nucléaires réalisées ainsi que les détails techniques du dispositif expérimental sont abordés dans la section 2.3.3.

3.4.1   Détection de radionucléides sur des détecteurs en silicium non fonctionnalisés et fonctionnalisés.

L'effet de la position du détecteur dans la chambre de détection et du matériau du détecteur sur les taux de^{152,153}Er, $^{199-201}$At, and $^{173-176}$Ir été étudié (Figure 4).
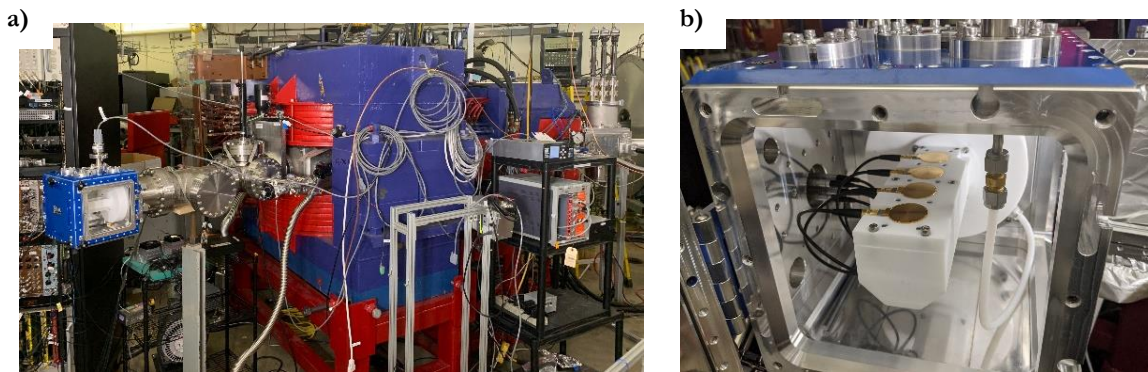
Figure 4 (a) The sRTC installed on the AGGIE separator. (b) The detectors are installed inside the sRTC.

L'effet de la position du détecteur dans la chambre du détecteur et du matériau Les matériaux testés étaient le silicium nu (Bare Si), le silicium recouvert d'or (Si+Au), le silicium recouvert d'or fonctionnalisé avec des SAMs Im-C$_{11}$-SH (C$_{11}$-Im), et le silicium recouvert d'or fonctionnalisé avec des SAMs MDDA (MDAA). Quatre configurations: A, B, C et D présentées sur la Figure 5 ont été testées en faisant passer les détecteurs par chaque position à l'intérieur de la chambre de détection. Ainsi, chaque détecteur a eu la possibilité d'être dans chaque position une fois.
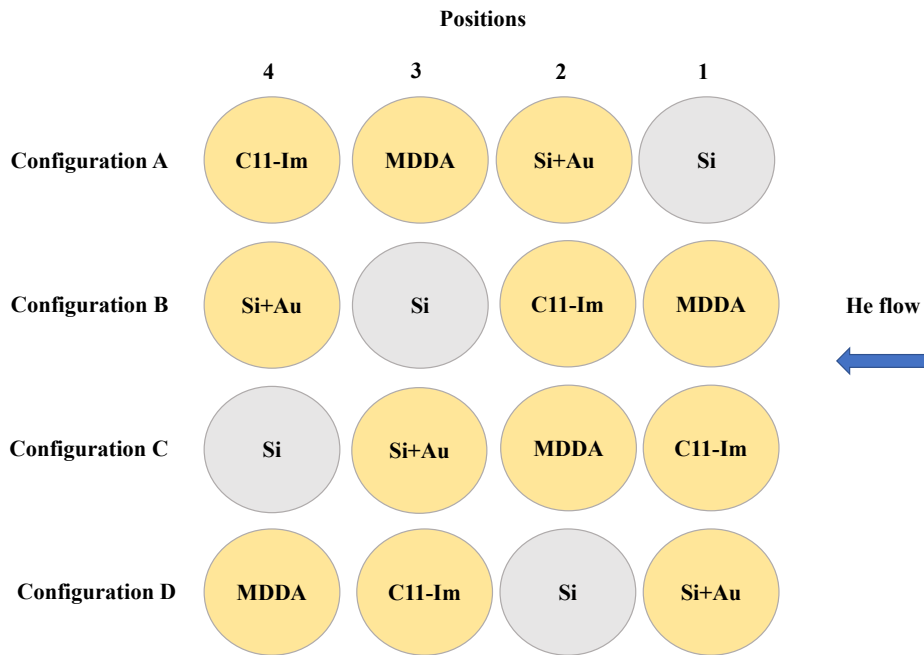
Figure 5. A schematic diagram of four configurations tested during the experiment. The blue arrow shows the entrance of the sRTC.

3.4.1.2. Conclusions

Des résultats prometteurs ont été obtenus lors de la production de ^{152,153}Er, $^{199-201}$At, et $^{173-176}$Ir qui ont démontré que le changement de position et de matériau du détecteur modifie la sorption du nucléide (Figure 6).
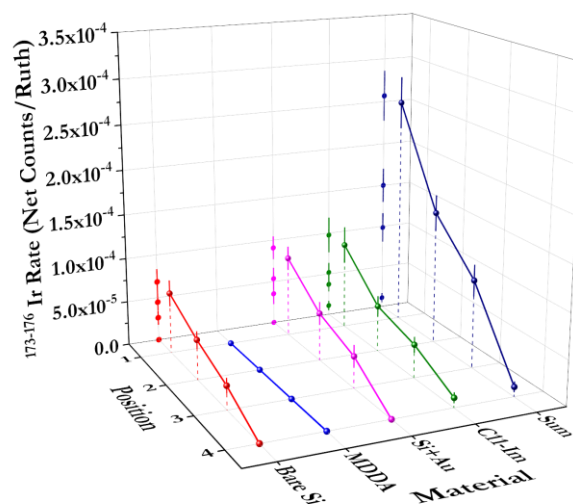

Figure 6. Graphique 3D pour l'activité de $^{173-176}$Ir en fonction de la position du détecteur et de matériaux de détecteur.

Le taux le plus élevé de ^{152,153}Er a été observé sur le détecteur en silicium recouvert d'or et sur les détecteurs en silicium nu. Le taux le plus élevé de ^{199,200,201}At a été observé sur le détecteur recouvert d'or, alors que les autres ont produit une efficacité égale. Pour $^{173-176}$Ir, tous les matériaux ont produit une efficacité égale. L'étude du comportement chimique de ^{152,153}Er, $^{199-201}$At et $^{173-176}$Ir produits online a confirmé le caractère non volatil de Er et Ir et le caractère volatil d'At (Figure 7a). Elle a également révélé que les détecteurs en première position recueillaient la pluralité du produit. L'activité totale était constante quelle que soit la configuration (Figure 7b).
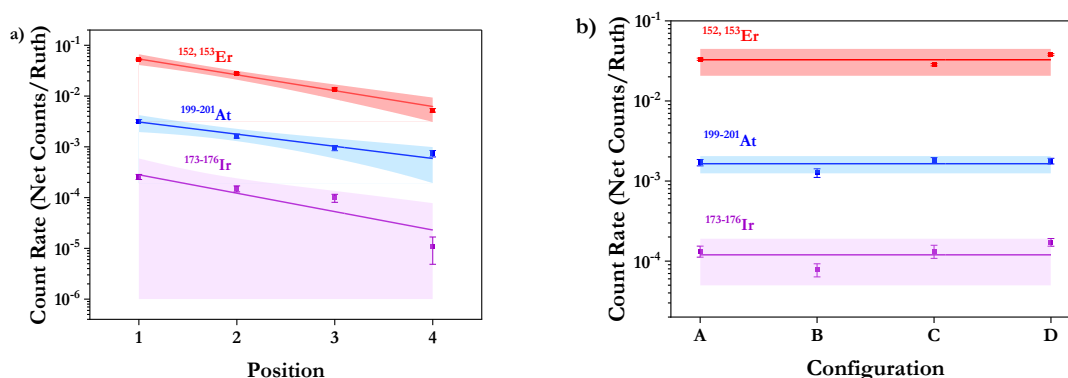
Figure 7. Taux de comptage pour $^{173-176}$Ir, ^{152,153}Er, et $^{199-201}$At en fonction de: a) la position de détecteur; b) la configuration de détecteur.

La spectroscopie alpha a démontré que la fonctionnalisation de la surface du détecteur ainsi que son utilisation pendant les expériences online au cyclotron n'entraînent pas une dégradation de la résolution du détecteur, ce qui permet de les réutiliser.

CHAPITRE IV

CONCLUSIONS

Dans la première partie de cette thèse, la caractérisation des SAMs Im-C$_{11}$-SH et MDDA sur des substrats recouverts d'or a été réalisée en utilisant différentes techniques de

science des surfaces. La morphologie et la topologie de la surface des substrats d'or fonctionnalisés n'ont pas été affectées par le dépôt de SAMs d'Im-C$_{11}$-SH et le traitement liquide-UVPO utilisé pour pré-nettoyer les substrats ou enlever les SAMs. Cette découverte faite avec l'AFM permet de réutiliser plusieurs fois les substrats recouverts d'or sans en altérer les propriétés. L'optimisation de la procédure de dépôt des SAMs a révélé que la plus grande couverture de surface de $(99 \pm 6)\%$ peut être atteinte lorsque des solutions éthanoliques de thiol 5mM sont utilisées pour préparer les SAMs de thiolate sur l'or. Les SAMs d'Im-C$_{11}$-SH et de MDDA se sont révélées stables pendant au moins un mois après leur stockage dans des plateaux de support de plaquettes fermés, enveloppés de papier d'aluminium. Ce résultat important a permis d'utiliser les SAMs d'Im-C$_{11}$-SH et de MDDA pour la fonctionnalisation de détecteurs en silicium recouverts d'or utilisés lors d'expériences cyclotron online qui peuvent durer jusqu'à un mois. L'épaisseur obtenue des SAMs Im-C$_{11}$-SH a prouvé la présence d'une monocouche de thiolate sur la surface de l'or. Les résultats positifs ont été obtenus lors des études de sorption de Ir(IV) et Rh(III) à partir de solutions d'acide chlorhydrique. La couverture des SAMs Im-C$_{11}$-SH avec Rh(III) a été mesurée à $(81.3 \pm 3.8)\%$ en utilisant NP-SIMS. Les résultats INAA ont permis de conclure que Ir(IV) peut être adsorbé sur les SAMs Im-C$_{11}$-SH et MDDA avec la saturation de surface de $(77 \pm 12)\%$ et $(84 \pm 16)\%$, respectivement. Sachant que les puces recouvertes d'or fonctionnalisées sont sensibles à la sorption de Ir(IV) et Rh(III), nous pouvons supposer que les SAMs nommées déposées sur des détecteurs en silicium recouverts d'or seraient efficaces pour fixer les éléments produits online dans la phase gazeuse pendant les expériences basées sur le cyclotron.

Dans la deuxième partie de cette thèse, deux expériences basées sur le cyclotron ont été réalisées pour tester la nouvelle configuration du détecteur. Les résultats de la deuxième expérience ont été décrits en détail dans cette dissertation. Le sRTC a été conçu et utilisé pour

la première fois pour étudier la chimie des éléments produits online, tels que Ir, Er et At. La fenêtre du sRTC pouvait maintenir une différence de pression d'environ 350 Torr. En raison de plusieurs problèmes techniques, le taux de comptage de Ir était nettement inférieur à celui de Er et At. L'efficacité des surfaces à fonction thiolate dans l'adsorption des éléments s'est avérée comparable à celle des détecteurs en Si nu et en Si recouvert d'or. Des résultats prometteurs ont été obtenus lors de l'étude chimique de ^{152,153}Er, $^{199-201}$At, et $^{173-176}$Ir démontrant le rôle de la position du détecteur et de son revêtement sur la sorption du nucléide. Une diminution exponentielle du taux de comptage en fonction de la position du détecteur a été observée pour les nucléides cités. La distribution distincte des éléments volatils et non volatils dans la configuration du détecteur a été obtenue. La résolution des détecteurs est restée dans la même gamme après le dépôt des SAMs ainsi qu'après leur application lors d'expériences online au cyclotron. Cela permet d'utiliser les détecteurs nommés plusieurs fois à l'avenir.

Dans l'ensemble, le système de détection conçu peut être potentiellement appliqué à l'avenir pour étudier les propriétés d'adsorption des éléments superlourds produits online et les comparer à celles de leurs homologues plus légers.

CHAPITRE V

PERSPECTIVES

Malgré les résultats prometteurs obtenus lors de la première tentative d'utilisation des détecteurs en silicium recouverts d'or fonctionnalisés au thiolate dans des expériences basées sur le cyclotron, plusieurs améliorations peuvent être apportées. Tout d'abord, une nouvelle source d'alimentation électrique achetée après l'expérience aurait permis d'augmenter le courant sur l'aimant Q1. À son tour, cela aurait amélioré la concentration des produits dans le sRTC, par conséquent, le taux de comptage de l'Ir produit en ligne aurait pu être augmenté.

Deuxièmement, la taille de l'entonnoir du sRTC peut être diminuée, ce qui réduira la distribution des ions d'intérêt produits et augmentera la probabilité de leur détection sur les détecteurs situés à l'extrémité de la chambre de détection. Troisièmement, les études chimiques à l'intérieur du sRTC ont été menées à température ambiante. À l'avenir, l'effet d'autres températures ou du gradient de température à l'intérieur du dispositif de détection pourrait être étudié. La consommation de gaz He, qui était de 500 à 1800 centimètres cubes standard par minute, peut être réduite. Une meilleure conception de la boîte sRTC peut éliminer les fuites de gaz He tout au long d'une expérience. Enfin, la recherche de molécules potentielles (par exemple, des thiols basés sur des éthers couronnes) qui lieront sélectivement un élément par rapport à un autre peut être effectuée.

Le doctorant suivant dans notre groupe étudiera la sorption du polonium sur des détecteurs en silicium recouverts d'or fonctionnalisés en phase gazeuse. Le choix de l'élément a été dicté par son rapport de branchement alpha élevé. L'étudiant va fonctionnaliser les surfaces avec des molécules de dithiol qui sont potentiellement efficaces pour sorber le polonium.

REFERENCES

[1]   R. Eichler *et al.*, Chemical Characterization of Element 112, Nature **447**, 72 (2007). doi:10.1038/nature05761

[2]   R. Eichler *et al.*, Thermochemical and Physical Properties of Element 112, Angew. Chem. Int. Ed. **47**, 3262 (2008). doi:10.1002/anie.200705019

[3]   S. N. Dmitriev *et al.*, Pioneering Experiments on the Chemical Properties of Element 113, Mendeleev Commun. **24**, 253 (2014). doi:10.1016/j.mencom.2014.09.001

[4]   A. Yakushev *et al.*, First Study on Nihonium (Nh, Element 113) Chemistry at TASCA, Front. Chem. **9**, 1 (2021). doi:10.3389/fchem.2021.753738

[5]   C. Vericat, M. E. Vela, G. Corthey, E. Pensa, E. Cortés, M. H. Fonticelli, F. Ibañez, G. E. Benitez, P. Carro, and R. C. Salvarezza, Self-assembled Monolayers of Thiolates on Metals: A Review Article on Sulfur-Metal Chemistry and Surface Structures, RSC Adv. **4**, 27730 (2014). doi:10.1039/C4RA04659E

[6]   C. Vericat, M. E. Vela, G. Benitez, P. Carro, and R. C. Salvarezza, Self-assembled monolayers of Thiols and Dithiols on Gold: New Challenges for a Well-Known System, Chem. Soc. Rev. **39**, 1805 (2010). doi:10.1039/B907301A

[7]   J. C. Love, L. A. Estroff, J. K. Kriebel, R. G. Nuzzo, and G. M. Whitesides, Self-Assembled Monolayers of Thiolates on Metals as a Form of Nanotechnology, Chem. Rev. **105**, 1103 (2005). doi:10.1021/cr0300789

[8]   J. L. Wilbur and G. M. Whitesides, in *Nanotechnology*, edited by G. Timp (Springer-Verlag, New York, NY, 1999). doi:10.1007/978-1-4612-0531-9

[9]   A. Ulman, Formation and Structure of Self-Assembled Monolayers, Chem. Rev. **96**, 1533 (1996). doi:10.1021/cr9502357

[10]   J. Telegdi, Formation of Self-Assembled Anticorrosion Films on Different Metals, Materials **13**, (2020). doi:10.3390/ma13225089

[11]   G. A. Somorjai and Y. Li, *Introduction to surface chemistry and catalysis*, 2nd ed., (Wiley, Hoboken, NJ, 2010).

[12]   K. W. Kolasinski, *Surface science: Foundations of Catalysis and Nanoscience*, 4th ed., (Wiley, Hoboken, NJ, USA, 2020).

[13]   N. Papaiconomou, I. Billardde, and E. Chaine, Extraction of Iridium(IV) from Aqueous Solutions Using Hydrophilic/hydrophobic Ionic Liquids, RSC Adv. **4**, 48260 (2014). doi:10.1039/c4ra06991a

[14]   Y. Yan, Q. Wang, Z. Xiang, and Y. Yang, Separation of Pt(IV), Pd(II), Ru(III), and Rh(III) from Chloride Medium Using Liquid–liquid Extraction with Mixed

Imidazolium-based Ionic Liquids, Sep. Sci. Technol. **53**, 2064 (2018). doi:10.1080/01496395.2018.1440304

[15]   S. Yamamoto *et al.*, Direct Evidence of Interfacial Hydrogen Bonding in Proton-Electron Concerted 2D Organic Bilayer on Au Substrate, e-J. Surf. Sci. Nanotechnol. **17**, 49 (2019). doi:10.1380/ejssnt.2019.49

[16]   H. S. Kato, S. Yoshimoto, A. Ueda, S. Yamamoto, Y. Kanematsu, M. Tachikawa, H. Mori, J. Yoshinobu, and I. Matsuda, Strong Hydrogen Bonds at the Interface between Proton-Donating and -Accepting Self-Assembled Monolayers on Au(111), Langmuir **34**, 2189 (2018). doi:10.1021/acs.langmuir.7b03451

[17]   A. J. Zaitouna and R. Y. Lai, Design and Characterization of a Metal Ion–Imidazole Self-assembled Monolayer for Reversible Immobilization of Histidine-tagged peptides, Chem. Commun. **47**, 12391 (2011). doi:10.1039/C1CC15510E

[18]   J. Wei, H. Liu, A. R. Dick, H. Yamamoto, Y. He, and D. H. Waldeck, Direct Wiring of Cytochrome c's Heme Unit to an Electrode: Electrochemical Studies, J. Am. Chem. Soc. **124**, 9591 (2002). doi:10.1021/ja025518c

Vira ZAKUSILOVA

Monocouches auto-assemblées d'alcanes thiols sur détecteurs silicium recouverts d'or pour la sorption des métaux

Résumé

Cette thèse contribue aux développements pour les futures expériences visant l'élément 109, le meitnerium. Elle porte sur la préparation de silice fonctionnalisée et son application pour la séparation des éléments. Ces matériaux qu'imitent des détecteurs au silicium permettront de comparer la réactivité du meitnerium et de ses homologues, l'Ir et le Rh, vis-à-vis de ces surfaces lors d'expériences on-line. Pour la fonctionnalisation, nous avons employé la méthodologie basée sur la formation de monocouches auto-assemblée d'organothiols, le 1-(11-mercaptoundécyl)imidazole et l'acide 12-mercaptododécanoïque. Nous avons démontré que ces monocouches obtenus sont stables au moins pendant un mois et leur surface est saturée après l'absorption de l'Ir(IV) et Rh(III) à partir de solution aqueuse acide. La deuxième partie de la thèse porte sur l'étude de la sorption de l'Ir, l'erbium et l'astate sur les surfaces de matériaux préparés lors des expériences au cyclotron. Les résultats démontrent que la position du détecteur et son revêtement jouent un rôle important.

Mots-clés: Silice fonctionnalisée, Monocouches auto-assemblées d'organothiols, Sorption de l'iridium et le rhodium, Expériences on-line au cyclotron

Résumé en anglais

In this work, thiolate-functionalized gold-coated silicon detectors were proposed as new materials for the comparison of the sorption properties of superheavy elements and their lighter homologs produced during online cyclotron-based experiments. The first part of the dissertation discusses the functionalization of gold-coated silicon substrates with 1-(11-mercaptoundecyl)imidazole and 12-mercaptododecanoic acid self-assembled monolayers. The functionalized surfaces were characterized offline utilizing several surface science techniques. The successful results showed the studied materials are stable for at least one month and demonstrate the surface saturation with Ir(IV) and Rh(III) adsorbed from hydrochloric acid solutions. The second part of the dissertation discusses the new detector setup developed to study the sorption of online-produced Ir, Er, and At. The promising results demonstrated the role of the detector position and its coating on the element sorption.

Keywords: Functionalized silicon, Self-assembled monolayers of organothiols, Sorption of iridium and rhodium, Online cyclotron-based experiments

DEDICATION

To my big family in Ukraine and outside of it

ACKNOWLEDGEMENTS

I would like to thank a lot of people who helped me throughout my Ph.D. program. First of all, Dr. Maria Boltoeva who took me originally as a Master student and believed in me to obtain a Ph.D. degree. Thank you for offering a great opportunity to work in the well-known Heavy Elements group in one of the best universities in the United States. It was a hard decision to make, but now, I can say for sure that it was worth it. Thank you for always keeping in touch with me despite the time difference, loads of work, and family duties. Having three kids and a lot of work to do, you are the only person who would genuinely give me a helping hand without making me feel uncomfortable for asking.

Prof. Charles M. Folden III, thank you for agreeing to take me as a Research Assistant to work on my Ph.D. project in collaboration with Dr. Maria Boltoeva to achieve my goal of obtaining a higher degree. Thank you for allowing me to work on such an interesting project that taught me a lot of new things I did not know before and never thought possible. Thank you for sending me to conferences where I could present my work and discuss it with others in the field. This greatly helped me with my professional development and communication skills. Thank you for always proofreading the documents I needed to submit and giving your comments.

Dr. Evgeny E. Tereshatov, thank you for guiding me on how to perform the experiments I conducted during the past three years, helping me analyze my data whenever I needed it, teaching me new methods of data analysis in Origin, and putting a lot of your effort into the design of the sRTC. Thank you for showing me around the town in the country I had never been to and introducing me to the best restaurants in town. I'll never forget the first time I tried an American burger with you!

Kevin Glennon, thank you for showing me around our lab when I came to the group. You helped me perform several experiments, always proofread documents I asked you to check for me, and have always been a nice person to talk to.

Jenna Garcia, thank for you helping me with alpha spectroscopy measurements. I am impressed by how you can become engaged in someone else's work with great care. I am solemnly thankful for our friendship; you became a close friend to me.

Katie Childers, I will be forever thankful for teaching me how to analyze data from online experiments in ROOT that looked unreal to me at first. Thank you for answering my questions about the separator and for working together in the cave. I was able to describe the online experiments without hesitation in this dissertation. Jenna and I miss our lunches together.

Jordan Mildon, thank you for helping us to set up the separator, doing important magnet tests, and helping me with the data analysis in ROOT. It led us to perform the experiment results of which I am presenting in this dissertation. I would like to mention other members of our group who maintain a friendly environment at work: Isaac Haynes, Amelia Kirkland, and Sarah Loftin.

I am grateful to my friends from Ukraine who keep in touch even though I am so far away. Thank you to all my new friends I have made in College Station who give me great company. Thank you to my boyfriend, Dustin Scriven, you fill me with a tremendous amount of support.

Finally, I do not have enough words to describe how thankful I am to my family for always being supportive of me and especially to my mom Ludmila who supported the idea of studying in France which led me eventually to move to the United States where I feel safe right now. Thank you to my brother Sasha, my sister-in-law Margarita, my grandparents Fedia and Anastasia, aunt Sveta, and cousin Maxim for being there for me and cheering me up whenever I felt down. I would not be where I am right now without my family.

CONTRIBUTORS AND FUNDING SOURCES

At the beginning of the PhD program, several experiments were conducted to finish the Master's project and were published in December 2021. A paper based on the offline experiments of this dissertation is under review by coauthors. The results of the online experiments will be discussed in an additional paper that is currently being written.

NOMENCLATURE

AO	Atomic orbital
AFM	Atomic Force Microscopy
AGGIE	Al Ghiorso's Gas-filled Ion Equipment
B	Bin width
β_6	Cumulative stability constant
C	Number of counts of a nuclide
C11-Im	Gold-coated silicon functionalized with 1-(11-mercaptoundecyl)imidazole self-assembled monolayer
CN	Compound nucleus
COLD	Cryo-online detector
COMPACT	Cryo Online Multidetector for Physics And Chemistry of Transactinides
FLNR	Flerov Laboratory of Nuclear Reactions
GSI	Gesellschaft für Schwerionenforschung
$-\Delta H_{ads}$	Adsorption enthalpy
Image Rq	Surface roughness
Im-C$_{11}$-SH	1-(11-Mercaptoundecyl)imidazole
INAA	Instrumental Neutron Activation Analysis
IP	Ionization potential
JINR	Joint Institute for Nuclear Research
K	Surface coverage
LBNL	Lawrence Berkeley National Laboratory
λ	Rate constant parameter

Liquid-UVPO   Liquid-based hydrogen peroxide (H_2O_2)-mediated UV-photooxidation

treatment

MDDA   12-Mercaptododecanoic acid

P Peak area

R Normalized rate of a nuclide

RIKEN   Institute of Physical and Chemical Research

RS Rutherford scattering events

R_s Detector resolution

sRTC   Simple Recoil Transfer Chamber

SAM   Self-assembled monolayer

SS Surface saturation

SHE   Superheavy element

SHIP   Separator for Heavy Ion reaction Products

Si+Au   Gold-coated silicon

NP-SIMS   Nanoprojectile Secondary-Ion Mass Spectrometry

T_a Deposition temperature

TASCA   TransActinide Separator and Chemistry Apparatus

TEES   Texas Engineering Experiment Station

TRIGA   Training, Research, Isotopes, General Atomics

UNILAC   Universal Linear Accelerator

XPS   X-ray Photoelectron Spectroscopy

x_c,   Centroid of a nuclide peak

$T_{1/2}$ Half-life of a nuclide

I	α-branching ratio
σ	Cross-section of a nuclear reaction
y_o	Offset
A	Amplitude
ω_1	Full width at half maximum
ω_2	Variance of the low-energy side
ω_3	Variance of the high-energy side

TABLE OF CONTENTS

LIST OF FIGURES

LIST OF TABLES

CHAPTER I

INTRODUCTION

1.1   Superheavy Elements (SHEs)

The latest release of the Periodic Table of chemical elements shown in Figure 1 contains 118 elements [5]. SHEs are the elements with the atomic number $Z \geq 104$, they give an end to the actinide series and begin the series of transactinide elements [6]. The named elements exist due to shell stabilization of their nuclei which enables to keep the balance between the attractive nuclear force and the repulsive Coulomb force [6].
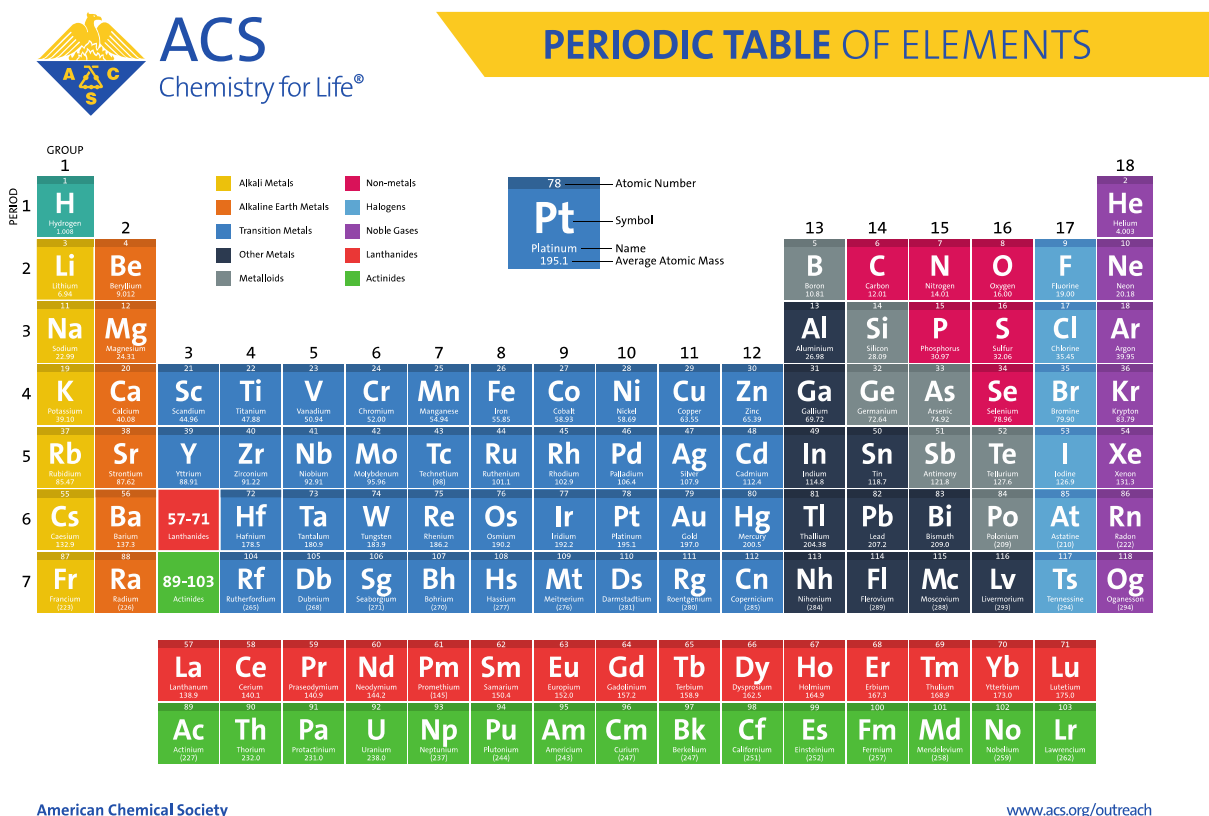
Figure 1. The Periodic Table of Elements. Reprinted from ref. [5]

SHEs are produced artificially through heavy-ion reactions during which two heavy nuclei fuse to form a compound nucleus (CN) [6]. Afterward, neutron evaporation leads to its de-excitation, and the formed nuclide alpha decays [6]. The excited heavy nucleus is very fissile due to a strong competition between spontaneous fission and alpha decay [6]. The survival probability of the CN is only 10^{-2} - 10^{-3} per evaporation step [6]. Short half-lives (from seconds to microseconds) and small cross-sections (from nanobarns to femtobarns) of produced isotopes limit the chemical characterization of SHEs to 'single atoms' making so-called "one-atom-at-a-time" experiments especially challenging to perform [6, 7].

There are two types of heavy-ion reaction mechanisms that are used to synthesize SHEs, namely "cold" and "hot" fusion. The schematics of the two reaction mechanisms are depicted in Figure 2. During cold fusion reactions, ^{208}Pb or ^{209}Bi targets are bombarded with appropriate heavy-ion projectiles of ^{54}Cr, ^{58}Fe, ^{62,64}Ni, or ^{68,70}Zn [6-8]. Typically, one or two neutrons are evaporated from the CN with the low excitation energy in the order of 10-15 MeV [7, 8]. Formed nuclides alpha decay until spontaneous fission in the region of the known elements.

Elements 107 to 112 were synthesized through cold fusion reactions at Gesellschaft für Schwerionenforschung (GSI) in Darmstadt, Germany [6, 7]. The last SHE that was synthesized using the cold fusion reaction was nihonium (Nh, Z=113) [9]. A ^{70}Zn ion beam bombarded a ^{209}Bi target producing ^{278}Nh isotope at the Institute of Physical and Chemical Research (RIKEN) in Wako City, Japan in 2004 [9]. Beam irradiations continued until 2012 which allowed for the production of a few atoms of nihonium [10]. The discovery of nihonium was recognized by the International Union of Pure and Applied Chemistry (IUPAC) in 2013 [11]. The cross-section of the ^{209}Bi(^{70}Zn, n)^{278}Nh reaction is only ~20 fb; such a small value indicated the inability to utilize the cold-fusion mechanism to synthesize elements with Z>113 [12].
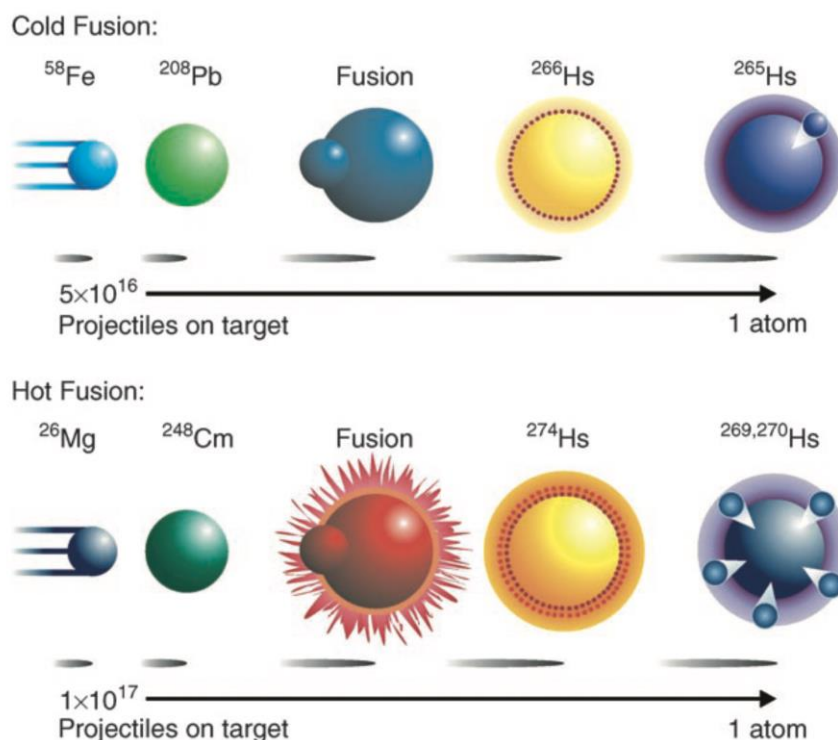
Figure 2. Schematics of cold- and hot-fusion reaction mechanisms with examples of the ^{208}Pb(^{58}Fe, n)^{265}Hs and the ^{248}Cm(^{26}Mg,4–5n)$^{269-270}$Hs reactions, respectively. Figure used with permission from ref. [8].

During hot fusion reactions, an actinide target (^{238}U, ^{242,244}Pu, ^{243}Am, ^{248}Cm, ^{249}Bk, ^{249}Cf, or ^{254}Es) is bombarded with highly accelerated light-ion projectiles of ^{48}Ca, ^{26}Mg, ^{18}O, or ^{22}Ne [6-8]. Usually, three or five neutrons are evaporated from the CN with the excitation energy of 40-50 MeV [6, 8]. The cross sections for the production of SHEs can be up to 100 times larger than those measured during cold fusion reactions [7]. Often, decay chains end in unknown regions which makes it challenging to identify nuclides.

Elements 114 to 118, flerovium to oganesson, with more neutron-rich nuclides, as well as multiple isotopes of elements 112, copernicium, and 113, nihonium, were produced through hot fusion reactions at Flerov Laboratory of Nuclear Reactions (FLNR), Joint Institute for Nuclear Research (JINR) in Dubna, Russia [6, 7]. Element 118, oganesson, was first synthesized in 2002

during the experiment using a [48]Ca ion beam on a [249]Cf target to produce [294]Og, only one event of this isotope was detected [7, 13]. The second experiment with the higher sensitivity resulted in the detection of two additional events of the isotope [294]Og [13]. The discovery of oganesson announced in 2005 [13] and its official recognition by IUPAC in 2016 [11] completed the seventh period of the periodic table [7].

Proper chemical studies must be performed to confirm whether a SHE belongs to a particular group it was placed in the Periodic Table [14]. The chemical properties of SHEs are strongly influenced by relativistic effects that increase with Z^2 and cause deviations in the periodicity of the chemical properties [8, 14-17]. The electrons of SHEs orbiting the highly charged nucleus closer to it are accelerated to relativistic velocities due to the stronger Coulomb forces that the electrons experience [7]. Consequently, the electron mass increases according to:

$$m = m_o[1 - (v/c)^2]^{-1/2}, \qquad \text{Eq. 1}$$

where m_o is the rest mass of the electron, v is the velocity of the electron, and c is the speed of light [14, 17].

The relativistic mass increase of the electron results in the contraction and stabilization of spherically symmetric s and $p_{1/2}$ atomic orbitals (AOs) [14, 17]. This is known as a direct relativistic effect that originates from the inner K- and L-shell regions [14, 17]. The expansion and destabilization of the $p_{3/2}$, d, f, g, etc. AOs, caused by the increased screening of the nucleus by the relativistically contracted s and $p_{1/2}$ AOs, is known as the indirect (the second) relativistic effect [14, 17]. The spin-orbit splitting of the AOs with the orbital quantum number $l>1$ is called the third relativistic effect [14, 17]. For instance, the splitting of the three isoenergetic p levels and the electron distribution into the more stabilized $p_{1/2}$ and the less stabilized $p_{3/2}$ subshells [7]. The splitting of the isoenergetic d levels is induced as well [7].

Overall, relativistic effects cause big changes in the orbital geometry as well as stronger electron binding in atoms [7]. Their impact on the valence orbitals of the heavier elements is bigger compared to that for lighter homologs [14]. This might result in different chemical properties of SHEs and their lighter congeners [14]. Therefore, rapid chemical techniques must be developed to characterize the chemical properties of SHEs and verify their position in the Periodic Table.

1.1.1   Meitnerium

Meitnerium (Mt, Z=109) is a SHE located in group 9 of the Periodic Table [8]. Mt was synthesized for the first time during an experiment at GSI in 1982 [18-20]. It was produced using the reaction ^{209}Bi(^{58}Fe, n)^{266}Mt performed at the new at that time Separator for Heavy Ion reaction Products (SHIP) [18]. The latest SHIP setup can be found in Figure 3. The observed one-event decay chain that consisted of two uninterrupted alpha disintegrations followed by fission was assigned to the isotope ^{266}Mt [18]. The cross-section of the reaction was estimated to be about 10^{-35} cm^2, and the excitation energy of the compound nucleus was estimated to be in the range of 20-26 MeV [18]. A more detailed description of the results was published in 1984 [21] that were finally confirmed in 1988 [22]. The combined result of the two experiments reported the half-life of $(3.4^{+6.1}_{-1.3})$ ms for ^{266}Mt and the cross-section of (10^{+10}_{-6}) pb for the reaction provided above [22].

Ship 1994
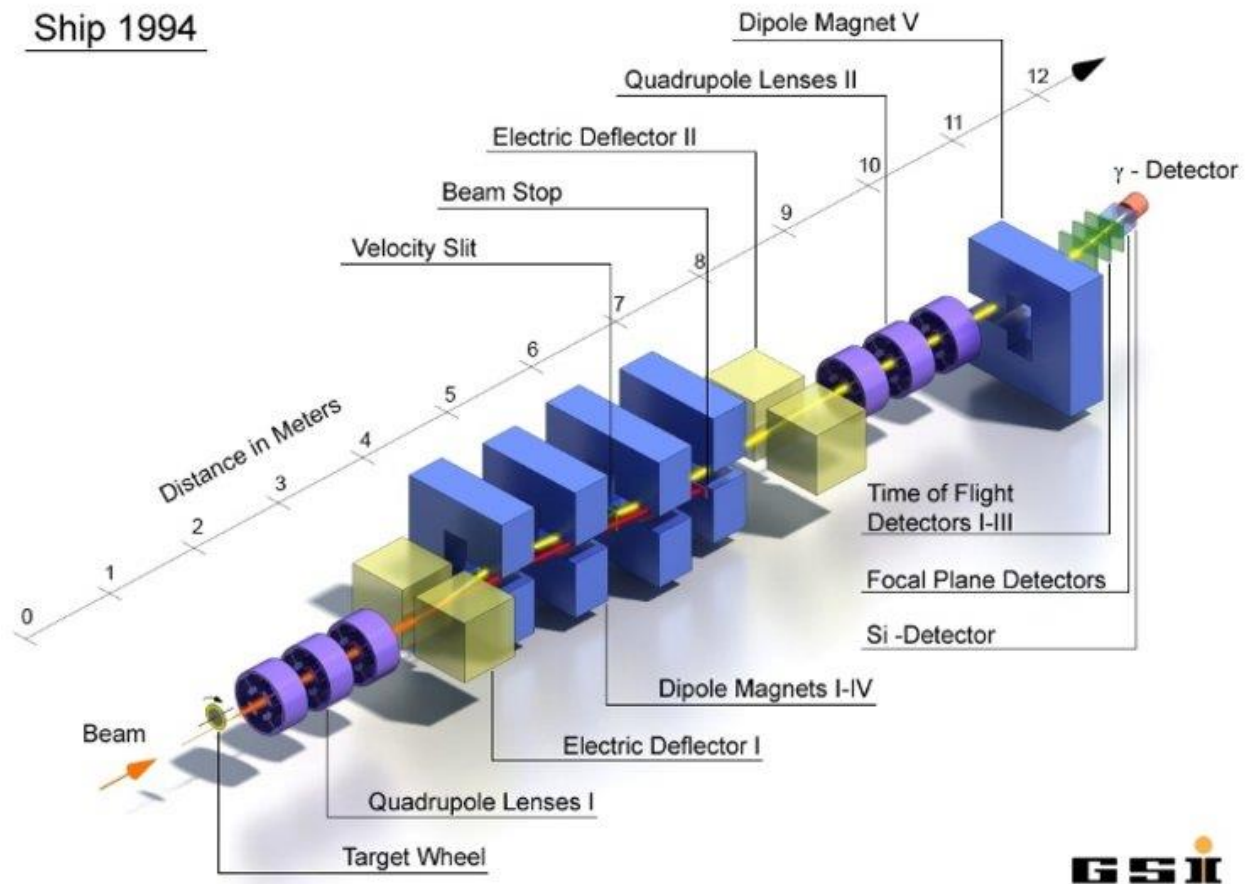
Figure 3. The schematic diagram of the velocity filter SHIP setup in its 1994 modified version. Reprinted from ref. [23].

12 decay chains of ^{266}Mt were measured using three different beam energies in an experiment conducted in 1997 [24]. The mean half-life of ^{266}Mt of $(1.7^{+0.6}_{-0.4})$ ms and the production cross-section of (7.5 ± 2.7) pb were obtained [24]. The wide range of α energies from 10.5 to 11.7 MeV indicated the existence of complicated level and decay schemes for ^{266}Mt [24].

A different nuclear reaction ^{208}Pb(^{59}Co, n)^{266}Mt was studied using the Berkeley Gas-filled Separator at the Lawrence Berkeley National Laboratory (LBNL) 88-Inch Cyclotron in 2009 [25]. The half-life of ^{266}Mt of $(3.3^{+2.5}_{-1.0})$ ms and the cross-section of $(7.7^{+5.5}_{-3.3})$ pb were measured [25] and reported to be consistent with the latest values reported by Hofmann *et al.* [24]. The CN excitation

energy was 14.9 MeV [25]. The decay properties of daughter nuclides were also consistent with the results published in the literature [25].

The more neutron-rich isotope ^{268}Mt was detected in the α-decay chain of ^{272}Rg [26, 27]. The half-life of ^{268}Mt was measured to be (70^{+100}_{-30}) ms in an earlier work [26] and (42^{+29}_{-12}) ms in a later work conducted by Hofmann *et al.* [27]. The mean α energy for ^{268}Mt was 10.258 MeV taken as an average of α energies from three decay chains of ^{272}Rg [27].

The isotope ^{270}Mt with the mean half-life of $(0.69^{+0.95}_{-0.26})$ s was found in the decay chain of ^{278}Nh produced in the ^{209}Bi(^{70}Zn, n)^{278}Nh reaction [10]. The α-decay energies were 10.03 ± 0.07 and 10.26 ± 0.07 MeV [10]. All Mt isotopes that were discovered and identified during the cold- and hot-fusion reactions are listed in Table 1.

Table 1. Mt isotopes produced through cold- and hot-fusion reactions in accelerator facilities.

Isotopes	Half-life	Nuclear reaction	Facility	Reference
^{266}Mt	$(1.7^{+0.6}_{-0.4})$ ms	^{209}Bi(^{58}Fe, n)^{266}Mt	GSI	[24]
^{266}Mt	$(3.3^{+2.5}_{-1.0})$ ms	^{208}Pb(^{59}Co, n)^{266}Mt	LBNL	[25]
^{268}Mt	(42^{+29}_{-12}) ms	^{209}Bi(^{64}Ni, n)^{272}Rg	GSI	[27]
^{270}Mt	$(0.69^{+0.95}_{-0.26})$ s	^{209}Bi(^{70}Zn, n)^{278}Nh	RIKEN	[10]
^{278}Mt	$(7.7^{+37}_{-3.5})$ s	^{249}Bk(^{48}Ca,3n)^{294}Ts		[28]
^{276}Mt	$(0.68^{+0.20}_{-0.12})$ s	^{243}Am(^{48}Ca,3n)^{288}Mc	FLNR	[29]
^{275}Mt	$(9.7^{+46}_{-4.4})$ ms	^{243}Am(^{48}Ca,4n)^{287}Mc		[30]
^{274}Mt	(440^{+810}_{-170}) ms	^{237}Np(^{48}Ca,3n)^{282}Nh		[31]

The chemical properties of Mt have not been characterized yet due to low cross-sections and short half-lives of Mt isotopes (less than one second) produced during cold-fusion reactions

making chemical investigations hard to perform [8]. Thus far, only theoretical predictions were performed.

Mt is predicted to have $6d^77s^2$ ground state, its properties are expected to be similar to those of its lighter homologs, iridium (Ir, Z=77) and rhodium (Rh, Z=45) [17]. However, strong relativistic effects are predicted to have a bigger impact on the chemical properties of Mt located in the seventh period of the Periodic Table rather than those of its lighter homologs in the sixth and fifth periods [17].

The ionization potential (IP) of 8.7 eV for Mt was calculated using the Dirac–Fock (DF) theory [32]. It is lower than the IP value of 8.967 eV reported for Ir, whereas ideally, it should be larger [17]. It is necessary to perform more accurate calculations for Mt in the near future [17].

The most stable oxidation states for Mt are expected to be +1 (in the aqueous solution), +3, and +6 [32]. The prediction of the stable +6 oxidation state means that volatile hexafluorides of Mt might be formed, making chemical separation experiments feasible to perform [32]. Overall, the chemistry of Mt is predicted to show a strong tendency toward the formation of complex ions of this element [32].

The bond length in MtH_3, MtC^-, MtN were calculated using the density functional method with the Amsterdam Density Functional (ADF) program package [33, 34]. The single-bond and the triple-bond radii of the 6d element, Mt, are about 8-9 pm larger than for its 5d analog, Ir, as can be seen in Table 2. It means that relativistic effects do not change the general periodic trend in group 9, and Mt still forms another normal d trend: 4d≤5d<6d.

Table 2. The single-bond and the triple-bond radii of 4d (Rh), 5d (Ir), and 6d (Mt) elements.

Bond	Species Class	Species	Distance, pm	Reference
Single	Hydrides	RhH_3	161.7	[33]
			152	[35]
		IrH_3	154.3	[33]
		MtH_3	162.999	
Triple	Carbides	RhC^-	161.52	[34]
		IrC^-	165.08	
		MtC^-	173.22	
	Nitrides	RhN	159.80	
		IrN	159.06	
		MtN	166.59	

Nonetheless, longer-lived isotopes of Mt might be produced during hot-fusion reactions involving [48]Ca beams on actinide targets which will make chemical characterization possible [8]. Unfortunately, Mt has been produced only indirectly in hot-fusion reactions [19].

For example, [278]Mt with a half-life of $(7.7^{+37}_{-3.5})$ s is a decay product observed in the decay chain of [294]Ts produced in [249]Bk([48]Ca,3n)[294]Ts reaction [28].

[276]Mt and [275]Mt with the half-lives of $(0.68^{+0.20}_{-0.12})$ s and $(9.7^{+46}_{-4.4})$ ms, respectively, were found to be members of the decay chains of the Mc isotopes produced during the [243]Am([48]Ca,3n)[288]Mc and the [243]Am([48]Ca,4n)[287]Mc reactions, respectively [29, 30].

The decay chain of [282]Nh produced during the [237]Np([48]Ca,3n)[282]Nh reaction contains the [274]Mt isotope with a half-life of (440^{+810}_{-170}) ms [31].

Volatile oxides, hydroxides, or carbonyls of Mt might be proper species for the chemical separation and characterization of this element using gas-phase chromatography techniques [8, 36].

1.1.2 SHE Chemical Experiments

In the field of studying the chemical properties of SHE, the gas-solid chromatography method is the most effective way to perform one-atom-at-a-time experiments [4, 8, 14, 17, 37]. Chemistry studies and the detection of single atoms of SHE occur in a chromatography column by registering their nuclear decay using silicon detectors or gold-coated silicon detectors [4].

Thermochromatography is a method in which a negative temperature gradient is applied to a chromatography column [8, 37]. Volatile species are transported through the column by a carrier gas [37]. The time the species are adsorbed on the surface of the column increases exponentially due to the applied negative temperature gradient [37]. Species with different volatility form distinct deposition peaks depending on their adsorption enthalpy $(-\Delta H_{ads})$ on the surface of the column [37]. As a result, this allows the separation of different species [37]. $-\Delta H_{ads}$ values can be calculated by knowing the event distribution in the column and using Monte Carlo simulations based on the adsorption model [14]. The deposition temperature (T_a) is the characteristic quantity that is associated with the deposition zones registered by a series of planar silicon detectors comprising a column [14, 37].

Typically, two detector arrays face each other in close proximity, therefore, the probability to observe a series of α-decays of a produced isotope is high [37]. The sensitivity of thermochromatography experiments for transactinides decaying by spontaneous fission is high due to the fact that all the species get adsorbed eventually on the column surface, and each nuclide's

decay is registered [37]. Consequently, the position of each decay in the column can explain the chemistry of species under study [37]. A temperature profile and an integral chromatogram resulting from thermochromatography are pictured in Figure 4.
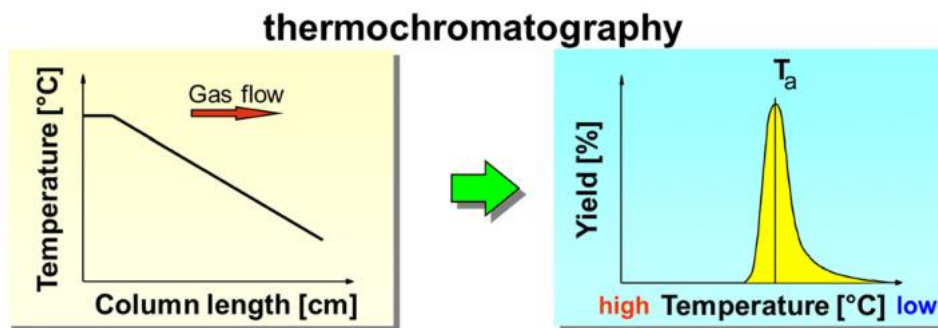
Figure 4. Temperature profile (left image) and integral chromatogram (right image) obtained during thermochromatography. Illustration used with permission from ref. [37].

During the chemical characterization of copernicium (Cn, Z=112), silicon detectors coated with a layer of gold were used for the first time [1]. The ^{242}Pu(^{48}Ca, 3n)^{287}Fl reaction was performed at the U-400 cyclotron at the FLNR [1]. The thermochromatographic in situ volatilization combined with the cryo-online detector (COLD) was employed [1]. The experimental setup is shown in Figure 5.
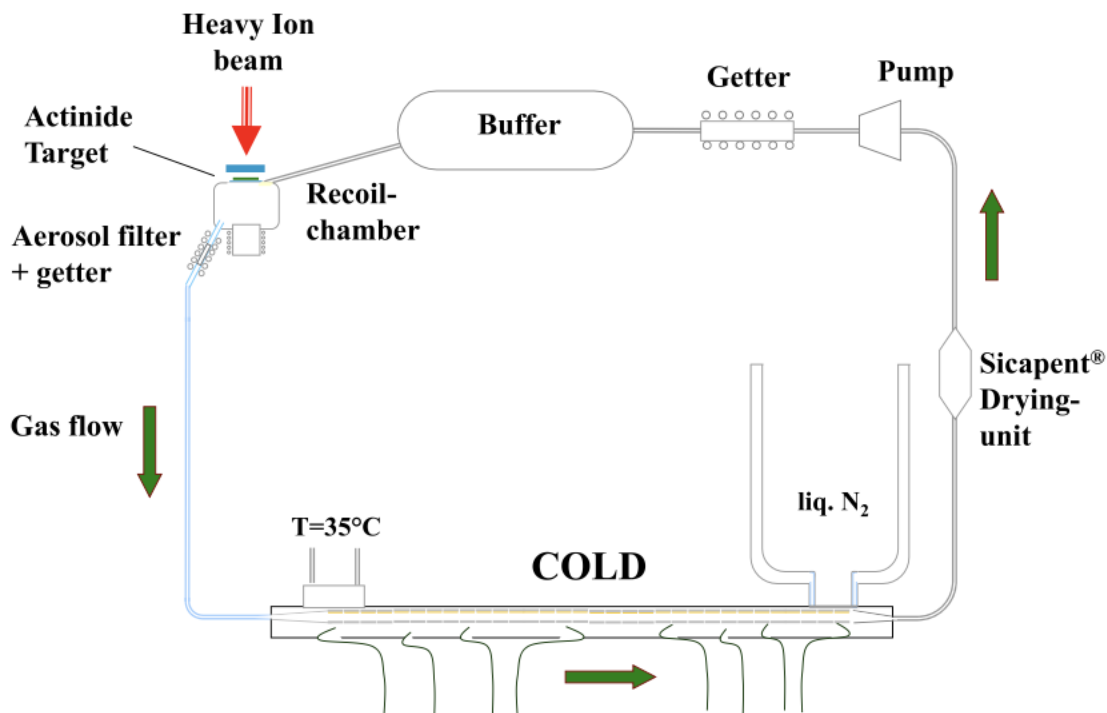
Figure 5. The experimental setup used in thermochromatography experiments performed for Cn chemistry studies at FLNR. Illustration used with permission from ref. [37].

The detector array consisted of 32 pairs of ion-implanted planar silicon detectors that face each other and form a chromatographic channel [1]. The detector surface on one side of the channel was coated with 30-50 nm of gold [1]. Two negative temperature gradients of +24 to -184°C and +35 to -180°C were applied in this experiment [1].

The adsorption of two atoms of ^{283}Cn, produced after the α-decay of the short-lived ^{287}Fl, was observed on the gold-covered side of the detector [1]. Cn was found to be a very volatile element that showed a metallic interaction with the gold surface, confirming the belonging of Cn to group 12 of the Periodic Table [1].

A year later, the overall efficiency of the experiment was approximately 3 times higher, and three additional decay chains of ^{283}Cn were obtained [2]. The temperature gradient was held between +32 and -164°C [2]. Cn was confirmed to be more volatile than its lighter homologs. The

adsorption enthalpy of Cn on the gold surface was determined to be $-\Delta H_{ads}^{Au}(\text{Cn}) = 52_{-3}^{+4}$ kJ/mol which was lower than that for its lighter homologs [2]. The calculated $-\Delta H_{ads}^{Au}$ value was higher than the theoretically predicted adsorption enthalpy using a physisorption model [2].

The obtained results confirmed the formation of a metallic bond during the interaction between Cn and Au which was weaker than that for its lighter homologs [2]. This demonstrated that the trend of increasing stabilization of the elemental atomic state due to relativistic effects is saved in group 12 of the Periodic Table.

The results of the first Nh chemistry experiments performed at FLNR without pre-separation showed that Nh strongly reacts with gold: $-\Delta H_{ads}^{Au} > 60$ kJ/mol [3]. It was concluded that the observed species was either atomic Nh or its hydroxide NhOH [3]. However, improvements in the used technique needed to be made, such as using an electromagnetic recoil separator [4]. This would increase the probability of detection of Nh and its daughters while the background in α-decay spectra caused by volatile byproducts of a multi-nucleon transfer reaction would be decreased [4].

After the successful chemical characterization of flerovium (Fl, Z=114), at the gas-filled separator TransActinide Separator and Chemistry Apparatus (TASCA) at GSI using gold-coated silicon detectors [38], experiments aimed at the study of Nh chemistry using a similar setup were initiated [4]. Therefore, a pulsed ^{48}Ca^{10+} beam bombarded a ^{243}Am target wheel to produce ^{288}Mc using the Universal Linear Accelerator (UNILAC) [4]. The ions of interest were thermalized in a He/Ar gas mixture inside the Recoil Transfer Chamber (RTC) and flushed out to the Cryo Online Multidetector for Physics And Chemistry of Transactinides (COMPACT) [4]. The schematic of the experimental setup is displayed in Figure 6.
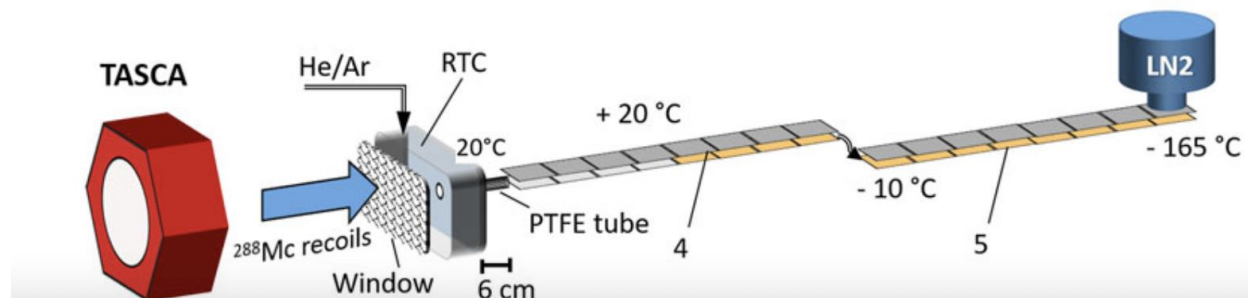
Figure 6. The experimental setup used in thermochromatography experiments performed for Nh chemistry studies at GSI. Reprinted from ref. [4].

The first COMPACT array consisted of 16 pairs of silicon detectors followed by 16 pairs of gold-coated silicon detectors and was kept at room temperature [4]. The second COMPACT array consisted of 32 pairs of gold-coated silicon detectors, and a negative temperature gradient was applied to it [4].

Unfortunately, no decay chains of ^{288}Mc or its α-decay product, ^{284}Nh, were observed [4]. Only one spontaneous fission event was observed which could not be assigned to the decay of the named isotopes [4]. This suggested that Nh has higher reactivity than Cn and Fl given the fact that Nh has one unpaired electron in the outermost electron shell: $7s^2 7p_{1/2}^{1}$ [4].

Possibly, Nh was irreversibly adsorbed on the inner wall of the PTFE tube which connected the RTC to the first COMPACT which led to a loss of Nh atoms [4]. The non-observation of Nh might also be explained by the formation of NhOH which is predicted to be non-volatile [4]. As a result, an improved detector array called miniCOMPACT was developed [4]. Such a setup does not require any transportation tubes between the RTC and the detection system [4]. The transport efficiency from the RTC into the miniCOMPACT was approximately 30% for the highly reactive francium isotopes, $^{202-205}$Fr [4]. This implies that studies of Nh and Mc chemistry are now possible [4].

1.2 Iridium and Rhodium Chemistry

Ir (Z=77) and Rh (Z=45) are expected to be homologs of Mt. Ir has two stable naturally occurring isotopes: [191]Ir and [193]Ir with abundancies of 37.3% and 62.7%, respectively. Rh has one naturally occurring isotope: [103]Rh. In the earth's crust, the concentration is 0.3‑5 ng/g for Ir and less than 0.5 ng/g for Rh.

In a U.S. Geological Survey report, Ir and Rh are reported as critical minerals which means their supply is at risk [39]. The common minerals that contain Ir are alloys of osmium and iridium called osmiridium (syserkskite), iridosmium (nevyanskite), or ruthenosmiridium. Hollingworthite and irsarite contain both Ir and Rh. They are predominantly produced as by-products during the mining and refining of host commodities such as platinum and nickel [40].

To separate Ir and Rh from other platinum-group metals present in a commodity, they first need to be dissolved [41]. After the dissolution step in hydrochloric acid (HCl) that can be used for this purpose with an oxidizing agent, the formed species can be separated and extracted employing liquid-liquid extraction [41]. The recovery of Ir and Rh metals is achieved as a result [41]. This is one of the reasons why significant attention is paid to the chemistry of Ir and Rh in HCl solutions.

The electron ground states of Ir and Rh are $[Xe]4f^{14}5d^76s^2$ and $[Kr]4d^85s^1$, respectively. The most stable oxidation states of Ir are +3 and +4 [41]. The most stable oxidation states of Rh are +1 and +3 [41]. The oxidation states of Ir and Rh and corresponding examples of their compounds with different coordination numbers are listed in Table 3. Ir and Rh can form octahedral complexes with halide anions or ligands containing oxygen [41].

Table 3. Oxidation states of Ir and Rh and examples of their compounds [41]. Table adapted with permission from ref. [41]

Metal	Oxidation state	Coordination number			
		3	4	5	6
Ir	-2	$Ir(NO)_2PPh_3$			
Ir Rh	-1		$K[Ir(PF_3)_4]$ $[Rh(CO)_4]^-$	$[Rh(NO)_2Cl]_n$	
	0		$Ir_4(CO)_{12}$		$Rh_4(CO)_{12}$
	+1		$Ir(CO)Cl(PPh_3)_2$ $[Rh(CO)_2Cl]_2$	$HIr(CO)(PPh_3)_3$ $HRh(PF_3)_4$	
	+2		$Ir(CO)_2Cl_2$ $[Rh(C_4N_2S_2)_2]^{2-}$	$[Ir(CO)_2I_3]^-$ $[Rh(OAc)_2]_2$	
	+3			$H_3Ir(AsPh_3)_2$	$[IrCl_6]^{3-}$ $[Rh(H_2O)_6]^{3+}$
	+4				$[IrCl_6]^{2-}$ $Cs_2[RhCl_6]$
	+5				$[IrF_6]^-$ $[RhF_5]_4$
	+6				IrF_6, RhF_6

Ir and Rh have similar chemical behavior and exist in the form of different chloro-complexes in HCl solutions depending on their pH [41]. If the solution pH is below 2, Ir(IV) predominantly exists in the form of $IrCl_5^-$ and $IrCl_6^{2-}$ complexes [41-43]. $IrCl_6^{2-}$ is reduced to $IrCl_6^{3-}$ in even more acidic HCl solutions [42, 44]. In the pH range from 2 to 7, $IrCl_4(OH)_2^{2-}$ and $IrCl_2(OH)_4^{2-}$ complexes are formed [41]. In the pH range from 7 to 12, $IrCl_2(OH)_4^{2-}$ and neutral $IrO_2 \cdot 2H_2O$ are predominant species [41]. In an alkaline solution, the dark red-brown $IrCl_6^{2-}$ undergoes spontaneous reduction which leads to the formation of pale yellow-green $IrCl_6^{3-}$. The

speciation of Ir in HCl solutions is summarized in Table 4. Organic compounds containing phosphorus, arsenic and sulfur donors can reduce Ir(IV) to Ir(III) [41].

Table 4. The speciation of Ir(IV) in HCl solutions with different pH.

pH	<2	2-7	7-12	alkaline solution
Species	$IrCl_6^{2-}$	$IrCl_4(OH)_2^{\,2-}$ $IrCl_2(OH)_4^{2-}$	$IrCl_2(OH)_4^{2-}$ $IrO_2 \cdot 2H_2O$	$IrCl_6^{3-}$

In an aqueous solution, Rh(III) exists in the form of a stable yellow hexaaqua ion $Rh(H_2O)_6^{3+}$ [41]. When the pH of a solution is less than 1, hydroxy species $Rh(H_2O)_5(OH)^{2+}$ are formed [41]. When $Rh(H_2O)_6^{3+}$ is heated in excess of HCl, rose-pink $RhCl_6^{3-}$ is formed [41]. The major species of Rh(III) in HCl solutions are the following: $RhCl(H_2O)_5^{2+}$, $RhCl_2(H_2O)_4^{+}$, $RhCl_3(H_2O)_3$, $RhCl_4(H_2O)_2^{-}$, $RhCl_5(H_2O)^{2-}$ and $RhCl_6^{3-}$ [41, 45, 46]. When $Rh(H_2O)_6^{3+}$ is heated in diluted HCl, cationic species of $RhCl(H_2O)_5^{2+}$ and $RhCl_2(H_2O)_4^{+}$ are formed [41]. $RhCl_6^{3+}$ becomes predominant with an increase in the HCl concentration [41]. The speciation of Rh(III) in HCl solutions [47] is summarized in Figure 7.

Rh(III) speciation in HCl solution has been extensively studied, and all six stability constants of Rh(III) chloro-complexes are known [47]. However, only one cumulative stability constant of the Ir(IV) chloro-complex, $IrCl_6^{2-}$, was estimated so far ($\beta_6=10^{31}$) [48].
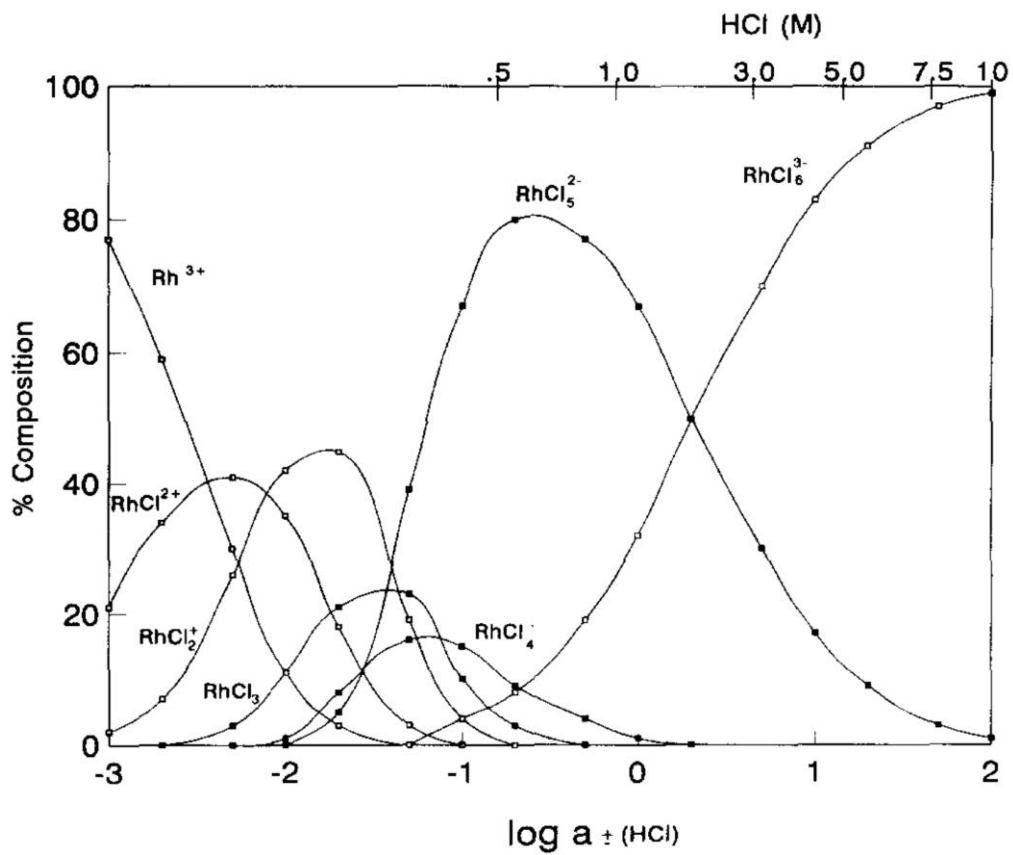
Figure 7. The speciation diagram for Rh(III) in HCl solutions with different concentration. Figure used with permission from ref. [49].

1.3   Self-Assembled Monolayers (SAMs)

A well-known approach to the functionalization of metals, metal oxides, and semiconductors is the formation of self-assembled monolayers (SAMs) on top of them [50-55]. SAMs are arrangements of molecules that can be spontaneously adsorbed on solid surfaces from a solution or a vapor phase [51].

SAMs molecules can be divided into three parts: a headgroup, a hydrocarbon chain, and a functional terminal group [51]. Different headgroups can bind to specific metals, metal oxides, and semiconductors [52-55]. The literature review on different types of SAMs adsorbed on different substrates is summarized in Table 5.

Alkanethiolate SAMs on the surfaces of noble and coinage metals (gold, silver, copper, palladium, platinum, nickel) are the most broadly studied and popular class of SAMs [50-55].

Among all listed metals, the preference is made for gold (Au), in particular, Au(111). Due to the fact that face-centered cubic metals with (111) orientation have the lowest surface free energy, such surfaces are more stable unlike metal surfaces with (100) orientation which undergo massive reconstructions [56, 57]. Gold is the most widely used metal during SAMs adsorption because it is easy to obtain in a form of thin films, reasonably inert, and forms SAMs of good quality [50, 52].

Thiols can form strong thiolate−Au covalent bonds of 50 kcal/mol during the SAMs formation [51], and these SAMs can be easily prepared in the liquid phase by the immersion of a substrate into an ethanolic thiol solution for up to 24 h [51, 52].

19

Table 5. Different types of SAMs adsorbed on different substrates.

Substrate	Type of SAMs	Reference
Gold	Alkanethiolate	[58-62]
	Selenolate	[63-65]
	Organogermane	[66]
	Dodecyl sulfate	[67]
Silver	Alkanethiolate	[68]
	Selenolate	[65, 69]
Copper	Alkanethiolate	[70]
	Amino acid	[71]
	Tetrazole	[72]
Palladium	Alkanethiolate	[73]
Platinum		[74]
Nickel		[75]
Titanium	Organophosphonic acid, organophosphate, and organosilane	[76]
Iron	Alkylamine	[77]
Titanium oxide and silicon oxide	Chlorosilane, alkoxysilane, carboxylic acid, and isocyanate	[78]
Various alloy and metal oxides	Hydroxamic, organophosphonic, carboxylic, and sulfonic acids	[79]
Sapphire	Carboxylic acid	[80]
Calcium fluoride	Dodecyl sulfate	[67]

The adsorption of thiols on the gold surface occurs in two steps, beginning with physisorption followed by chemisorption as illustrated in Eq. 2 and Eq. 3, respectively [51]. During the latter one, a thiol molecule, namely R-SH becomes deprotonated, turning into a thiolate (RS−Au) [51].

The adsorption process can be described as follows:

$$R\text{-}SH + Au \rightarrow (R\text{-}SH)_{phys}Au \qquad\qquad\qquad \text{Eq. 2}$$

$$(R\text{-}SH)_{phys}Au \rightarrow RS-Au + 1/2H_2 , \qquad\qquad\qquad \text{Eq. 3}$$
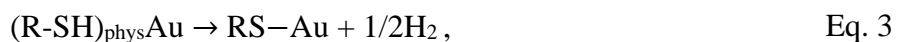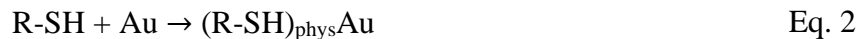
where R is an organic radical; in the case of alkanethiolates, $R=CH_3(CH_2)_n$, where n is the number of carbon atoms present in a molecule [51].

The scheme of the self-assembly of alkanethiolates is depicted in Figure 8 [51]. It is important to perform the SAMs deposition for up to 24 h due to several steps taking place during the self-assembly. As it was said, the physisorption occurs first, then, at the beginning of the chemisorption, molecules are mostly laying down. In time, they turn into the standing-up phase finishing with the formation of desired well-ordered molecules in a close-packed configuration [51].
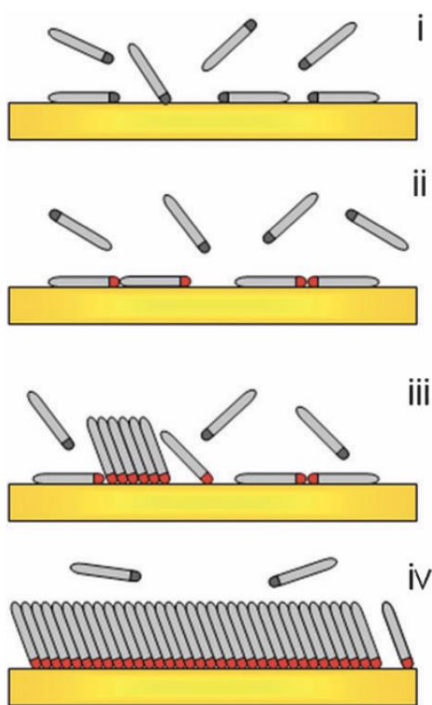
Figure 8. A scheme of the alkanethiolate SAMs formation on Au(111): physisorption (i), laying down phase formation (ii), nucleation of the standing up phase (iii), completion of the standing-up phase (iv). Illustration used with permission from ref. [51].

The high affinity of thiols to Au enables scientists to create well-defined organic substrates with useful chemical functionalities and properties which can be changed in advance based on the application [52].

1.4   Review of Past Studies

Kato *et al.* [81] reported the modification of gold disks or gold thin films deposited on cleaved mica with 1-(11-mercaptoundecyl)imidazole (Im-C_{11}-SH) SAMs for the design of a new conceptual electronic device. In a few works, mixed SAMs containing Im-C_{11}-SH deposited on gold electrodes were characterized for the future development of biosensors or biocatalytic devices [82, 83]. Gold-coated chips were modified with 12-mercaptododecanoic acid (MDDA) in the work of Chen *et al.* to develop a new label-free impedance biosensor based on a novel conductive linker [84]. MDDA SAMs on gold substrates have recently been used to prepare DNA-modified liquid-crystal droplets which can be potentially applied in surface information visualization and detection kits [85].

The literature review showed that thiolate SAMs on Au(111) have been utilized to study the interaction between various metals and terminal functional groups of SAMs [62, 83, 86, 87]. Magallanes *et al.* characterized the interaction between copper(II) ions and carboxylic acid- or alcohol-terminated thiolate SAMs on Au(111) for the future preparation of heavy metal ion sensors [86]. In their work, 3-mercaptopropionic and 16-mercaptohexadecanoic acids were investigated [86]. A new capacitor sensor was developed for the chromium(VI) determination by Kochana *et. al* [88], in their work, an Au(111) electrode was functionalized with ethanethiolate SAMs with the functional group exhibiting affinity for chromium(VI) anions. Ivanova *et al.* [87] reported the electrochemical deposition of monoatomic high layers of palladium and platinum on 4-

mercaptopyridine SAMs on Au(111) electrodes. In the work of Zaitouna and Lai [83], gold disk electrodes were modified with mixed SAMs containing Im-C_{11}-SH. They were used to coordinate divalent metals such as zinc(II), cobalt(II), and nickel(II) through the surface-immobilized imidazole terminal groups for the subsequent reversible immobilization of histidine-tagged peptides [83].

However, there were no works reported on the application of the Au(111) surfaces functionalized with Im-C_{11}-SH SAMs or MDDA for the sorption of Ir and Rh from liquid or gas phases.

The imidazole-terminated alkanethiol, Im-C_{11}-SH, studied in this dissertation was chosen for several reasons. The goal was to generate an alkanethiolate SAMs-based substrate with predefined properties of binding Ir and Rh from hydrochloric acid solutions. First of all, it is well-known that imidazolium-based ionic liquids have already been used in the Ir(IV) extraction from hydrochloric acid solutions reaching high distribution ratios of up to 71.4 [89]. The assumption was made that the imidazole-terminated alkanethiol would be effective in the binding of Ir(IV) as well. On the other hand, Rh(III) is extracted by imidazolium-based ionic liquids to a lower degree, and the extraction efficiencies were reported to be less than 10% [90]. Nevertheless, the idea was to compare the surface saturation of Im-C_{11}-SH SAMs with these two metals. Secondly, Im-C_{11}-SH is a commercially available compound that simplifies the procedure of SAMs preparation.

The second thiol, MDDA, was chosen to compare the metal sorption on SAMs with different functional groups.

1.5   Scope

In the first part of this project, the functionalization of gold-coated chips with Im-C_{11}-SH and MDDA SAMs, as well as Ir(IV) and Rh(III) sorption from hydrochloric acid solutions on Im-C_{11}-SH SAMs were studied. The results of this study were important for designing new functionalized gold-coated silicon detectors.

In the second part of this project, the named detectors were used during online cyclotron-based experiments aimed at studying the sorption of iridium, erbium, and astatine on non-functionalized and functionalized silicon detectors.

The results of this study can possibly be used to develop a chemical system suitable for the chemical characterization of Mt in the future.

CHAPTER II

EXPERIMENTS

2.1   Chemicals

Silicon wafers of 10 mm square in size and 525 μm thick were coated with a 100 nm Au(111) film that had been primed with titanium (5 nm) to promote adhesion between silicon oxide and gold; glass chips of aluminosilicate 10 mm square in size and 700 μm thick were coated with a 50 nm Au(111) film that had been primed with titanium (2.5 nm) (Platypus Technologies, LLC, USA). 1-(11-Mercaptoundecyl)imidazole (Im-C$_{11}$-SH, C$_{14}$H$_{26}$N$_2$S, 96% purity, Sigma-Aldrich, USA) and 12-mercaptododecanoic acid (MDDA, C$_{12}$H$_{24}$O$_2$S, 96% purity, Sigma-Aldrich, USA) were used without further purification. 30% (w/w) hydrogen peroxide solution in water was purchased from VWR BDH, USA. Ethanol (≥99.5% v/v) USP, 200 Proof, undenatured was provided by VWR, USA. Iridium Pure Plus Standard (1 μg/mL in 2% HCl) and Rhodium Pure Plus Standard (1 μg/mL in 2% HCl) were acquired from PerkinElmer, Inc., USA. Iridium (10 μg/mL in 30% HCl) and Rhodium (10 μg/mL in 30% HCl) Calibration Standard was purchased from Inorganic Ventures and used to prepare calibrators during instrumental neutron activation analysis. Praseodymium Standard (10 mg/mL in 7% HNO$_3$) was purchased from Inorganic Ventures, Inc., USA. 2-Propanol, anhydrous (assay ≥99.8%), DriSolv®, Supelco® was provided by VWR, USA.

2.2   Instruments and Analytical Techniques

Surface characterization techniques used for the measurement of the roughness, the surface coverage, the chemical state of SAMs, the kinetics of the SAMs degradation, the thickness of SAMs, and the surface saturation with Ir(IV) are described next.

2.2.1   Atomic Force Microscopy

The roughness measurements were acquired using a Bruker Dimension Icon AFM. All AFM images were obtained in scanning mode at room temperature using a rectangular Si_3N_4-coated cantilever. Before AFM analysis, a stream of dry N_2 was used to blow the dust particles off the analyzed surface. AFM images were analyzed in NanoScope Analysis© software.

2.2.2   Nanoprojectile Secondary-Ion Mass Spectrometry

A custom-built cluster-SIMS instrument, consisting of a liquid metal ion source of 520 keV Au_{400}^{4+} clusters, was employed to verify the presence of Im-C_{11}-SH SAMs on the gold surface, and measure the coverage with SAMs. During the experiments, the ions impacted the front side of the bulk target at an angle of incidence of 45° from normal. The secondary ions were emitted/detected in the reflection direction. The NP-SIMS instrument is equipped with a reflectron-type time-of-flight (ToF) mass spectrometer, and an electron emission microscope, EEM [91-95]. The EEM was used to detect secondary electrons for the ToF start signal. The secondary electrons, being detected as a magnified electron image, were used for the "electron collimator" of the bombarded area.

The data were acquired at the level of individual 520 keV Au_{400}^{4+} impacts with a repetition rate of 1000 impacts/s. This event-by-event bombardment-detection mode [96] allowed for the selection of specific impacts, in the present case those involving Im-C_{11}-SH SAMs at the exclusion of signals from the uncoated gold support.

Secondary ions emitted/detected via a single projectile impact were collected as an individual mass spectrum. The number of individual mass spectra is ~106. They were collected from an area of 500 μm in diameter. The sum of all mass spectra (total mass spectrum) corresponds

to the regular mass spectrum measured in the case of regular analysis by commercial NP-SIMS. The peak intensity was normalized to the total number of events during an experiment. All spectra were collected in negative mode meaning the negative bias was applied to a sample, therefore, negatively charged secondary ions were emitted/detected. The same setup was used to detect Ir and Rh clusters bound to Im-C$_{11}$-SH SAMs and measure SAMs coverage with the identified clusters.

2.2.3   X-ray Photoelectron Spectroscopy

An Omicron XPS/UPS system with Argus detector and Mg X-ray source, set to 250 W, was used to acquire X-ray photoelectron spectra. The analyzer pass energy was set to 40 eV. Spectra were calibrated by setting the center of the strong Au 4f$_{7/2}$ peak to 84.01 eV. XPS spectra were analyzed and fitted using the Marquardt method via CasaXPS© Software [97, 98]. To fit sulfur XPS spectra containing two S 2p spin-orbit split components (S 2p$_{3/2}$ and S 2p$_{1/2}$) the branching ratio and the energy difference were set to 2:1 and 1.2 eV, respectively [81, 99].

2.2.4   Ellipsometry

An ellipsometer Alpha-SE from J.A. Woollam Co. was employed for ellipsometric measurements. An angle of incidence was set to 70°, and all measurements were acquired in a standard mode with the data acquisition rate of 10 sec. CompleteEASE® software was used to measure the SAMs thickness. A refractive index (n) of 1.450 for SAMs was used [100, 101] which is a default Cauchy parameter. The Cauchy layer was used to fit the data and determine the thickness of SAMs.

2.2.5   Instrumental Neutron Activation Analysis (INAA)

This technique was utilized to measure the concentration of Ir(IV) and Rh(III) in the aqueous phase before and after sorption on non-functionalized and functionalized precleaned gold-coated substrates. The comparator method of INAA - in which calibrators and the experimental samples are irradiated, and gamma-ray emissions are counted under identical conditions - was employed [102].

Aliquots of 100 μL of the Ir and Rh calibrator solutions were accurately transferred by pipette and heat-sealed in pre-washed 2/5-dram polyethylene irradiation vials. 500 μL aliquots of initially 5.2 μM Ir(IV) experimental samples and 1000 μL aliquots of initially 0.52 μM, 1.0 μM Ir(IV) or 1.0 μM, 1.9 μM Rh(III) experimental samples in 0.55 M HCl were prepared in the same manner. The sample masses were determined with a calibrated analytical balance with a readability of 0.01 mg. The closed sample vials were weighed in an ambient atmosphere and heat-sealed before irradiation.

The neutron irradiations were performed simultaneously in the in-pool facility of the Texas Engineering Experiment Station (TEES) Nuclear Science Center 1 MW TRIGA (Training, Research, Isotopes, General Atomics) reactor. The subsequent gamma-ray spectrometry was performed using a high-purity Ge (HPGe) gamma-ray detector (from ORTEC), and the data reduction was done using INAA software from Canberra Industries. Technical details for Ir(IV) and Rh(III) measurements are presented in Table 6.

Table 6. Technical details of neutron irradiation and gamma-ray spectrometry of Ir(IV) and Rh(III) solutions.

	Ir(IV)	**Rh(III)**
Indicator Nuclide	^{192}Ir	^{104m}Rh
Indicator half-life	73.831 d	4.34 min
Indicator Gamma Ray	316.51 keV	51.42 keV
Thermal neutron flux	$9.1 \cdot 10^{12}$ cm$^{-2} \cdot$s^{-1}	$9.1 \cdot 10^{12}$ cm$^{-2} \cdot$s^{-1}
Irradiation Interval	2.0 h	120 s
Decay Interval	5-7 d	300 s
Counting Interval	4.00 h	300 s
Counting Distance	0.5 cm	0.5 cm
Gamma Spectrometer Dead Time	<15%	< 15%

2.2.6 Other Instruments

Im-C$_{11}$-SH was weighed using a Mettler Toledo NewClassic MF ML204/03 balance with the precision of 0.1 mg. A commercially available SkinAct UV-sterilizer with a timer and a bulb emitting UV light at 254 nm was used during the liquid-based hydrogen peroxide-mediated UV-photooxidation treatment.

2.3 Experimental Procedures

2.3.1 Preparation and characterization

2.3.1.1 Substrate pre-treatment

The procedure of precleaning the surface of gold-coated silicon samples, and their regeneration after SAMs deposition was designed based on a surface regeneration technique developed by Johnson and Mutharasan [103], in particular liquid-based hydrogen peroxide (H$_2$O$_2$)-mediated UV-photooxidation (liquid-UVPO) treatment. Such a technique could replace a more

aggressive and destructive method of Im-C$_{11}$-SH SAMs removal, involving a "piranha" solution [82].

A sample was placed into a Petri dish, and 170 μL of a 30% H$_2$O$_2$ solution was added to cover the whole surface area of the chip. The Petri dish was placed into the UV sterilizer, and the UV light was turned on for 30 min. After 30 min, the drop of H$_2$O$_2$ was refreshed to provide a high concentration of hydroxyl radicals. The Petri dish was placed back into the UV-sterilizer for 30 more min. Afterward, the chip was washed with a copious amount of a deoxygenated ethanol solution using a glass Pasteur pipette (around 10 times). The same procedure was used to remove thiolate SAMs from the surface during all experiments, except for XPS measurements where the sample was treated twice in a row. To prepare the deoxygenated ethanol solution, ethanol was briefly heated in a water bath of a rotary evaporator (T = 55°C, t = 15 min). The optimal rotation speed was 250 rpm.

2.3.1.2   Preparation of Im-C$_{11}$-SH and MDDA solutions

Im-C$_{11}$-SH and MDDA must be stored in a desiccator and refrigerated at 2-8 °C to prevent their decomposition [104, 105]. The melting points of Im-C$_{11}$-SH and MDDA are 26-31°C and 45-50 °C, respectively [104, 105]. After taking the vial with Im-C$_{11}$-SH out of the refrigerator but before weighing the chemical, it must be kept at ambient temperature until it turns from a white solid into a homogeneous viscous liquid. MDDA is a white powder and stays in solid form at ambient temperature. To prepare a 1.6 mM or a 5 mM thiol solution, an appropriate amount of Im-C$_{11}$-SH or MDDA was weighed into a 15 mL centrifuge tube. To dissolve the named thiols, 15 mL or 5 mL of a deoxygenated ethanol solution was added depending on the Im-C$_{11}$-SH or MDDA volume needed for experiments. The components were thoroughly mixed manually until

a homogeneous solution was formed. The preparation procedure was performed in a fume hood at ambient temperature. Structural formulas of Im-C_{11}-SH and MDDA are shown in Figure 9.

a)
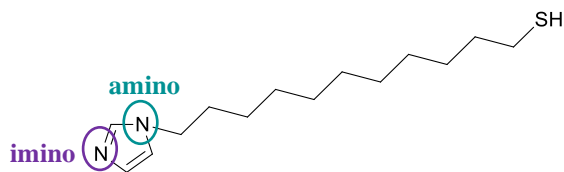
b)
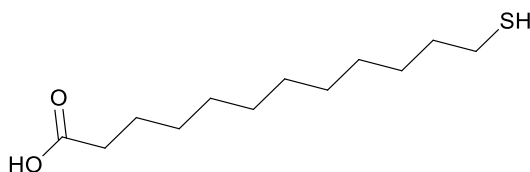
Figure 9. Structural formulas of: (a) Im-C_{11}-SH (highlighted are amino and imino nitrogen sites of the imidazole ring); (b) MDDA used for the preparation of the thiol solutions.

2.3.1.3   Formation of Im-C_{11}-SH and MDDA SAMs

The procedure of SAMs deposition was designed based on the works of Yamamoto *et al.* [106], Kato *et al.* [81], and Wei *et al.* [82]. The precleaned chip was placed into the bottom of a 50 mL plastic tube using tweezers with plastic tips. To fully cover the chip, 3 mL of the prepared 1.6 mM or 5 mM ethanolic Im-C_{11}-SH or MDDA solution was added. The plastic tube was wrapped with aluminum foil to avoid exposure to light. The cap of the tube was wrapped with Parafilm. The chip was submerged in the thiol solution for 21 h to ensure the formation of well-ordered, standing-up thiolate molecules in a closed-packed configuration, and the highest coverage [50, 51]. The immersion procedure was performed in the fume hood at ambient temperature.

The next day, the chip was taken out of the solution using tweezers with plastic tips. It was washed with a copious amount of the deoxygenated ethanol solution using a glass Pasteur pipette (approximately 10 times).

To dry the chip, a rubber bulb with a plastic tip was used to blow the residual drops off the surface. Then, a stream of compressed Ar gas was used to completely dry the surface.

The schematic structures of Im-C$_{11}$-SH and MDDA SAMs deposited on gold-coated silicon and glass chips are represented in Figure 10.
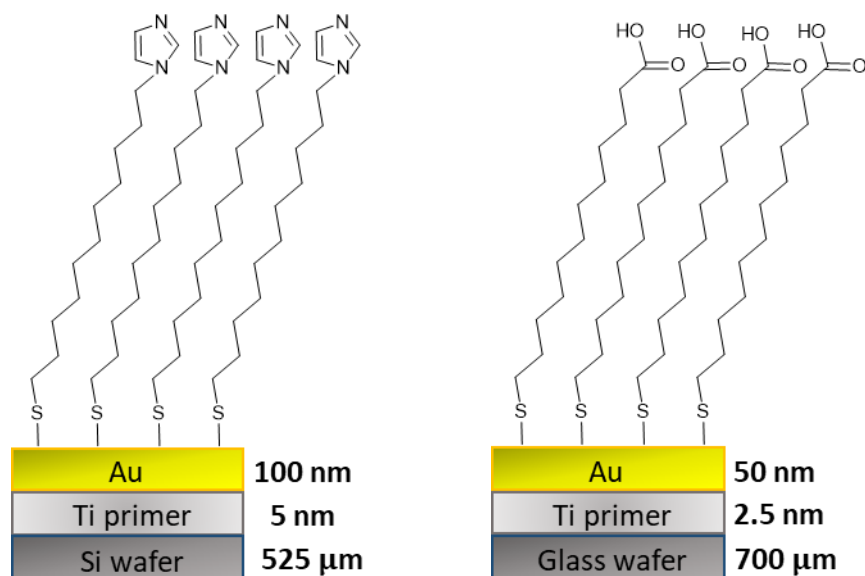
Figure 10. Schematic diagram of the substrates investigated in this study. All chips were 10 mm × 10 mm.

Chips with freshly prepared SAMs were analyzed on the same day. For kinetics studies of the SAMs degradation during the XPS analysis, chips were stored in wafer carrier trays wrapped with aluminum foil to avoid exposure to light. Wafer carrier trays were placed in a box stored in a closed cabinet.

2.3.2   Offline Experiments

2.3.2.1   Ir(IV) and Rh(III) sorption on gold-coated substrates

Bare gold-coated chips, as well as gold-coated chips functionalized with Im-C$_{11}$-SH SAMs, deposited from 5 mM ethanolic thiol solutions, were placed into 5 mL plastic tubes. Then, 2 or 3 mL of Ir(IV) and Rh(III) solutions of the target concentration in 0.55 M HCl were added separately into 5 mL plastic tubes containing the chips. During the INAA analysis, 2 mL of 5.2 µM Ir(IV) solution was added. Subsequently, for 0.5 µM or 1.0 µM Ir(IV) concentrations, 3 mL of the corresponding solution was added to simplify taking an aliquot needed for the INAA measurements. For the metal sorption from 0.5 µM, 5.2 µM Ir(IV), or 1.0 µM Rh(III) solutions, the non-functionalized and functionalized silicon chips coated with 100 nm of gold were employed. For the metal sorption from 1.0 µM Ir(IV) or 1.9 µM Rh(III) solutions, the non-functionalized and functionalized glass chips coated with 50 nm of gold were used. During the NP-SIMS analysis, the metal sorption from 3 mL of 5.2 µM Ir(IV) or 9.7 µM Rh(III) solutions in 0.55 M HCl was performed on the non-functionalized and functionalized glass chips coated with 50 nm of gold.

During both analyses, the non-functionalized and functionalized chips were left in contact with the metal solutions for approximately 21 h. The plastic tubes were wrapped with aluminum foil to avoid exposure to light. The cap of the tube was wrapped with Parafilm. The next day, the chips were taken out of the solutions using tweezers with plastic tips.

The solutions that were in contact with the functionalized chips, as well as solutions with the initial metal concentration, were analyzed with INAA. Aliquots of 100 µL of the Ir calibrator solution were accurately transferred by pipet and heat-sealed in pre-washed 2/5-dram polyethylene irradiation vials. 500 µL aliquots of initially 5.2 µM Ir(IV) experimental samples and 1000 µL

aliquots of initially 0.52 µM, 1.0 µM Ir(IV) or 1.0 µM, 1.9 µM Rh(III) experimental samples in 0.55 M HCl were prepared in the same manner. The sample masses were determined with a calibrated analytical balance with a readability of 0.01 mg. The closed sample vials were weighed in an ambient atmosphere and heat-sealed before irradiation.

Prior to the NP-SIMS analysis, the chips were washed with a copious amount of 0.55 M HCl solution using a glass Pasteur pipette (approximately 10 times). To dry the chips, a stream of compressed Ar gas was used.

2.3.3   Online Cyclotron-Based Experiments

The experiments described in this dissertation were performed at the Cyclotron Institute, Texas A&M University in two temporally separated experiments. The Cyclotron Institute has a normal conducting K150 and a superconducting K500 cyclotron. A schematic of the facility is illustrated in Figure 11.
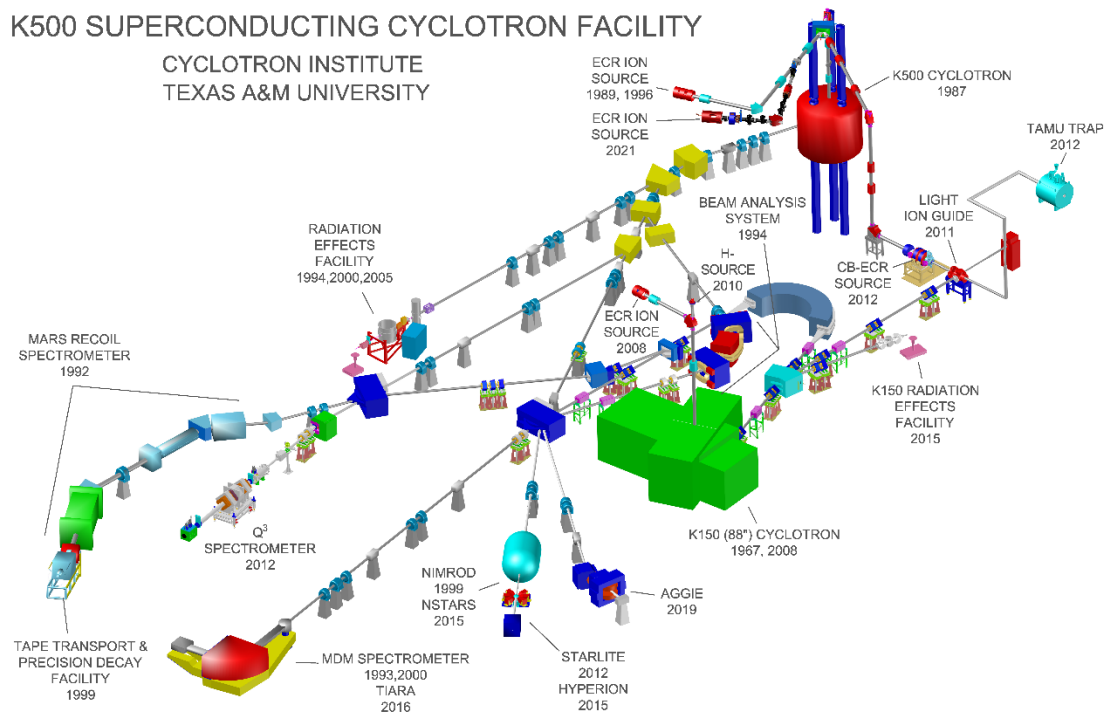
Figure 11. A scheme of the normal conducting K150 cyclotron used in this study, and the superconducting K500 cyclotron.

A schematic of the online cyclotron-based experiment performed in this study is depicted in Figure 12. During a fusion-evaporation reaction, the accelerated $^{40}Ar^{11+}$ beam, produced by the K150 conducting cyclotron, bombards a target in the target chamber; this is where a nuclear reaction occurs. Afterward, the produced ions of interest enter a system of magnets, namely the AGGIE (Al Ghiorso's Gas-filled Ion Equipment) separator. It is used to separate the ions of interest from the beam and other unwanted reaction products. Then, the ions of interest go through a rotating degrader and, finally, enter a simple Recoil Transfer Chamber (sRTC). It has been designed and used for the first time to study the chemical behavior of the produced nuclides on chemically modified and non-modified silicon detectors. The details of the experimental setup are discussed next.
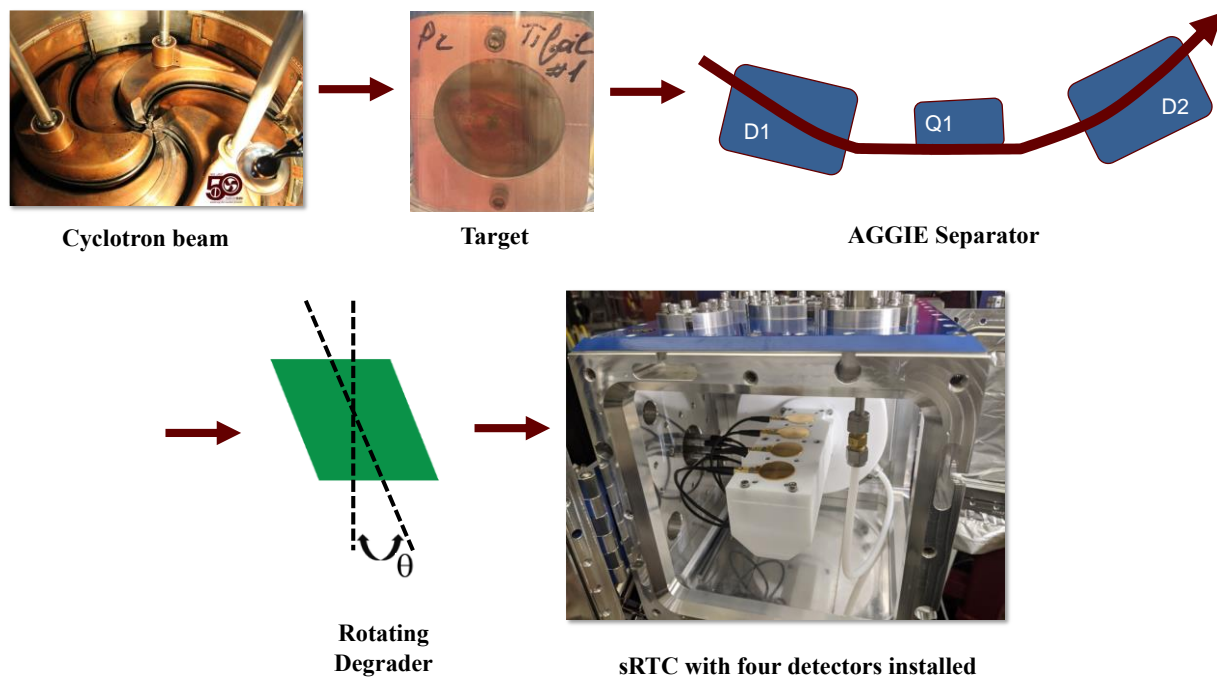
Figure 12. Schematic of the online cyclotron-based experiment.

2.3.3.1   Reactions of interest

Initially, the reaction $^{141}Pr(^{40}Ar, 5n)^{176}Ir$ was chosen to study the sorption of ^{176}Ir on chemically modified and non-modified silicon detectors. During the first experiment, the beam energy was 6.3 MeV/u (252 MeV), and the count rate of ^{176}Ir was low due to several reasons. Firstly, the $^{141}Pr(^{40}Ar, 5n)^{176}Ir$ reaction has the low cross-section of 1-10 mb [107], and ^{176}Ir has a low alpha branching ratio of 2.6% [108]. The half-life of ^{176}Ir is 8.6 ± 0.4 s [108]. Secondly, the quadrupole magnet of the AGGIE separator did not have enough field to properly focus the product into the simple Recoil Transfer Chamber, so the efficiency of the separator was too low. As a result, we switched to the reaction $^{118}Sn(^{40}Ar, 5n)^{153}Er$ which has the higher cross-section of ~50 mb [109]. ^{153}Er has an alpha branching ratio of 53% and the half-life of 37.1 ± 0.2 s [110]. The first experiment was a proof of principle and is not discussed in this dissertation. After a few

36

improvements were implemented, the second experiment was performed. The beam energy was increased to 6.9 MeV/u (276 MeV). During this experiment, three fusion-evaporation reactions were performed: ^{118}Sn(^{40}Ar, 5n)^{153}Er, ^{165}Ho(^{40}Ar, 5n)^{200}At, and ^{141}Pr(^{40}Ar, 5n)^{176}Ir. The ^{165}Ho(^{40}Ar, 5n)^{200}At reaction has the cross-section of ~10 mb [111]. ^{200}At has the alpha branching ratio of 57% and the half-life of 43 ± 1 s [112]. Alpha-decay information for the named nuclides is summarized in Table 7. The results of the second experiment are discussed in detail in Section 3.4 of this dissertation.

Table 7. Alpha-decay information for the produced nuclides and the cross-sections of the corresponding reactions.

	^{176}Ir	^{153}Er	^{200}At
$T_{1/2}$, s	8.6 ± 0.4	37.1 ± 0.2	43 ± 1
I, %	2.6	53	57
σ, mb	1-10	~50	~10

where $T_{1/2}$ is the half-life of a nuclide, I is the α-branching ratio, σ is the cross-section of a corresponding nuclear reaction.

2.3.3.2 Target Chamber

The target chamber illustrated in Figure 17 has three ladders attached to telescoping arms that are controlled remotely. The ladders and telescoping arms are shown in Figure 13 and Figure 14, respectively. At first, the beam goes through the degrader ladder with mounted aluminum degraders of various thicknesses (1.2-6.29 μm), including a blank. They are used to decrease the beam's energy and build the excitation function. This enables the selection of an appropriate degrader for a particular nuclear reaction at which the count rate of a produced nuclide is the highest.
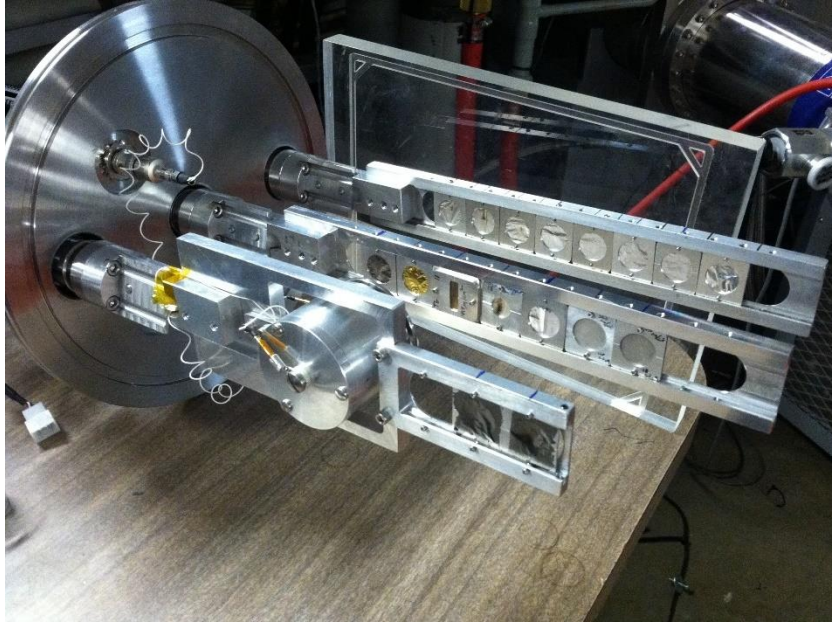
Figure 13. From top to bottom: degrader, target, and Faraday cup ladders. Reprinted from ref. [113].

Figure 14. Three telescoping arms attached to the ladders allowing the remote control over them. Reprinted from ref. [113].

The next ladder the beam goes through is the target ladder which has a variety of targets mounted on it as shown in Figure 13. Remote access to the target ladder allows putting in place a specific target needed for a particular nuclear reaction. The target position is aligned with the beam trajectory so that the beam hits the center of the selected target.

For the ^{118}Sn(^{40}Ar, 5n)^{153}Er reaction, a ^{118}Sn 428 μg/cm^2 target (97.06% purity, purchased from Microfoils Co, Arlington, Washington, USA) on a 20 μg/cm^2 ^{nat}C backing was used. For the ^{165}Ho(^{40}Ar, 5n)^{200}At reaction, a ^{165}Ho 300 μg/cm^2 target (purchased from MicroMatter, British Columbia, Canada) on a 1.08 μm ^{nat}Al backing was used. The aluminum degrader of 6.29 μm was used for these two reactions. For the ^{141}Pr(^{40}Ar, 5n)^{176}Ir reaction, a ^{141}Pr$_2$O$_3$ 400 μg/cm^2 target on a 2 μm titanium (Ti) foil (99.6% purity, purchased from Goodfellow Corporation, Pittsburg, Pennsylvania, USA) was used. No aluminum degrader was used for this reaction. The target was made using the electrodeposition technique [114-117]. A schematic of the electrodeposition cell is shown in Figure 15.
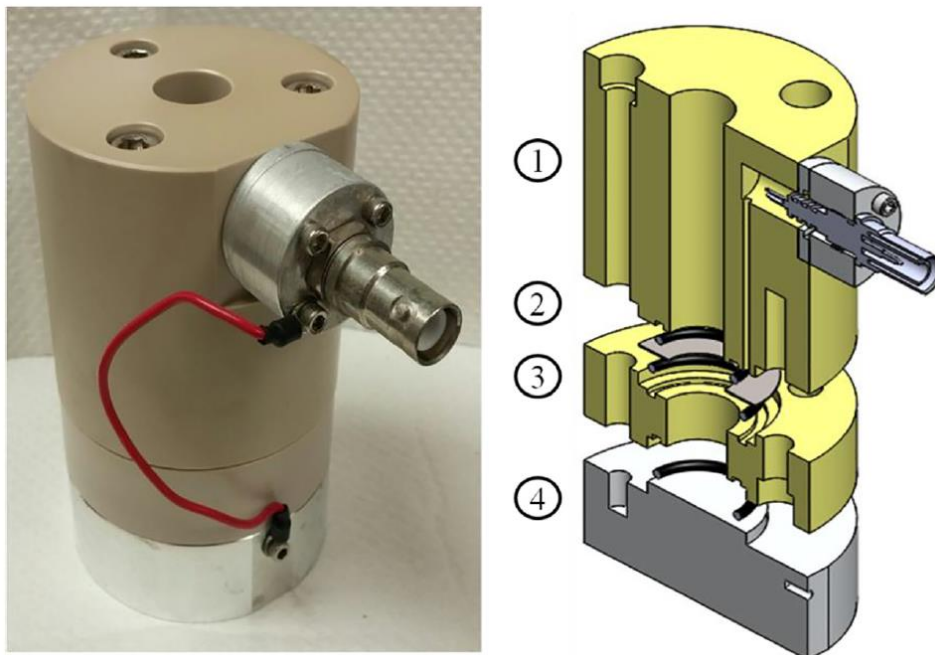
Figure 15. Electrodeposition cell used in this study to make the $^{141}Pr_2O_3$ 400 $\mu g/cm^2$ target. (1) The main body made of polyetheretherketone (PEEK); (2) platinum anode; (3) PEEK centerpiece; (4) aluminum cathode. Figure used with permission from ref. [117].

The Ti backing was weighed and placed on the bottom of the main body of the electrodeposition cell. Then, 125 µL of Praseodymium (Pr) Standard (10 mg/mL in 7% HNO_3) was added to a polytetrafluoroethylene crucible and evaporated to almost dryness at 80°C on a hot plate for approximately 40 min. The product was dissolved in 2-propanol and transferred into the main body of the electrodeposition cell making the total volume of 10 mL of the deposition solution. The electrodeposition was performed at constant voltage for 45 min starting at 500 V and finishing at 250 V by decreasing it by 50 V stepwise until the current curve reached the plateau. The resulting plot containing the current (orange) and the voltage (blue) curves is observed in Figure 16.
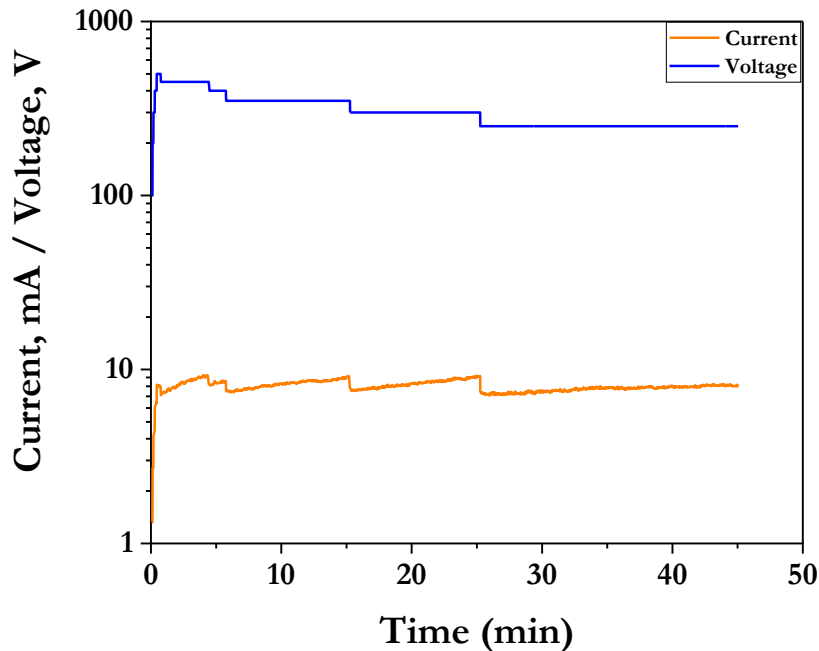
Figure 16. Current (orange curve) and voltage (blue curve) as a function of time.

The obtained target with the electrodeposit in a form of $^{141}Pr_2O_3$ was weighed after drying and baking it in the air at 200°C for 30 min, and the areal density of 400 μg/cm^2 was obtained. The target was placed into an aluminum frame before mounting it on the target ladder.

The backings of the targets faced the incident beam during the experiments. The resulting energies of the beam bombarding the ^{118}Sn, the ^{165}Ho, and the $^{141}Pr_2O_3$ targets were 5.51 MeV/u (220 MeV), 5.46 MeV/u (218 MeV), and 5.75 MeV/u (230 MeV), respectively. The energy loss was caused by the beam going through a 15 μm aluminum window, followed by the particular aluminum degrader for each nuclear reaction, and the backing of each target. The named aluminum window is located upstream of the target chamber to separate the 0.5 Torr pressure inside the separator from the vacuum in the beamline. The total number of incident ions of $^{40}Ar^{11+}$ beam on the ^{118}Sn, the ^{165}Ho, and the $^{141}Pr_2O_3$ targets were $5.6 \cdot 10^{15}$, $6.1 \cdot 10^{15}$, and $9.7 \cdot 10^{15}$ ions.

41

A Faraday cup illustrated in Figure 13 is attached to the third ladder and allows to measure the primary beam intensity when it is put in place. During a nuclear reaction, the Faraday cup is set to a position that is out of the beam's trajectory.

Lastly, the target chamber has two silicon detectors, called Rutherford East and West, located $\pm 30°$ from the beam axis and used to detect deflected beam nuclei. The ion source and the cyclotron performance can cause fluctuations in the beam intensity during the experiment. Additionally, the areal density of the target might decrease in time due to the target sputtering created by the intense beam. These changes can be accounted for by normalizing the total number of events of a produced nuclide to the mean of Rutherford scattering events collected on the Rutherford East and West detectors. Also, the Rutherford detectors can be used to control the alignment between the beam and the target.

Finally, after hitting the target, the desired reaction products and the unreacted beam particles enter the AGGIE gas-filled separator.

2.3.3.3   AGGIE gas-filled separator

The separator was originally designed at Lawrence Berkley National Laboratory and named SASSY II [118] which was an improved version of the previous separator named SASSY [119]. It was later transferred to the Wright Nuclear Structure Laboratory of Yale University and named SASSYER [120]. Eventually, it was transferred to the Cyclotron Institute, Texas A&M University, and named AGGIE. Characterization of the AGGIE separator using beam has begun in 2019 and is currently in progress [121].

AGGIE consists of two vertically focusing dipole magnets and one horizontally focusing quadrupole magnet placed between them in the configuration $D_v Q_h D_v$ [120, 121]. The effective

length of the three magnets is approximately 2.5 m [121]. A picture of AGGIE is illustrated in Figure 17.
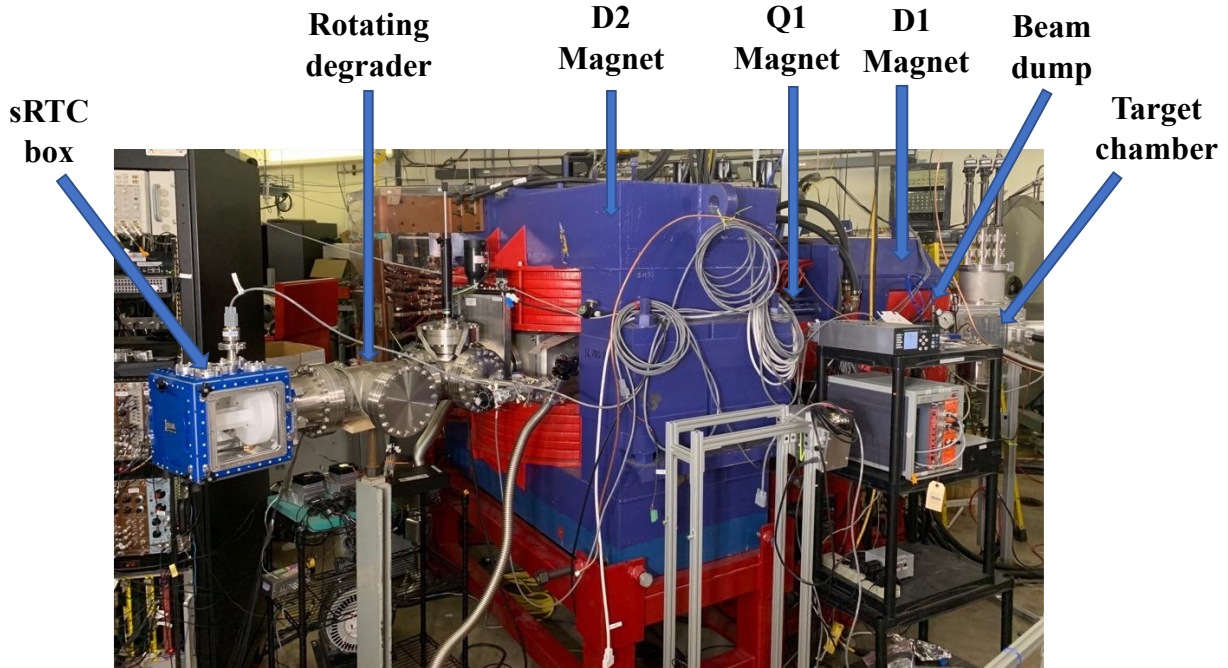
Figure 17. The AGGIE heavy element separator. Blue arrows show its main components.

The purpose of AGGIE is to separate the produced ions of interest from the primary beam [120]. The separation is done based on their magnetic rigidity, $B\rho$, defined as the momentum of an ion, mv, divided by its charge state, q:

$$B\rho = \frac{\gamma mv}{q},$$

Eq. 4

where B is the strength of a magnetic field, ρ is the radius of curvature of motion, γ is the Lorentz factor, m and v are the ion mass and velocity, respectively.

During the experiment described in this dissertation, the magnet chamber was filled with 0.5 Torr of helium (He) gas which provided charge equilibration of fusion-evaporation reaction products. This results in the narrower distribution of the product's magnetic rigidity and much

higher transmission through the separator compared to vacuum devices which can accept only up to two charge states [120, 121].

The magnetic fields of two dipole magnets D1 and D2 were tuned to bend the ions through the separator along the central axis. At the same time, the unreacted beam particles, which had a lower magnetic rigidity and lower radius of curvature, were stopped and collected in a beam dump box [120] located in front of the D1 magnet as shown in Figure 17. The magnetic field of a quadrupole magnet Q1 was tuned to bend the ions through the separator away from the central axis. Therefore, the separation of ions from the primary beam can be achieved following the target.

2.3.3.4   Simple Recoil Transfer Chamber

A simple Recoil Transfer Chamber (sRTC), composed of a funnel and a detector chamber, has been designed and used for the first time. Figure 17 illustrates the sRTC installed on the AGGIE separator. Figure 18 shows a closer view of the components of the sRTC and its cross-sectional view. The goal of the sRTC is to stop the ions of interest in the funnel by their collision with atoms of helium gas (350 Torr) which goes through the sRTC with a flow of 500-1800 standard cubic centimeters per minute. In turn, this enables more efficient sorption and detection of the named nuclides on the non-modified and modified silicon detectors located in the detector chamber. To separate the volumes of the sRTC and the separator operating at different pressures, an aluminized Mylar window (2 μm) was mounted at the entrance of the sRTC which is displayed in Figure 18 and Figure 19.
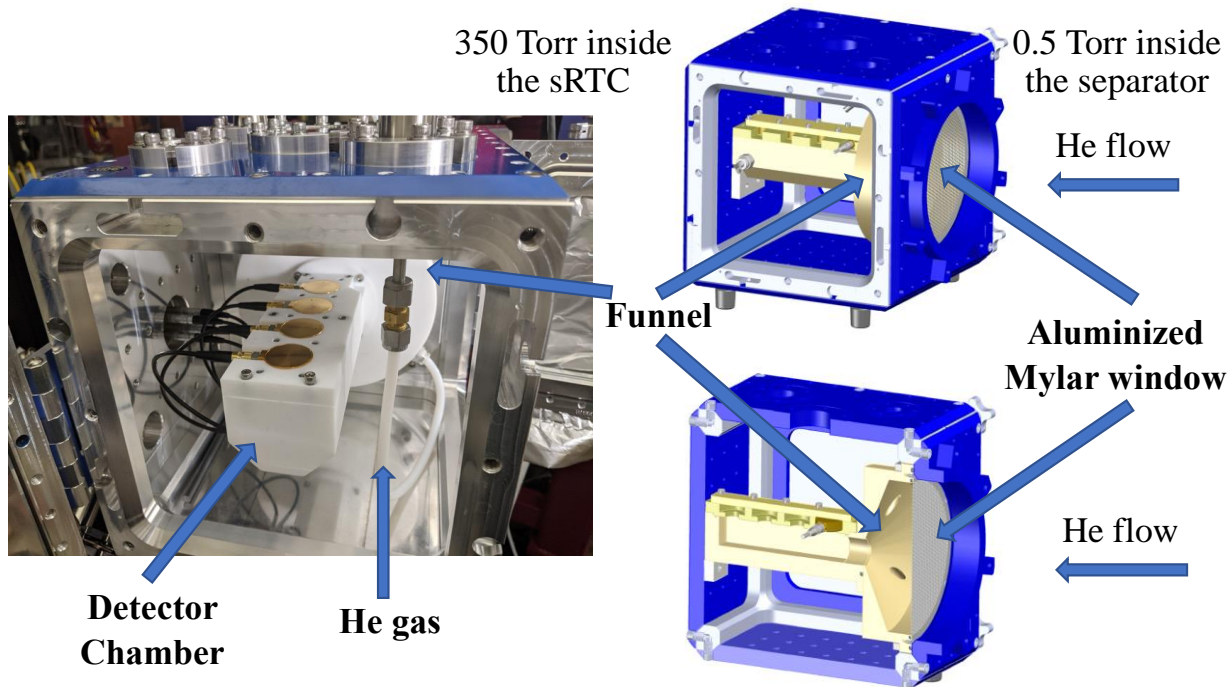
Figure 18. The left panel shows circular, gold-colored detectors installed inside the sRTC. The right panel shows schematic images of the sRTC including its cross-sectional view.

Figure 19. Aluminized Mylar window dismounted from the sRTC.

In addition, a rotating degrader made of Mylar (4 μm) was installed upstream of the sRTC inside the T connector; its location is indicated by a blue arrow in Figure 17. Changing the angle of the rotating degrader (0-75 degrees) results in the increase or decrease of the effective thickness of the material (4.0-15.5 μm) the ions are going through. As a result, it was possible to select a rotating degrader angle at which the ions were stopped mostly in the funnel due to their energy loss while traveling through the rotating degrader material of the corresponding thickness and an aluminized Mylar window. Consequently, this increased the count rate of a produced nuclide.

2.3.3.5   Detector Chamber

The detector chamber inside the sRTC depicted in Figure 18 has four slots for silicon detectors that were purchased from AMETEK ORTEC (Oak Ridge, Tennessee, USA). The SAMs deposition procedure used during offline experiments was transferred to online cyclotron-based experiments to prepare functionalized gold-coated silicon detectors. At first, three silicon detectors were coated with 50 nm of gold after being primed with 2.5 nm of titanium by Platypus Technologies, LLC (Madison, Wisconsin, USA). The left image in Figure 20 shows two silicon detectors, one bare silicon and one having silicon coated with gold. Before the gold coating, the silicon detectors were masked with aluminum foil to avoid the coating of the detector housing with gold.
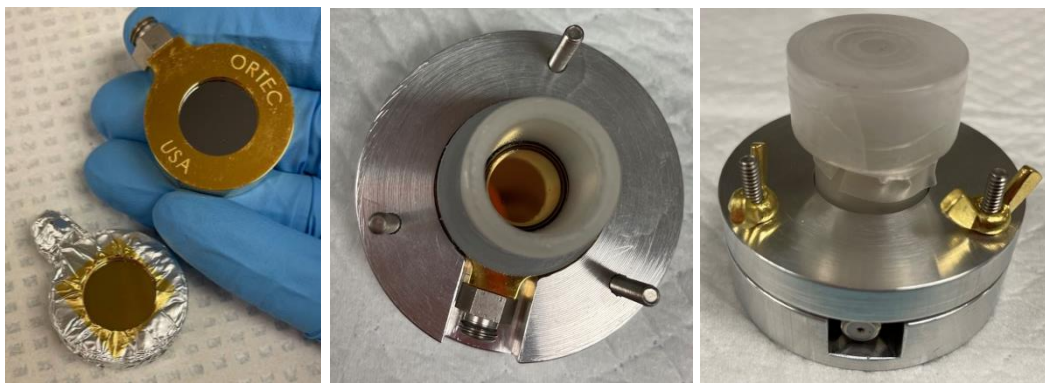
Figure 20. Silicon and gold-coated silicon detectors (left image), "chimney" placed onto the gold-coated silicon detector (center image), and the sealed "chimney" (right image).

After this, Im-C$_{11}$-SH or MDDA SAMs were deposited on two gold-coated silicon detectors from 5 mM ethanolic solutions of the corresponding thiols. Before depositing thiol solutions onto the surface of detectors, they need to be precleaned to get rid of any adventitious organic molecules present on the surface of gold. For that, two gold-coated silicon detectors were placed in a Petri dish and exposed to UV light of the UV-sterilizer for 1.5 h. Then, the surface of gold was washed with a deoxygenated ethanol solution approximately 10 times using a glass Pasteur pipette and a so-called "chimney" illustrated in Figure 20 that was designed for this study. The substrate pretreatment technique that involves adding the H$_2$O$_2$ solution onto the detector surface coupled with the UV light exposure was found to damage the surface of gold by peeling it off completely. As a result, H$_2$O$_2$ was excluded from the precleaning technique leaving only the UV light factor. The preparation of ethanolic thiol solutions is identical to that described in Section 2.3.1.2. An aliquot of 3 mL of 5 mM Im-C$_{11}$-SH or MDDA ethanolic solution was added onto the detector surface using a "chimney". It allowed a thiol solution to be in contact only with the detector surface preventing damaging the detector if it was submerged into the solution. The "chimney" was sealed with a cap wrapped with Parafilm to avoid exposure to air, and aluminum foil was wrapped around the "chimney" to avoid exposure to light. The thiol solution was left in

contact with the detector surface for 21 h. The SAMs deposition was performed twice to obtain the highest surface coverage. So, the next day, the thiol solution was poured into the thiol waste, and the detector surface was washed with an ethanol solution approximately 10 times using a glass Pasteur pipette and the "chimney". To dry the detector surface, a stream of compressed Ar gas was used. To remove the SAMs before the second deposition, the detector was exposed to UV light for 2 h.

Photooxidation of SAMs by exposure to UV light has already been studied before [122, 123]. It was suggested that UV-induced so-called "hot" electrons tunnel from the gold substrate to the empty electronic states of the sulfur atoms which initiates their excitation and the formation of anionic radicals [122, 123]. In turn, they react with oxygen molecules that penetrate the SAM-substrate interface and form sulfinates as a result [122, 123]. Sulfinates can disproportionate or be oxidized to sulfonates which can be washed away with ethanol followed by the release of alkyl chains [103, 122, 123]. The SAMs photooxidation mechanism proposed by Yan *et al.* [122] is depicted in Figure 21.

The next step after the SAMs removal was to wash the detector surface with a deoxygenated ethanol solution approximately 10 times as described above. Then, an aliquot of 3 mL of 5 mM Im-C_{11}-SH or MDDA ethanolic solution was added onto the detector surface using a "chimney" for the second time. After 21 h of the SAMs deposition, the thiol solution was poured into the thiol waste. The detector surface was washed with a deoxygenated ethanol solution approximately 10 times as it was described above and dried using a stream of compressed Ar gas. The functionalized gold-coated silicon detectors were placed into the detector chamber.
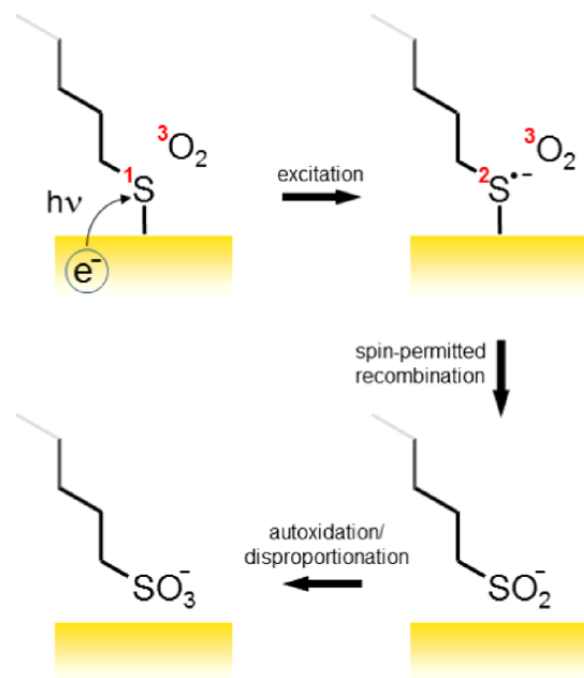
Figure 21. The SAMs photooxidation mechanism. Reprinted with permission from R. Yan, A. Terfort, and M. Zharnikov, J. Phys. Chem. C **125**, 1855 (2021). Copyright 2022 American Chemical Society.

Two other detectors inside the detector chamber were a bare silicon detector and a non-functionalized gold-coated silicon detector. Different detector surfaces were used during the online experiment to compare the sorption of produced nuclides on them. The collected alpha spectra and the data analysis are discussed in Section 3.4.

2.3.3.6   Alpha Spectrometry

Alpha spectrometry was performed to measure the resolution of the silicon detectors before and after their coating with gold, as well as after using the functionalized gold-coated silicon detectors during online cyclotron-based experiments. A model 7401 single channel alpha spectrometer with a Multiport II MCA illustrated in Figure 22 was calibrated against a NIST-traceable four-peak alpha calibration source containing ^{148}Gd, ^{239,240}Pu, ^{241}Am, and ^{244}Cm.
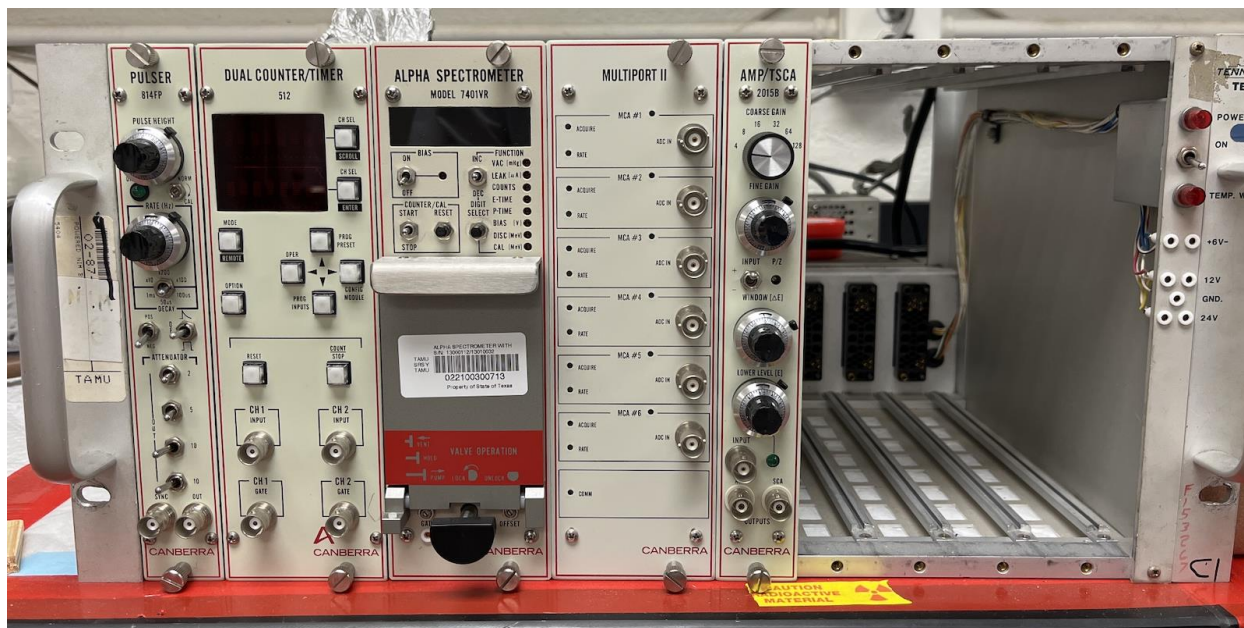
Figure 22. Alpha spectrometer used to measure the detector resolution.

The four-peak alpha source was mounted onto the door of the vacuum chamber so that the distance between an analyzed detector and the source was 1.5 cm. Alpha spectra were acquired and analyzed using Genie™ 2000 Gamma Analysis Software. The collected alpha-spectra and the results of the resolution analysis are discussed in Section 3.4.1.6.

CHAPTER III

RESULTS AND DISCUSSION

3.1   Characterization of Im-C_{11}-SH and MDAA SAMs on gold-coated chips

Surface characterization techniques used for the measurement of the roughness, the surface coverage, the chemical state of SAMs, the kinetics of the SAMs degradation, the thickness of SAMs, and the surface saturation are described next. Technical details of the utilized techniques are provided in chapter 2.

3.1.1   Evaluation of the roughness of non-functionalized and functionalized gold-coated silicon chips

AFM was employed to evaluate the roughness of a bare gold surface (i.e. after precleaning using the liquid-UVPO treatment), and gold substrates functionalized with Im-C_{11}-SH SAMs deposited from 5 mM ethanolic thiol solutions. The AFM images (10×10 μm) are shown in Figure 23. Image Rq is the root mean square average of the profile heights over the evaluation length, which gives information about the surface roughness. The Image Rq value for a bare gold surface is 1.20 nm as shown in Figure 23a. The surface roughness of gold subsequently functionalized with Im-C_{11}-SH SAMs is 1.20 nm as illustrated in Figure 23b. The roughness was also evaluated for the substrate which underwent the second SAMs deposition from a 5 mM ethanolic Im-C_{11}-SH solution after the removal of SAMs obtained during the first deposition from a 1.6 mM ethanolic Im-C_{11}-SH solution. As will be discussed later, the chips were tested on whether they can be reused by using the liquid-UVPO treatment [103] to remove SAMs, and depositing SAMs for the second time. The Image Rq value of the named substrate is 1.25 nm as depicted in Figure 23c.

a) Image Rq=1.20 nm

11.0 nm

2 μm

b) Image Rq=1.20 nm

13.4 nm

2 μm

c) Image Rq=1.25 nm

11.5 nm

2 μm
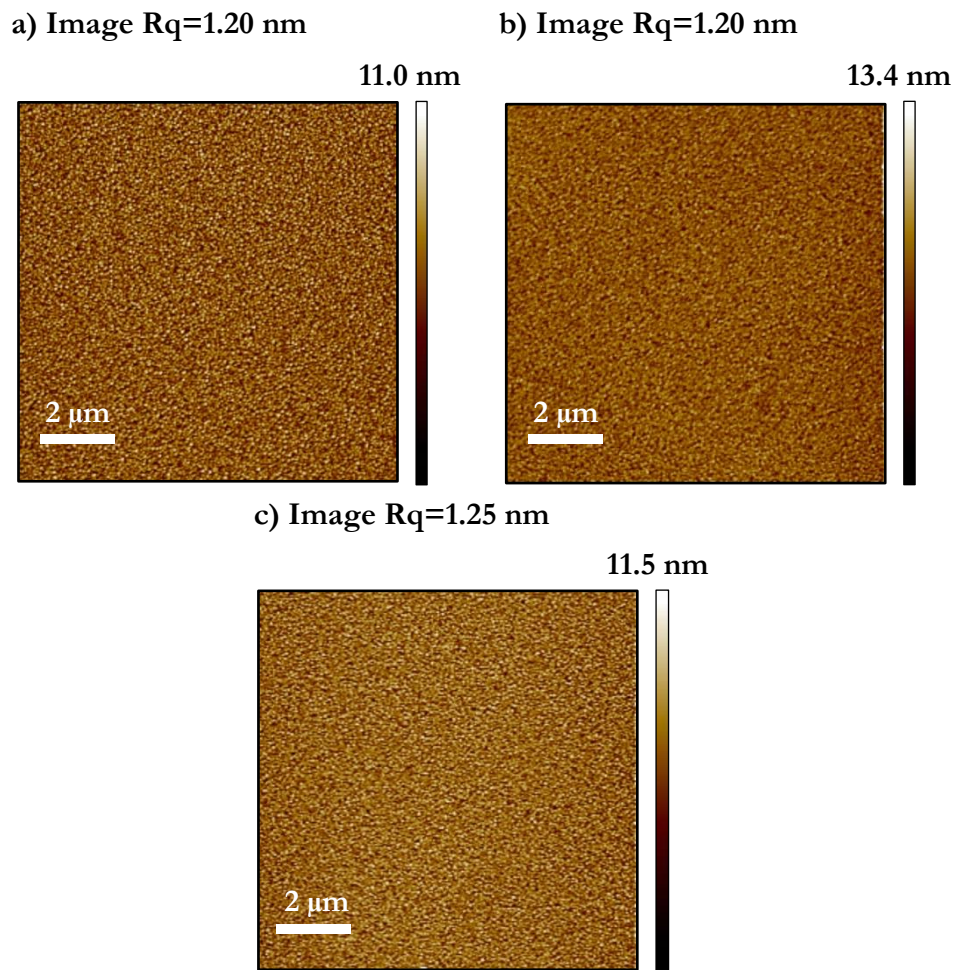
Figure 23. AFM images (10 × 10 μm) of (a) pure precleaned Au, (b) Im-C$_{11}$-SH SAMs on precleaned Au (the first deposition), (c) Im-C$_{11}$-SH SAMs on precleaned Au (the second deposition).

The comparison of the similar AFM images and the Image Rq values, which remain in the same range, suggests that the first and the second SAMs depositions, as well as the liquid-UVPO treatment, do not produce a macroscopic change to the surface morphology and topography, and as a result, the substrates can be reused without noticeable surface damage.

In the corresponding 2×2 μm AFM images provided in Figure 24, the grains of gold can be observed.
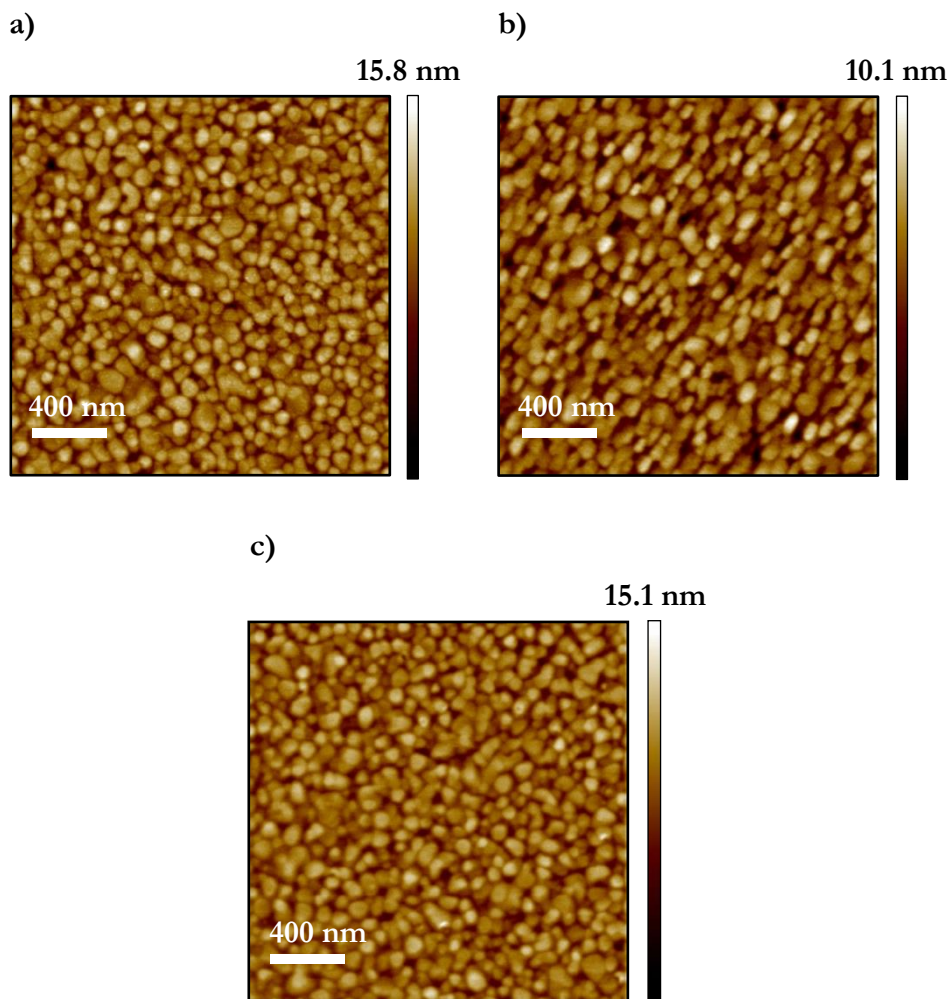
Figure 24. AFM images (2 × 2 μm) of (a) pure precleaned Au, (b) Im-C$_{11}$-SH SAMs on precleaned Au (the first deposition), (c) Im-C$_{11}$-SH SAMs on precleaned Au (the second deposition).

3.1.2   Measurement of the coverage of gold-coated silicon chips with Im-C$_{11}$-SH SAMs

NP-SIMS was used to identify the presence of Im-C$_{11}$-SH SAMs on gold and measure the surface coverage with the organic molecules. The total mass spectra in Figure 25a,26a were acquired for the substrate which was submerged into a 1.6 mM ethanolic Im-C$_{11}$-SH solution for the first time. The chip was not precleaned with the liquid-UVPO treatment before the SAMs deposition.

The total mass spectra in Figure 25b,26b were acquired for the substrate which was submerged into a 5 mM ethanolic Im-C_{11}-SH solution, the SAMs deposition was done for the second time. This means the gold surface was regenerated before the second deposition by removing SAMs obtained during the first deposition from a 1.6 mM ethanolic Im-C_{11}-SH solution. The liquid-UVPO treatment was used to remove SAMs. Our results on the regeneration efficacy will be explained in the XPS Section 3.1.3.

In both cases, the spectra were obtained by normalization of the intensity of the detected fragments to the total number of impacts emitted during the SIMS experiment.

As was mentioned above, the method of event-by-event bombardment-detection allows the selection of specific impacts, in the present case those involving SAM-related molecular fragments.

In Figure 25, the mass spectra contain characteristic peaks of the following Im-C_{11}-SH SAMs-Au fragments: hydrocarbon peaks $C_xH_y^-$, CN^-, S^-, SH^-, S_2^-, $C_3N_2H_3CH^-$. The latter one is a product of the imidazole ring fragmentation.

In Figure 26-28, the mass spectra contain characteristic peaks of the following Im-C_{11}-SH SAM-Au fragments: gold-sulfur clusters Au_nS^- (229, 426, 623, 820, 1017 amu), $AuSC_xH_y^-$ (253, 255 amu), a deprotonated monomer (Im-C_{11}-S^-) (253.2 amu), a gold-molecule cluster ion $Au(Im-C_{11}-S^-)_2$ (703 amu). Their observation verifies that Im-C_{11}-SH molecules are self-assembled on the surface of gold, forming the strong Au-S bond at the metal–thiol interface [124].

Mass (amu)	Fragment
12	C^-
13	CH^-
16	O^-
24	C_2^-
26	CN^-
32	S^-
33	SH^-
36	C_3^-
42	CNO^-
48	C_4^-
60	C_5^-
64	S_2^-
72	C_6^-
74	$C_6H_2^-$
80	$C_3N_2H_3CH^-$
84	C_7^-
97	C_8H^-
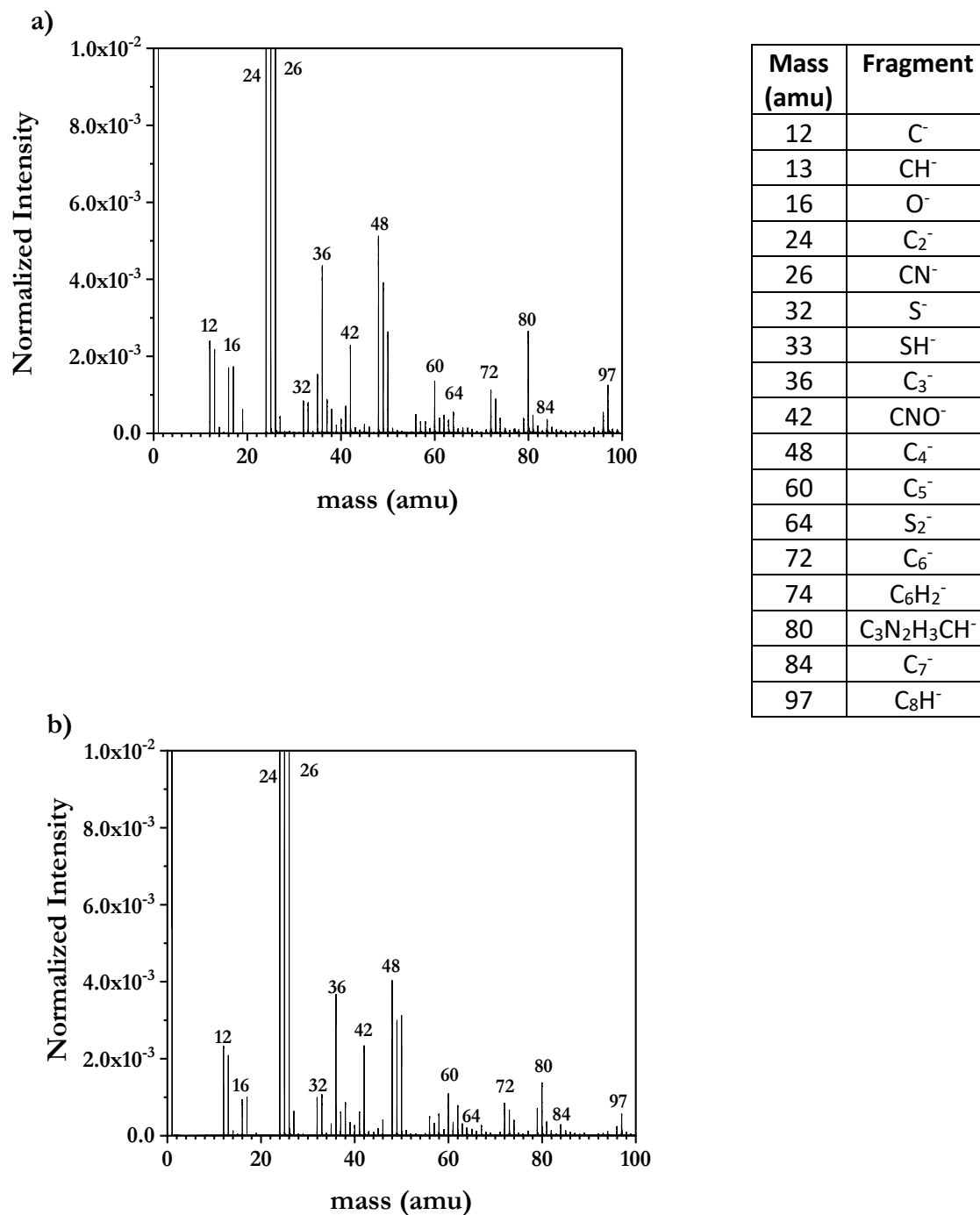
Figure 25. (a) Mass spectrum of non-precleaned Au functionalized with Im-C_{11}-SH SAMs deposited from a 1.6 mM ethanolic thiol solution during the first deposition. (b) Mass spectrum of precleaned Au functionalized with Im-C_{11}-SH SAMs deposited from a 5 mM ethanolic thiol solution during the second deposition. Mass range of 0-100 amu.
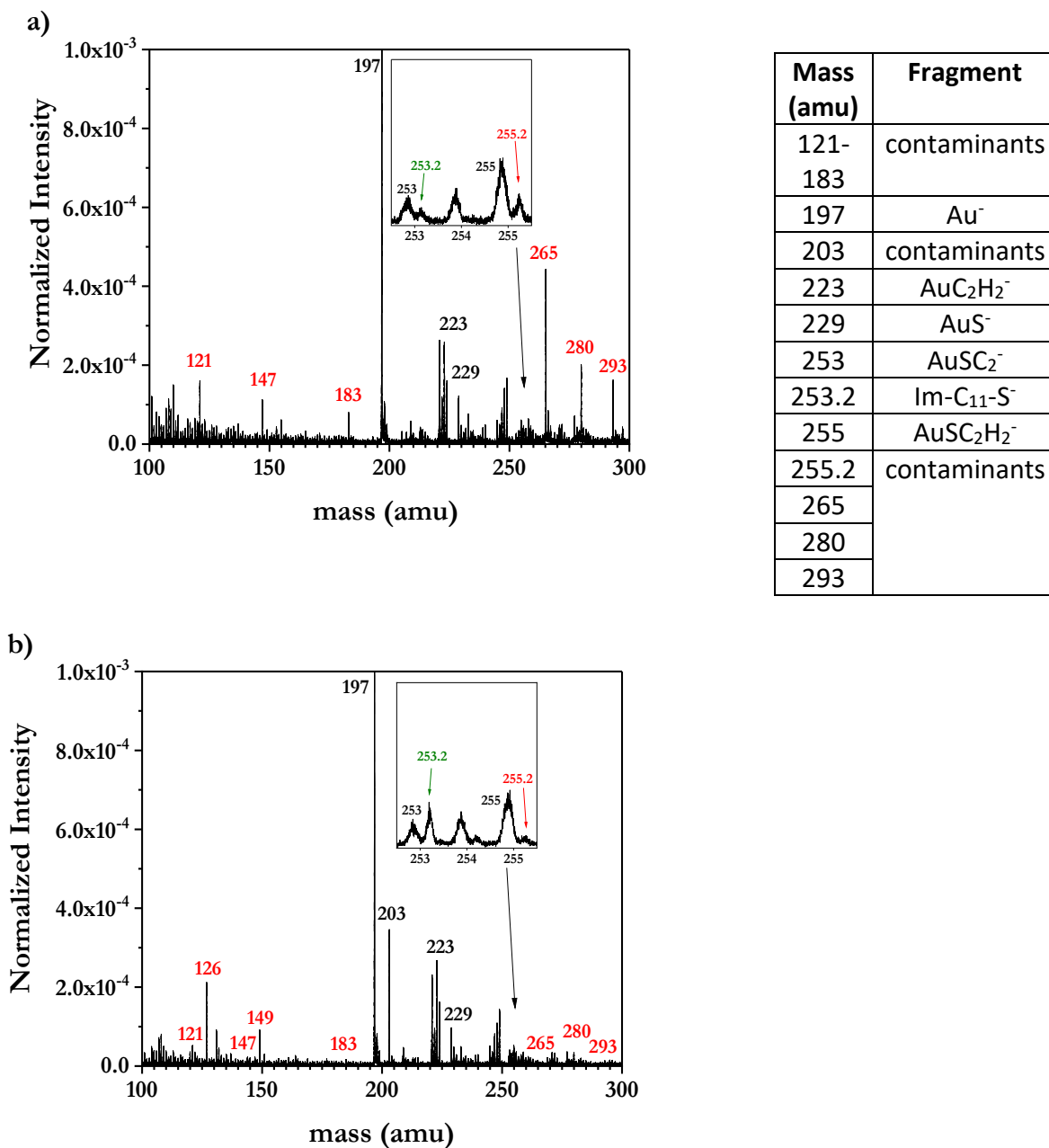
Figure 26. (a) Mass spectrum of non-precleaned Au functionalized with $Im-C_{11}-SH$ SAMs deposited from a 1.6 mM ethanolic thiol solution during the first deposition. (b) Mass spectrum of precleaned Au functionalized with $Im-C_{11}-SH$ SAMs deposited from a 5 mM ethanolic thiol solution during the second deposition. Mass range of 100-300 amu.
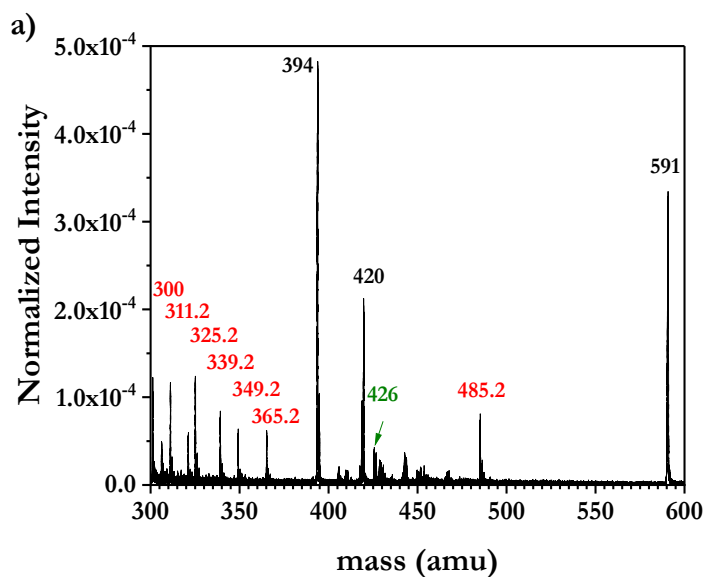
Mass (amu)	Fragment
300-365.2	contaminants
394	Au_2^-
420	$Au_2C_2H_2^-$
426	Au_2S^-
485.25, 520.5	contaminants
591	Au_3^-
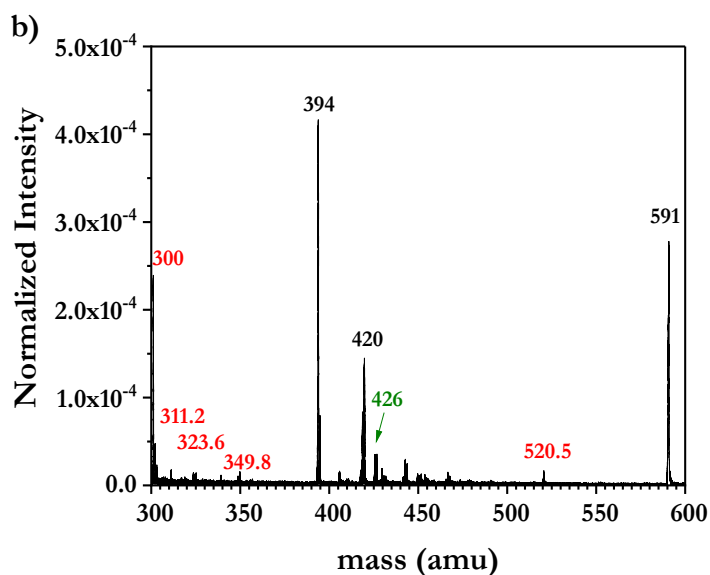
Figure 27. (a) Mass spectrum of non-precleaned Au functionalized with Im-C$_{11}$-SH SAMs deposited from a 1.6 mM ethanolic thiol solution during the first deposition. (b) Mass spectrum of precleaned Au functionalized with Im-C$_{11}$-SH SAMs deposited from a 5 mM ethanolic thiol solution during the second deposition. Mass range of 300-600 amu.

Mass (amu)	Fragment
603	Au_3C^-
615	$Au_3C_2^-$
623	Au_3S^-
639	$Au_3C_4^-$
703	$Au(Im\text{-}C_{11}\text{-}S^-)_2$
788	Au_4^-
800	Au_4C^-
813	$Au_4C_2H^-$
820	Au_4S^-
985	Au_5^-
1017	Au_5S^-
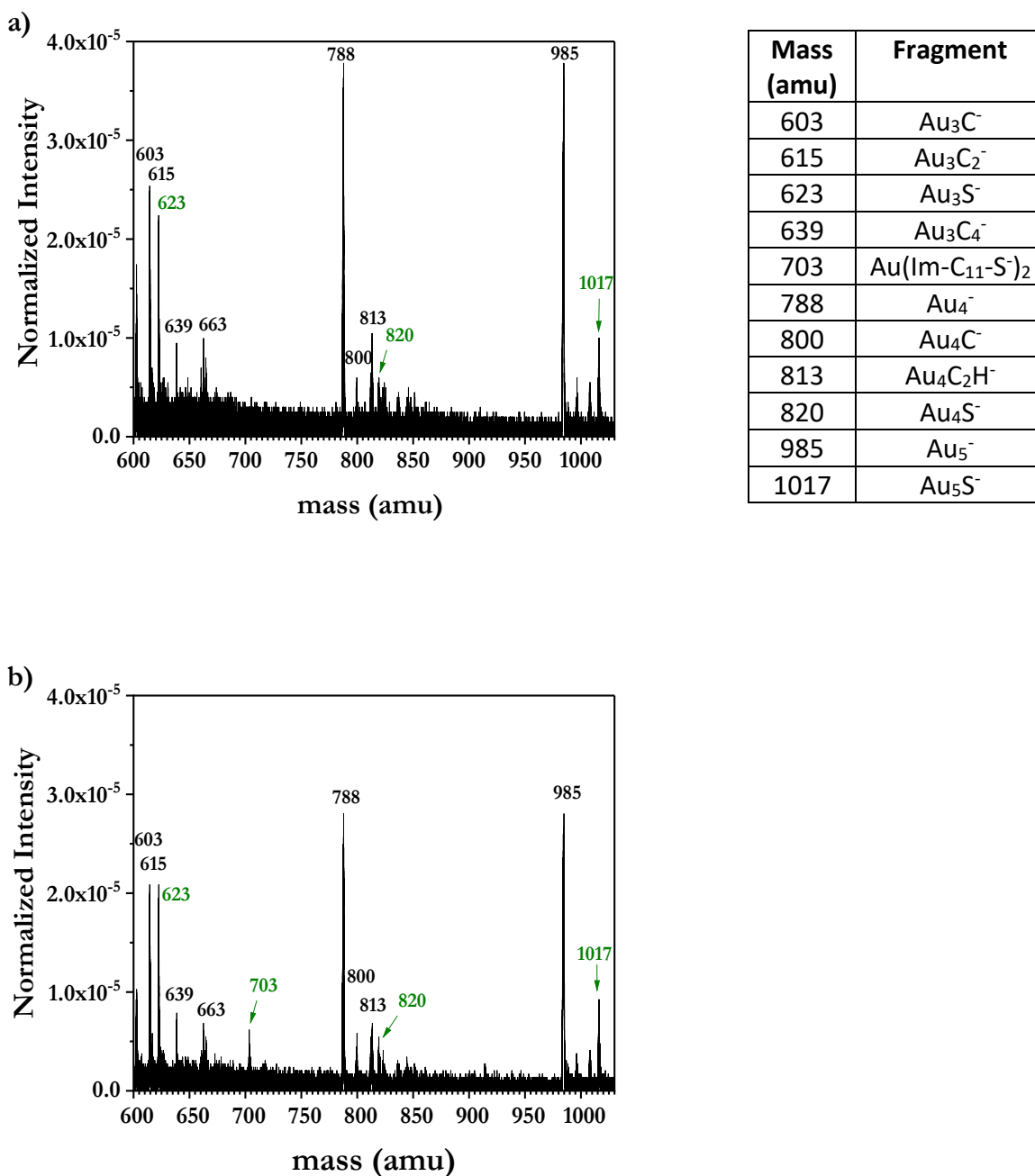
Figure 28. (a) Mass spectrum of non-precleaned Au functionalized with Im-C_{11}-SH SAMs deposited from a 1.6 mM ethanolic thiol solution during the first deposition. (b) Mass spectrum of precleaned Au functionalized with Im-C_{11}-SH SAMs deposited from a 5 mM ethanolic thiol solution during the second deposition. Mass range of 600-1030 amu.

One needs to pay attention to the zoomed-in region of 252.5-255.5 amu in Figure 26a,b. The important characteristic peak of an (Im-C_{11}-S^-) fragment at 253.2 amu corresponds to the

deprotonated molecule of Im-C_{11}-SH which implies that the adsorption process occurred on the surface of gold [51].

It must be noted that for the substrate shown in Figure 26a, the concentration of an Im-C_{11}-SH solution was 1.6 mM, whereas, in Figure 26b, it was increased to 5 mM. As a result, the intensity of the (Im-C_{11}-S^-) peak increased with an increase in the thiol concentration. This is one of the pieces of evidence that the coverage increased.

Also, in Figure 26a, the surface of Au was not precleaned using the liquid-UVPO treatment before the SAMs deposition. The positive impact of this treatment can be observed by comparing spectra in Figure 26a,b at the mass ranges 121-183 amu, 255.2 amu and above. All peaks in these regions correspond to contaminants in the form of adventitious organic compounds adsorbed on the surface of Au either during the manufacturing of the Au-coated Si chips or during their handling under ambient laboratory conditions. Such compounds are composed of polymeric hydrocarbon species, $(C_xH_y)_n$, or oxidized carbon species, C_mO_p, containing C–O–C, O=C–O, O=C=O, and C–OH groups [125, 126]. In Figure 26b their peak intensities are negligible compared to those in Figure 26a. The same trend can be observed in the spectra of higher mass regions in Figure 27a,b. The intensities of the peaks at 311.2-365.2 amu and 485.2 amu decrease significantly after the liquid-UVPO treatment was used. This technique was selected for all further experiments due to its efficacy, and its promising preservation of surface morphology as well as crystallinity of Au [103].

To measure the coverage (K) of Au-coated Si chips with Im-C_{11}-SH SAMs, the Surface Analysis and Mapping of Projectile Impacts (SAMPI©) software (version 5.0.5) was employed [92, 95]. A characteristic pair of Au-S cluster ions, namely Au_2S^- (426 amu) and Au_3S^- (623 amu), was selected to perform calculations. The SAMPI© software enables the extraction of the total

number of detected ions per impact (Y_{tot}, the total yield) from a total spectrum, and the number of detected ions per impact when detecting a specific ion (Y_{coinc}, the coincidence yield) from a coincidence spectrum. In general, a coincidence spectrum is composed of events containing a selected ion of interest. It shows all ions co-emitted with the selected ion from the same desorption volume [94, 95, 127-130]. In the present case, impacts of the detected Au_3S^- ions were selected to obtain a coincidence spectrum, after which the total yield of the co-emitted Au_2S^- ion, Y_{tot} (Au_2S^-), was divided by the coincidence yield of Au_2S^- ion, Y_{coinc} (Au_2S^-). The corresponding peaks are shown in Figure 27a, 28a. To sum up, K was measured utilizing the following equation:

$$K = \frac{Y_{tot} \ (Au_2S^-)}{Y_{coinc} \ (Au_2S^-)} \cdot 100\%$$

Eq. 5

K was measured to be $(78 \pm 7)\%$ when the SAMs deposition was performed from a 1.6 mM Im-C_{11}-SH solution for the first time.

To increase the K value, the concentration of ethanolic Im-C_{11}-SH solution was increased to 5 mM during the second deposition. Impacts of the detected Au_3S^- (623 amu), $Au(Im-C_{11}-S^-)_2$ (703 amu, and 704 amu due to the presence of ^{13}C), Au_4S^- (820 amu), and Au_5S^- (1017 amu) ions were selected to obtain a sum coincidence spectrum. The corresponding peaks are depicted in Figure 28b. In general, a sum coincidence spectrum is composed of events containing either of the selected ions of interest. Such selection enhances the accuracy of co-localized species identification on complex surfaces [94, 95]. To measure K, the total yield of Au_2S^- ion was divided by the coincidence yield of Au_2S^- ion utilizing Eq. 5. The corresponding peak is shown in Figure 27b. The K value was increased to $(99 \pm 6)\%$.

Moreover, the appearance of another characteristic peak of a dimer $Au(Im-C_{11}-S^-)_2$ at 703 amu in Figure 28b confirms that the coverage increased for the sample with the higher thiol

concentration. The reason is that this peak corresponds to the fragment where two deprotonated molecules of Im-C$_{11}$-SH are attached to the same gold center.

Additionally, one more confirmation that the coverage increased is we observed a decrease in the peak intensities corresponding to the substrate signal Au$^-$, and gold cluster ions Au$_x^-$ shown in Figure 26b-28b. If there is a monolayer of thiol molecules present on the gold surface, it is harder for projectiles to bombard the gold surface deeply. Consequently, part of the projectiles' energy is lost for the SAMs fragmentation. This results in decreasing the peak intensities of Au$^-$ (197 amu), Au$_2^-$ (394 amu), Au$_3^-$ (591 amu), Au$_4^-$ (788 amu), Au$_5^-$ (985 amu) ions.

The main conclusions of NP-SIMS are: 1) a chip needs to be precleaned using the liquid-UVPO treatment before the SAMs deposition from a 5 mM ethanolic thiol solution; 2) The highest value of the coverage was obtained in the order of (99 $\pm$ 6)% after the second SAMs deposition which indicates that surface is covered with Im-C$_{11}$-SH SAMs quantitatively. To sum up, to obtain the highest coverage, one cycle of SAMs deposition-regeneration is recommended before the final second deposition.

3.1.3   The study of the Im-C$_{11}$-SH, MDDA SAMs chemical state and the kinetics of their degradation

The chemical state of Im-C$_{11}$-SH SAMs deposited from a 5 mM ethanolic thiol solution once was characterized by XPS. Figure 29,30 show the XPS spectra of the S 2p and N 1s regions of the SAMs. Table 8 summarizes peak areas as well as the elemental composition of SAMs.
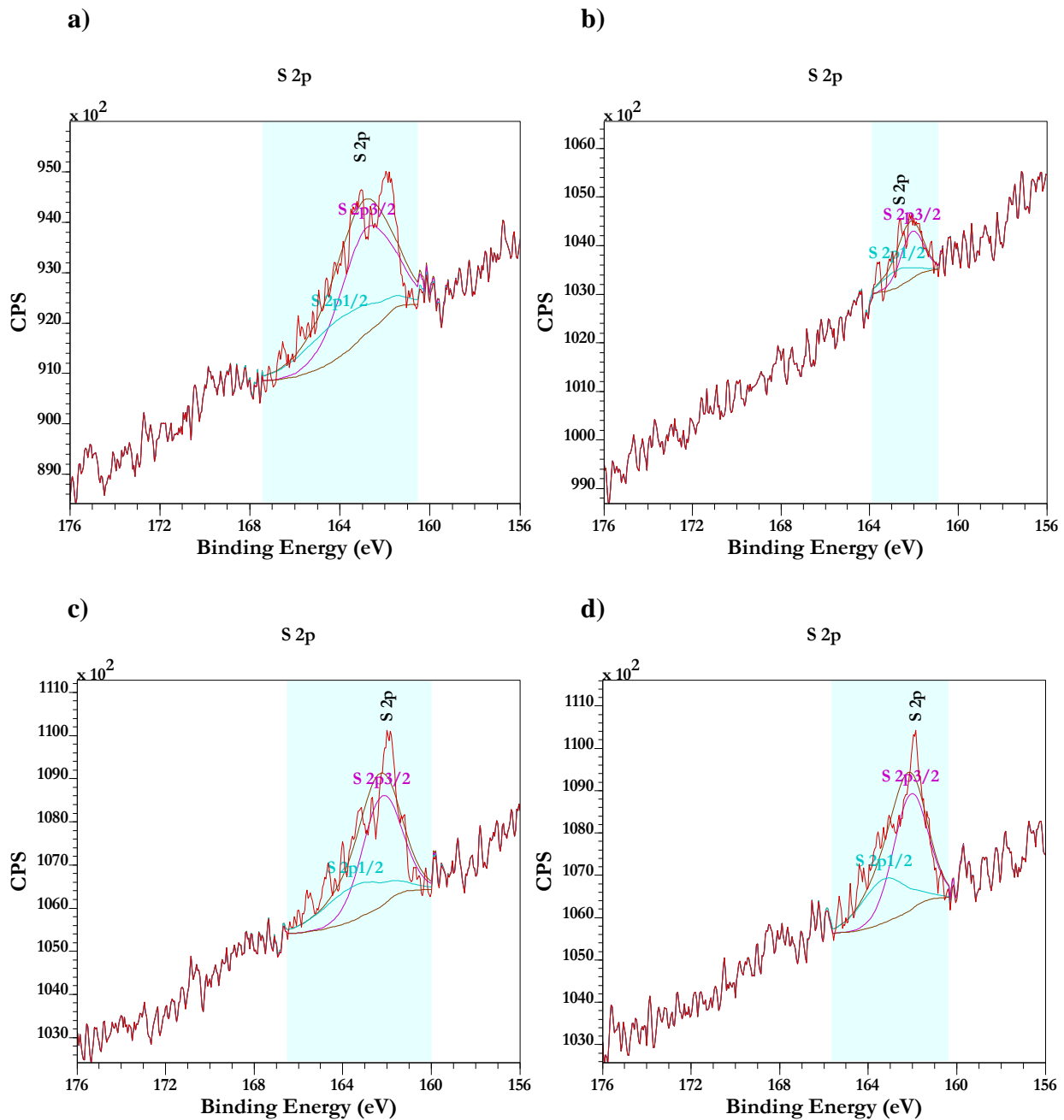
Figure 29. Sulfur 2p XPS for Im-C$_{11}$-SH SAMs on precleaned Au; one SAMs deposition: (a) the freshly prepared SAMs; (b) SAMs removed using the liquid-UVPO treatment; (c) the freshly prepared sample stored for two weeks; (d) the freshly prepared sample stored for one month.
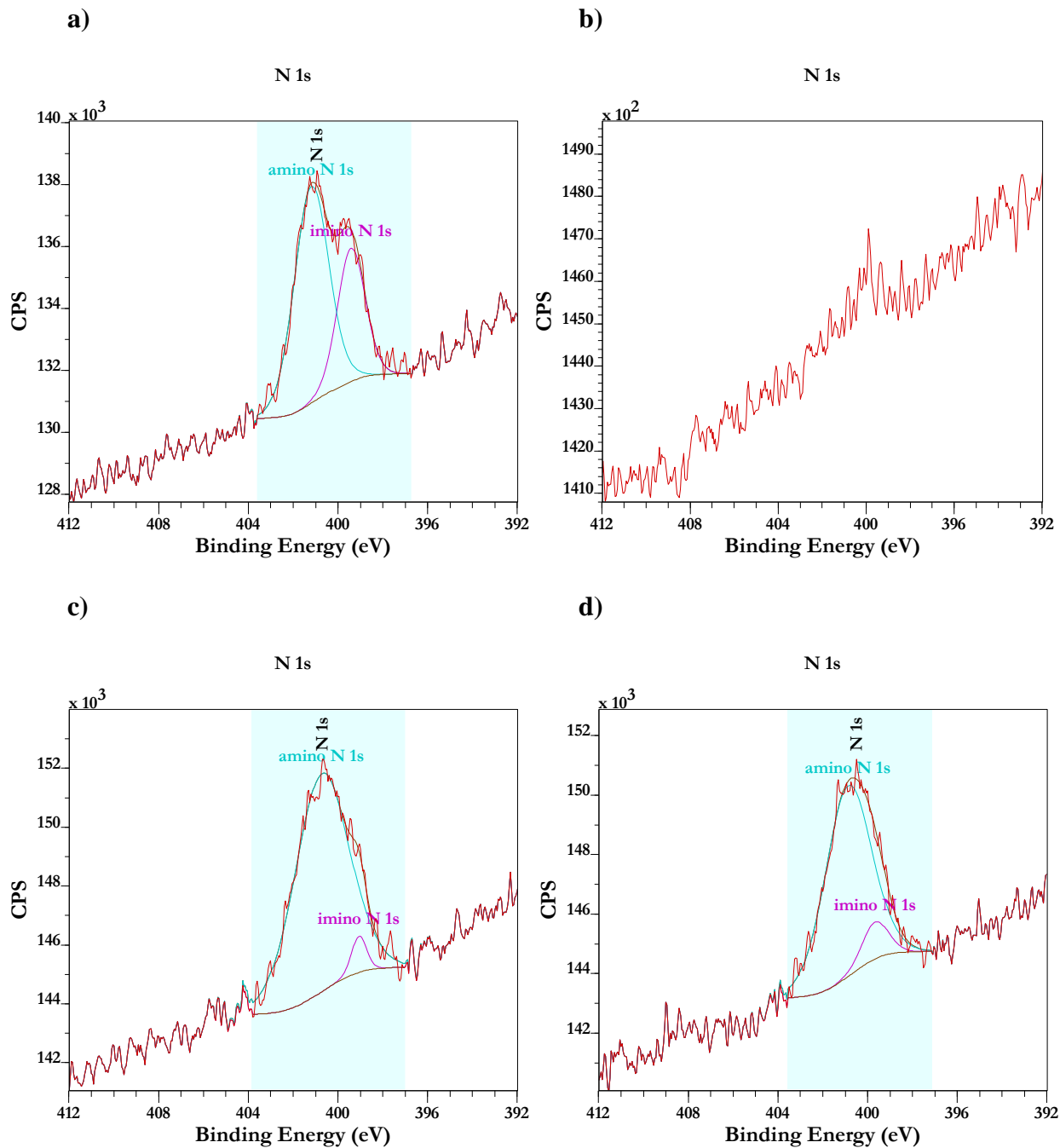
Figure 30. Nitrogen 1s XPS for Im-C_{11}-SH SAMs on precleaned Au; one SAMs deposition: (a) the freshly prepared SAMs; (b) SAMs removed using the liquid-UVPO treatment; (c) the freshly prepared sample stored for two weeks; (d) the freshly prepared sample stored for one month.

Table 8. Peak areas in the XPS spectra, and composition of Im-C₁₁-SH SAMs.

Sample	Au 4f, CPS.eV	C 1s, CPS.eV	N 1s, CPS.eV	O 1s, CPS.eV	S 2p, CPS.eV	Au 4f, %	C 1s, %	N 1s, %	O 1s, %	S 2p, %	Desorbed SAMs, %
Freshly deposited	1621.82	2474.20	295.92	334.40	131.24	33.39	50.93	6.09	6.88	2.70	0
2 weeks storage	1802.662	2772.53	333.30	378.65	127.14	33.29	51.21	6.16	6.99	2.35	3
1 month storage	1854.864	2794.45	263.08	411.92	119.05	34.08	51.34	4.83	7.57	2.19	9
After SAMs removal	2979.337	1312.58	-	268.91	26.76	64.94	28.61	-	5.86	0.58	80

Sulfur XPS spectra shown in Figure 29 contain spin-orbit splitting components with S $2p_{3/2}$ at around 162.5 eV which corresponds to a thiolate bound to the gold surface, while S $2p_{1/2}$ at 163.0-164.0 eV indicates some unbound sulfur species produced due to the damage of SAMs caused by the ionizing radiation (X-rays during XPS measurements, or UV-light during the liquid-UVPO treatment) [81, 99, 131, 132].

Nitrogen XPS spectra are presented in Figure 30 for the same series of samples. They contain two components in N 1s peaks at 399.42 and 401.19 eV, which are assigned to imino and amino N of the imidazole ring in the Im-C₁₁-SH molecule (see Figure 1a in Section 2.3.1.2) [81, 133, 134].

As can be seen in Figure 29b,30b and Table 8, the peaks of S 2p and N 1s vanished after the H₂O₂-mediated liquid UV-light photooxidation treatment that was employed to remove thiolate SAMs. Additionally, increases in the Au 4f peak area shown in Table 8 and the Au 4f peak intensity (see Figure A1a,b in the appendix) further support this idea. So, when SAMs are removed, the gold photoelectrons are no longer attenuated which rises the intensity of Au 4f peaks [99]. The percentages of S 2p, C 1s, and N 1s peaks decrease drastically after Im-C₁₁-SH SAMs are removed

as seen in Table 8. The S 2p, C 1s, and N 1s peak intensities and areas are related to the amount of Im-C_{11}-SH SAMs present on the gold surface. Decreases in the intensities, the peak areas, and the composition percentage explain Im-C_{11}-SH SAMs desorption [99]. Carbon and oxygen XPS spectra are illustrated in Figure A1 in the appendix. The S 2p peak area of the freshly prepared Im-C_{11}-SH SAMs was assumed to be 100%. Then, solving the proportion showed that 80% of SAMs were desorbed from the gold surface. This all suggests that the gold-coated silicon chips can be reused.

The process that stands behind the removal of SAMs from the gold surface is the following. After the UV light interacts with H_2O_2, hydroxyl radicals (HO$^\bullet$) are formed. Then, thiolate species are oxidized to sulfonates that loosely bind to metal surfaces and can be easily washed away with ethanol [103]:

$$\tfrac{1}{2}\,H_2O_2 + h\nu \rightarrow HO^\bullet \qquad\qquad \text{Eq. 6}$$

$$RS-Au + O_2 + HO^\bullet \rightarrow RSO_3H + Au, \qquad\qquad \text{Eq. 7}$$
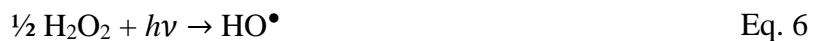
where R is the organic radical. Several pathways of imidazole atmospheric oxidation initiated by hydroxyl radicals can be found in the study conducted by Safaei *et al.* [135].

Furthermore, the effect of sample aging was studied. The XPS results indicate that prepared SAMs do not degrade significantly when stored under ambient conditions, except that samples were stored in wafer carrier trays and wrapped with aluminum foil to avoid exposure to air and light. These are known to be the main factors in the SAMs degradation [99]. The decrease in the S 2p peak areas allows us to evaluate the kinetics of the Im-C_{11}-SH SAMs degradation. Therefore, 3% and 9% of SAMs were lost after two weeks and one month of storage, respectively. Additionally, a shoulder that corresponds to the imino N component becomes less pronounced after the sample storage which is presented in Figure 30c,d. This can be attributed to the

transformations inside the imidazole ring due to atmospheric oxidation which was previously reported by Safaei *et al.* [135]. On the other hand, the Au 4f peak areas listed in Table 8 and the Au 4f peak intensities (see Figure A1 in the appendix) increase during the sample storage which also means that a lower amount of the thiolate molecules is present on the gold surface. At the same time, Table 8 shows that the C 1s peak areas increase slightly. This might be attributed to the contamination of the gold surfaces with organic compounds detached from the walls of the wafer carrier trays. Table 8 also reveals the same trend for the elemental composition of SAMs. Degradation of thiolate SAMs under ambient conditions leads to the formation of either disulfides (Eq. 8) or sulfonates (Eq. 9) which can be easily washed away from the gold surface with ethanol [51, 136, 137]:

$$2\ RS-Au \rightarrow RSSR + 2\ Au \qquad\qquad\qquad \text{Eq. 8}$$

$$RS-Au + H_2O + O_3 \rightarrow RSO_3H + HO-Au \qquad\qquad\qquad \text{Eq. 9}$$

Even though such oxidation factors as air and light were limited, even a small amount of moisture present in closed wafer-carrier trays could lead to the beginning of the SAMs partial degradation processes.

Similarly, the chemical state of MDDA SAMs deposited from a 5 mM ethanolic thiol solution once was characterized by XPS. Sulfur XPS spectra shown in Figure 31 contain S $2p_{3/2}$ and S $2p_{1/2}$ spin-orbit split components. Carbon XPS spectra contain the C-C, C-H component at 284.8 eV due to the presence of a hydrocarbon chain, the C-O-C component at 286 eV, and the O-C=O component at 288.5 eV as depicted in Figure 32 [132], [138]. The last two components are attributed to the presence of the carboxyl functional group in the MDDA structure (see Figure 1b in Section 2.3.1.2). Table 9 summarizes Au 4f, C 1s, O 1s, S 2p peak areas as well as the elemental composition of SAMs. Gold and oxygen XPS spectra are illustrated in the appendix.
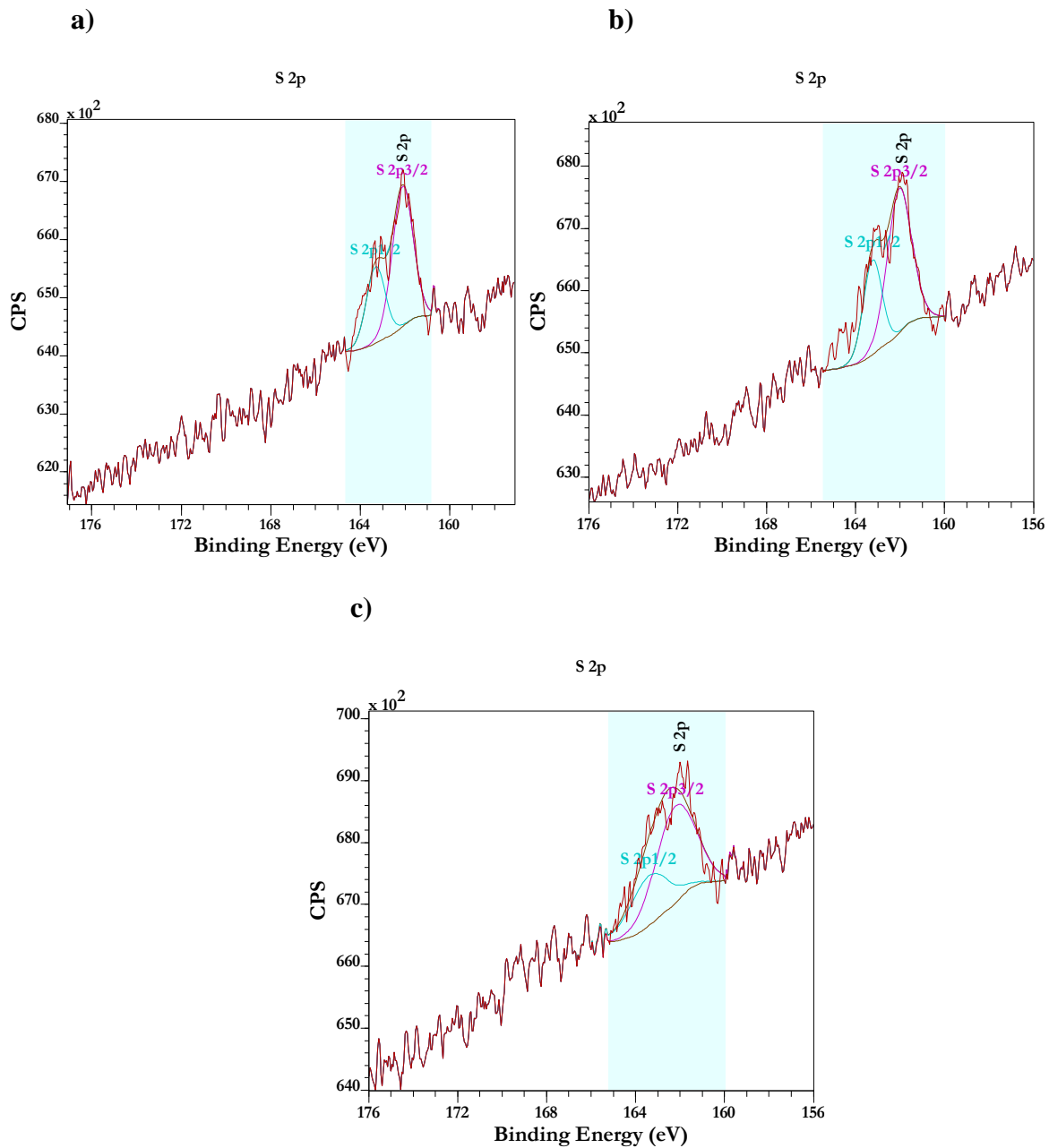
Figure 31. Sulfur 2p XPS for MDDA SAMs on precleaned Au; one SAMs deposition: (a) the freshly prepared SAMs; (b) the freshly prepared sample stored for one week; (c) the freshly prepared sample stored for one month.
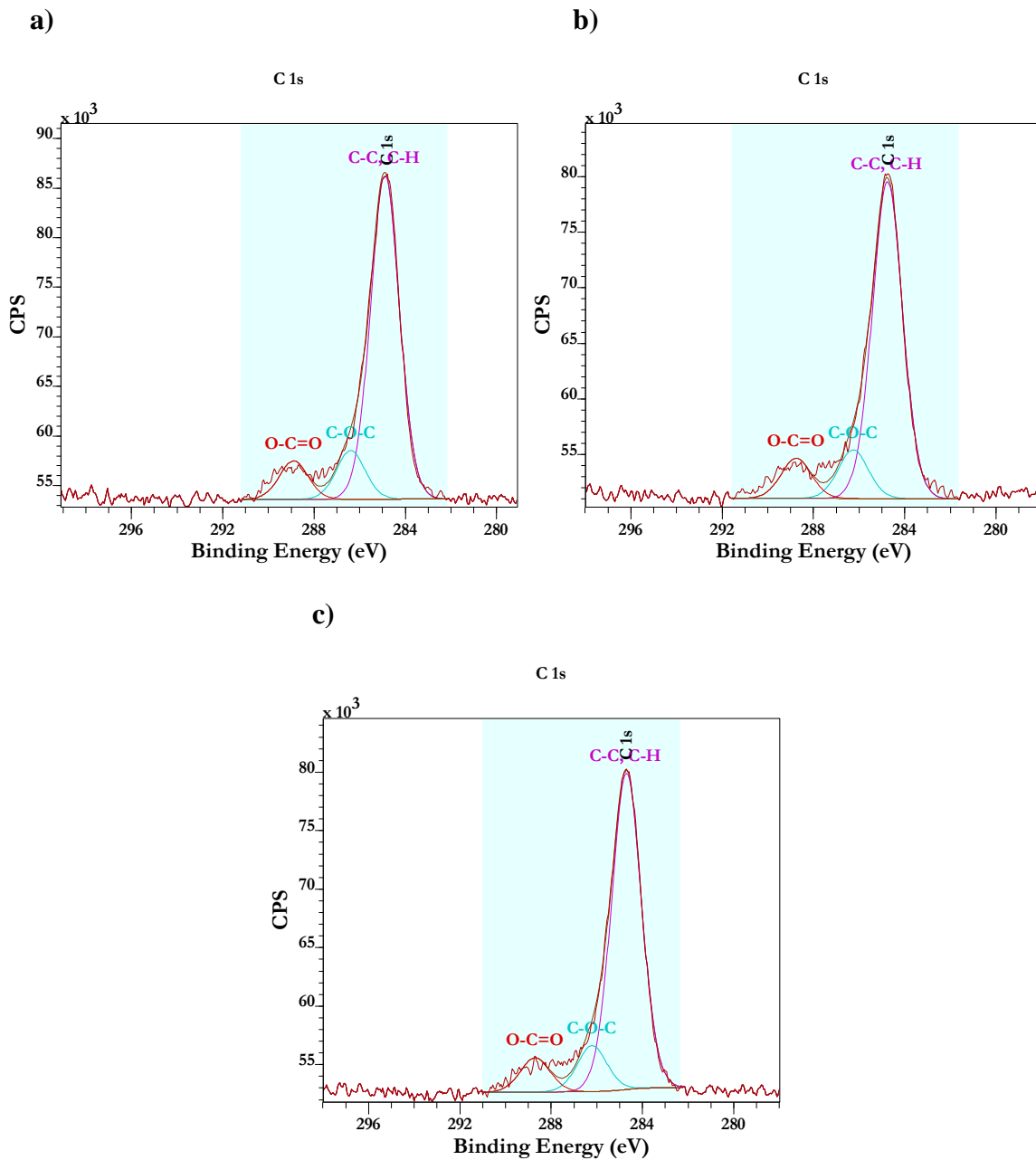
Figure 32. Carbon 1s XPS for MDDA SAMs on precleaned Au; one SAMs deposition: (a) the freshly prepared SAMs; (b) the freshly prepared sample stored for one week; (c) the freshly prepared sample stored for one month.

Table 9. Peak areas in the XPS spectra, and composition of MDDA SAMs.

Sample	Au 4f, CPSeV	C 1s, CPSeV	O 1s, CPSeV	S 2p, CPSeV	Au 4f, %	C 1s, %	O 1s, %	S 2p, %
Freshly deposited	1206.5	1692.3	309.0	61.6	36.90	51.76	9.45	1.89
1 week storage	1205.9	1595.8	257.2	76.3	38.46	50.90	8.20	2.43
1 month storage	1447.2	1429.9	216.7	74.7	45.67	45.13	6.84	2.36

Likewise, the effect of sample aging was studied under the same storage conditions as for Im-C_{11}-SH SAMs. Minor changes in the shape of the S 2p doublet peak shown in Figure 31 and the S 2p peak area listed in Table 9 as a function of the sample storage time indicate the non-significant degradation of MDDA SAMs. The Au 4f peak area also remained in the same range after one week of the sample storage as shown in Table 9. Slight increases in the Au 4f peak area and the Au 4f peak intensity (see Figure A2 in the appendix) after one month of the sample storage mean that some MDDA SAMs were desorbed from the surface of gold making the gold photoelectrons no longer attenuated [99]. The C 1s peak intensity presented in Figure 32 and the C 1s peak area listed in Table 9 decrease slightly after one month of the sample storage also supporting the idea of the insignificant MDDA SAMs degradation.

3.1.4   Measurement of the thickness of Im-C$_{11}$-SH SAMs

Ellipsometry is an optical spectroscopy technique that was used to determine the thickness of Im-C$_{11}$-SH SAMs deposited from a 5 mM ethanolic thiol solution once. SAMs are very thin organic layers that are ideally composed of a single monolayer [139]. In general, their thickness is in the order of 1-2 nm and not more than 10 nm [100, 101, 134, 139].

Ellipsometry is sensitive to the presence of thin SAMs on the surface of gold due to the change in the measured delta (Δ) parameter, which contains information about the phase difference between p- and s-polarized light [140]. The measured (square symbols) and modeled (solid curves) Δ values versus the wavelength (λ) are plotted in full scale in Figure 33a. In the zoomed-in region of low delta values represented in Figure 33b, the change between samples can be observed.

During ellipsometry measurements, it is important to measure a bare gold surface to determine optical constants at first. The obtained data shown as green square symbols in Figure 33 was fitted using a B-Spline layer. As a result, the modeled green solid curve in Figure 33 represents the bare precleaned gold surface.

After this step, the thickness of the thin organic layer (Im-C$_{11}$-SH SAMs in our case) can be measured. The blue square symbols in Figure 33b represent Im-C$_{11}$-SH SAMs on the precleaned gold surface. One can notice a vertical shift in Δ toward lower values which is attributed to the presence of a thin film on top of gold. In the case of thicker films on the gold surface, a larger shift is observed. By fitting the data using the Cauchy layer, the blue solid curve was obtained, and the thickness of 1.690 ± 0.014 nm was reported for the freshly deposited Im-C$_{11}$-SH SAMs.

The thickness of Im-C$_{11}$-SH SAMs on the precleaned gold surface was also measured after one week of sample storage represented by the red square symbols in Figure 33b. The red solid curve was obtained after fitting the data, and the thickness of 1.640 ± 0.011 nm was measured.

The thickness value is slightly lower than that for the freshly deposited SAMs, but the difference in values is practically non-significant. Figure 33b also demonstrates the proximity of the fits for the freshly deposited and one-week-old SAMs.
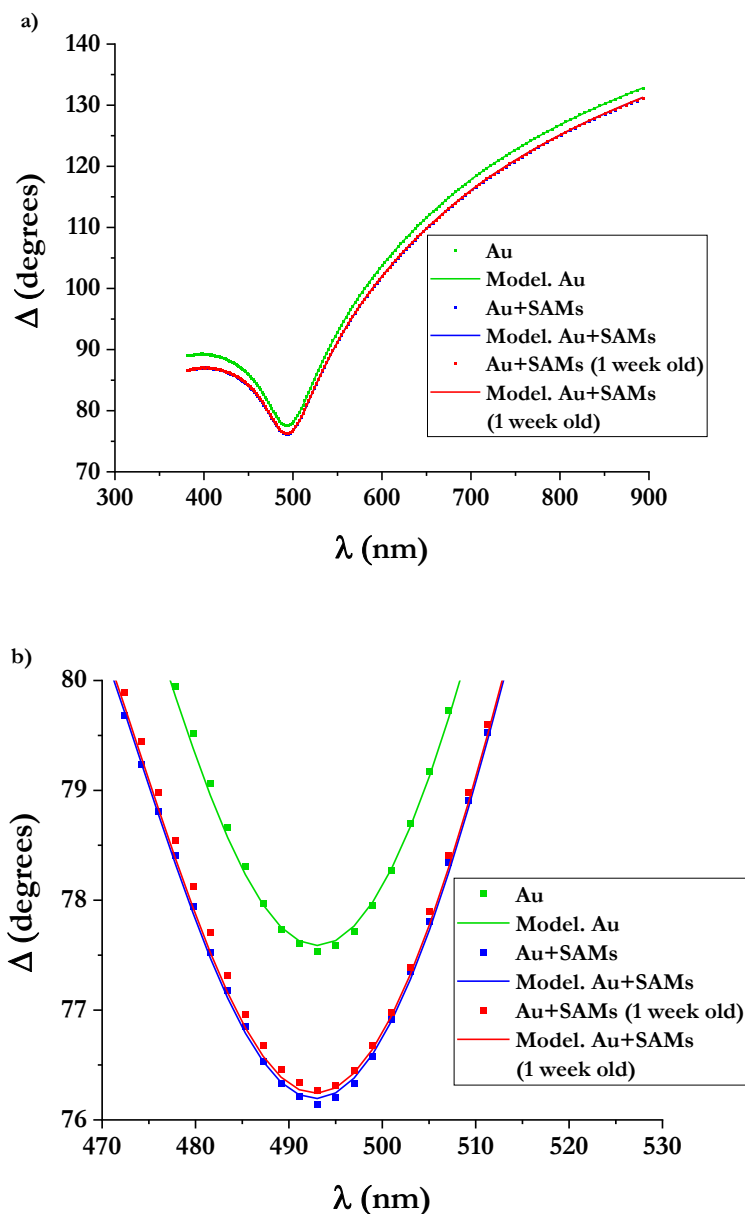
Figure 33. Delta as a function of wavelength: a) full scale; b) zoomed-in region of low delta values. Measured (square symbols) and modeled (solid curves) data for bare precleaned gold (green), freshly deposited Im-C_{11}-SH SAMs on precleaned Au (blue), Im-C_{11}-SH SAMs on precleaned Au after one week of storage (red). The B-spline layer was used to fit the bare precleaned gold data, n=1.50. The Cauchy layer was used to fit the Im-C_{11}-SH SAMs data, n=1.450.

As a result, ellipsometry showed that storing Im-C$_{11}$-SH SAMs for one week did not initiate degradation processes which would lead to a decrease in the SAMs thickness.

The measured thickness values indicate the presence of a single monolayer on the surface of gold and are in good agreement with the literature results obtained for similar films [100, 101, 134].

3.2   Ir(IV) and Rh(III) sorption on gold-coated chips

In the following section, the results of the NP-SIMS and the INAA analyses utilized to study the sorption of Ir(IV) and Rh(III) from 0.55 M HCl solutions on non-functionalized and functionalized gold-coated chips are discussed.

3.2.1   Measurement of the coverage of non-functionalized and functionalized gold-coated
         chips with Ir(IV) and Rh(III)

During the NP-SIMS analysis, the metal sorption from 5.2 µM Ir(IV), and 9.7 µM Rh(III) solutions in 0.55 M HCl, respectively, was performed on non-functionalized glass-coated chips and glass-coated chips functionalized with Im-C$_{11}$-SH SAMs deposited from a 5 mM ethanolic thiol solution. The substrates were submerged in Ir(IV) and Rh(III) solutions for approximately 21 h.

In the NP-SIMS analysis, a primary beam of 520 keV Au$_{400}^{4+}$ clusters bombards the surface of the functionalized chips, and the energy transfer from the beam to the surface causes the emission of cluster ions [93, 94]. Figure 34a-d display characteristic peaks of RhCl$_3^-$ (208-214 amu), RhCl$_4^-$ (243-251 amu), RhCl$_5^-$ (278-284 amu), Rh$_2$Cl$_7^-$ (451-459 amu),

Rh₃Cl₄H⁻ (450-458 amu) clusters which indicate the sorption of Rh(III) on functionalized gold-coated glass chips. $Rh_xCl_y^-$ introduce groups of peaks in the mass spectra due to the isotopes of Cl.

c)

d)
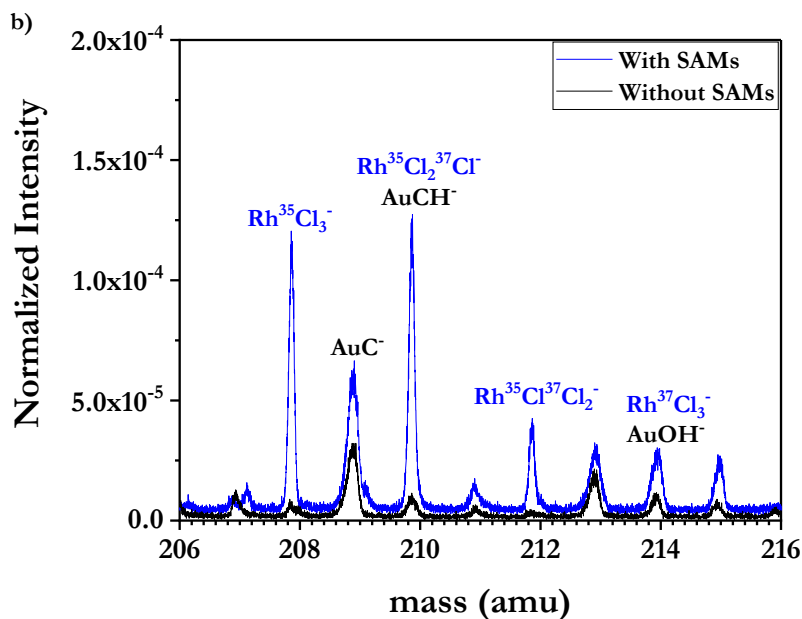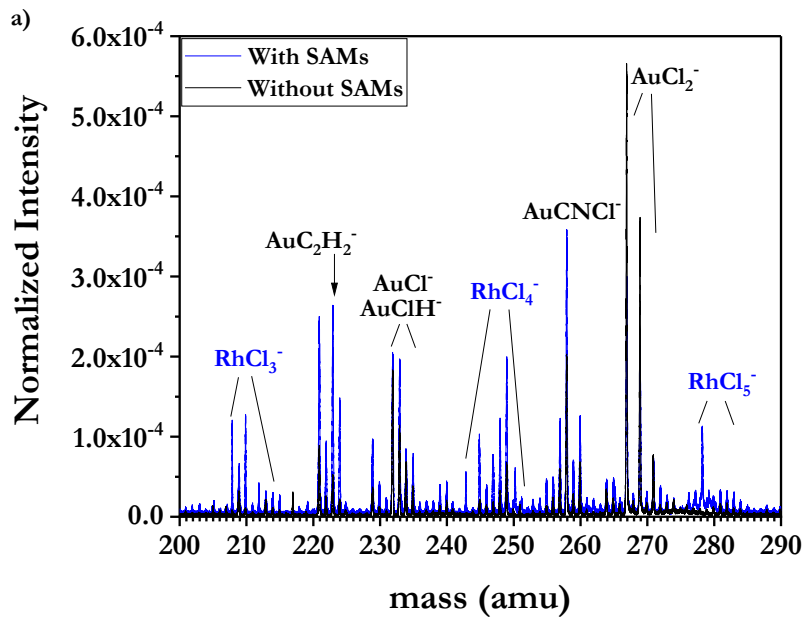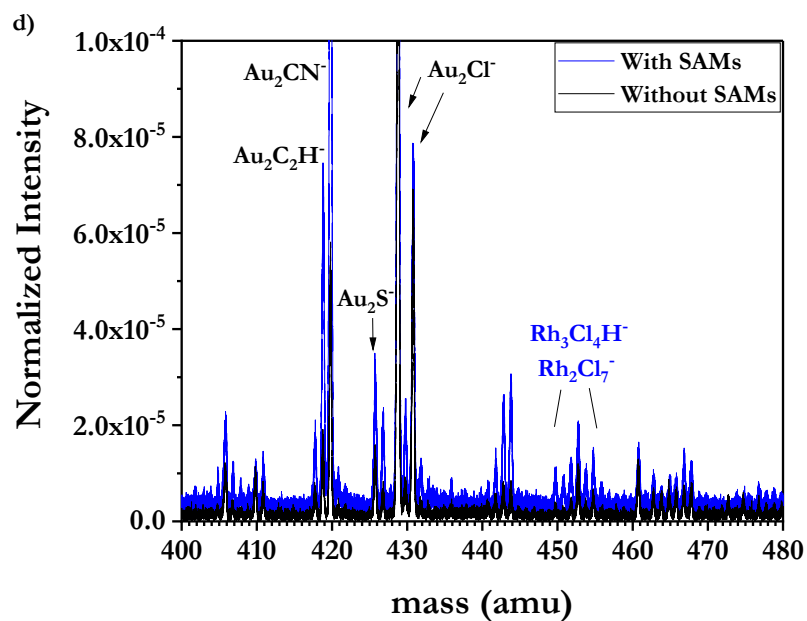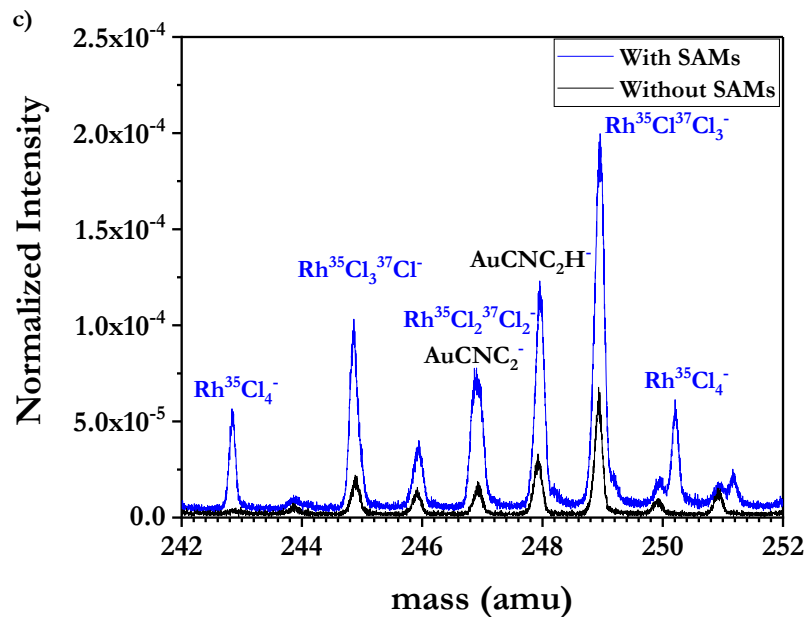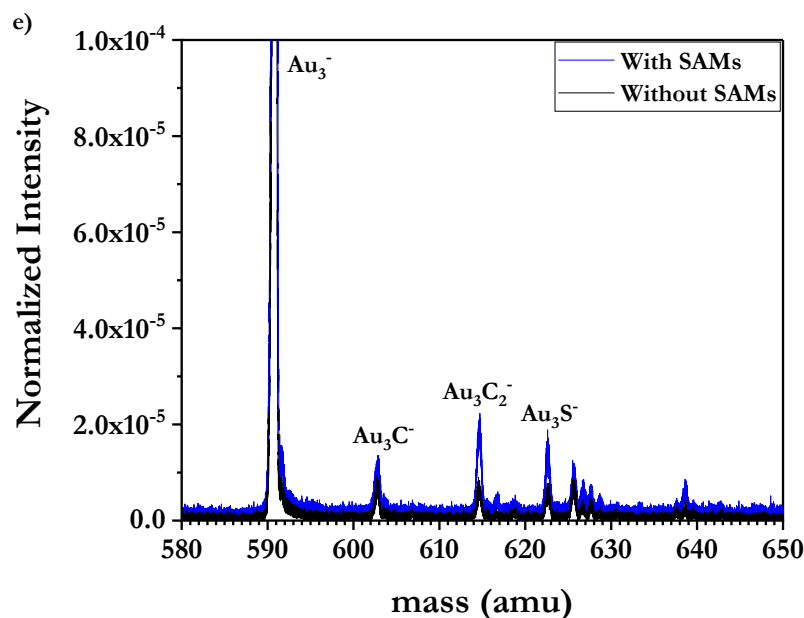
Figure 34. Mass spectra of precleaned Au functionalized with Im-C$_{11}$-SH SAMs and adsorbed Rh(III) (blue line), and precleaned non-functionalized Au with adsorbed Rh(III) (black line). [Rh]$_{init}$ = 9.7 μM, [HCl] = 0.55 M. (a) Mass range of 200 – 290 amu showing characteristic peaks of RhCl$_3^-$, RhCl$_4^-$ and RhCl$_5^-$ clusters. (b) Mass range of 206 – 216 amu showing zoomed-in ions of RhCl$_3^-$ clusters and their interference with other ions. (c) Mass range of 242 – 252 amu showing zoomed-in ions of RhCl$_4^-$ clusters and their interference with other ions. (d) Mass range of 400 – 480 amu showing characteristic peaks of Rh$_2$Cl$_7^-$ and Rh$_3$Cl$_4$H$^-$ clusters. (e) Mass range of 580 – 650 amu showing a characteristic peak of Au$_3$S$^-$ clusters important for the calculation of the coverage of Au with Im-C$_{11}$-SH SAMs.

In Figure 34b-d, one should notice that the intensities of the named clusters are much higher for samples where the Rh(III) sorption occurred on gold-coated glass chips functionalized with Im-C$_{11}$-SH SAMs compared to non-functionalized ones. For instance, the sum net yield for the peaks corresponding to RhCl$_3^-$ clusters (208-214 amu) observed on precleaned Au functionalized with Im-C$_{11}$-SH SAMs, and precleaned Au without Im-C$_{11}$-SH SAMs is $1.73 \cdot 10^{-2}$, and $1.85 \cdot 10^{-3}$, respectively. The net yield is the total yield with the background subtraction. The difference of one order of magnitude indicates more quantitative Rh(III) sorption on functionalized gold-coated glass chips rather than on non-functionalized ones.

RhCl$_3^-$ was chosen as a primary cluster to measure the coverage of Im-C$_{11}$-SH SAMs with Rh(III). The named cluster will give a more accurate result since its peaks are more narrow and have no significant interference compared to the RhCl$_4^-$ group of peaks which have more interference with other ions, such as AuCNC$_2^-$ (247 amu), AuCNC$_2$H$^-$ (248 amu) shown in Figure 34c. RhCl$_5^-$ and Rh$_2$Cl$_7^-$ clusters were not taken into consideration for the coverage calculation due to low statistics.

To measure K of Im-C$_{11}$-SH SAMs with Rh(III), a similar approach described above to measure K of Au-coated Si chips with Im-C$_{11}$-SH SAMs was used [94, 95, 127-130]. At first, impacts were selected where Rh^{35}Cl$_2^{37}$Cl$^-$ ion (210 amu) was detected to obtain a coincidence spectrum. After this, the total yield of co-emitted Rh^{35}Cl$_3^-$ ion (208 amu), Y_{tot} ($Rh^{35}Cl_3^-$), was divided by the coincidence yield of Rh^{35}Cl$_3^-$ ion, Y_{coinc} ($Rh^{35}Cl_3^-$):

$$K = \frac{Y_{tot}\ (Rh^{35}Cl_3^{\ -})}{Y_{coinc}\ (Rh^{35}Cl_3^{\ -})} \cdot 100\% \qquad \text{Eq. 10}$$

The results are represented in Table 10.

Table 10. Measured Ion Yields of RhCl$_3^-$ clusters used to measure the coverage of Im-C$_{11}$-SH SAMs on precleaned Au.

Type of Au substrate	Y_{tot} ($Rh^{35}Cl_3^-$)	Y_{coinc} ($Rh^{35}Cl_3^-$)	K (%)
With SAMs	0.008055	0.009912	81.3±3.8

There were not enough statistics to measure the coverage of non-functionalized Au with RhCl$_3$ clusters.

In the Rh(III) sorption experiments, the coverage of Au with Im-C$_{11}$-SH SAMs was measured according to Eq. 5 and gave a result of $(80 \pm 5)\%$. The SAMs deposition was performed once.

The presence of characteristic peaks of IrCl$_3^-$ (296-302 amu), IrCl$_4^-$ (331-339 amu), Ir$_2$Cl$_4^-$ (522-534 amu), Ir$_2$Cl$_5^-$ (557-571 amu), Ir$_2$Cl$_6^-$ (592-604 amu), Ir$_2$Cl$_7^-$ (627-643 amu), Ir$_3$Cl$_9^-$ (892-908 amu) and Ir$_3$Cl$_{10}^-$ (923-937 amu) cluster ions with high intensities confirms the sorption of Ir(IV) on functionalized gold-coated glass chips shown in Figure 35. Ir$_x$Cl$_y^-$ introduces groups of peaks in the mass spectra due to the stable isotopes of Ir and Cl, respectively.

78
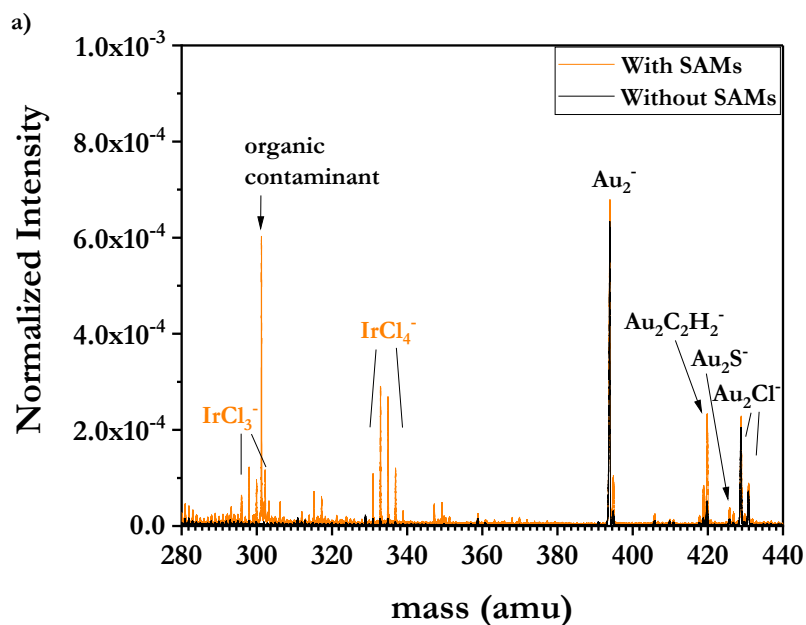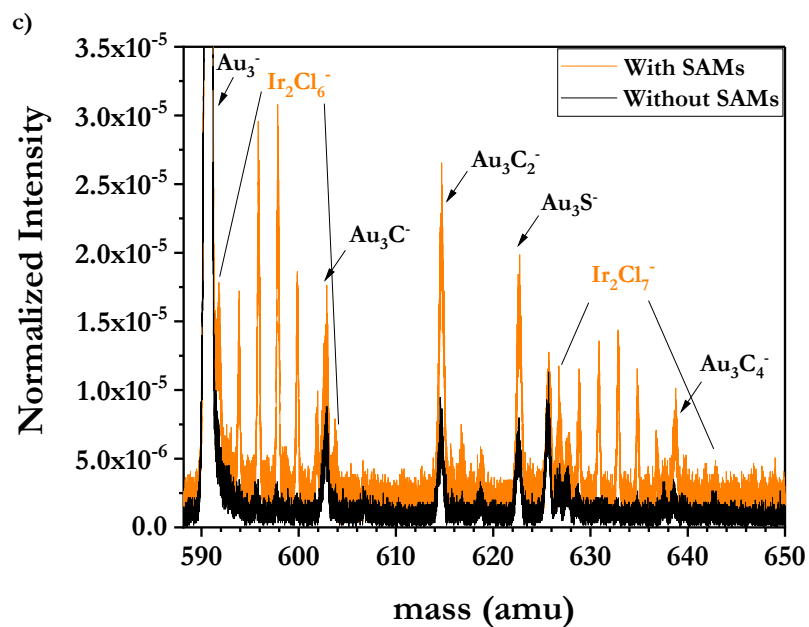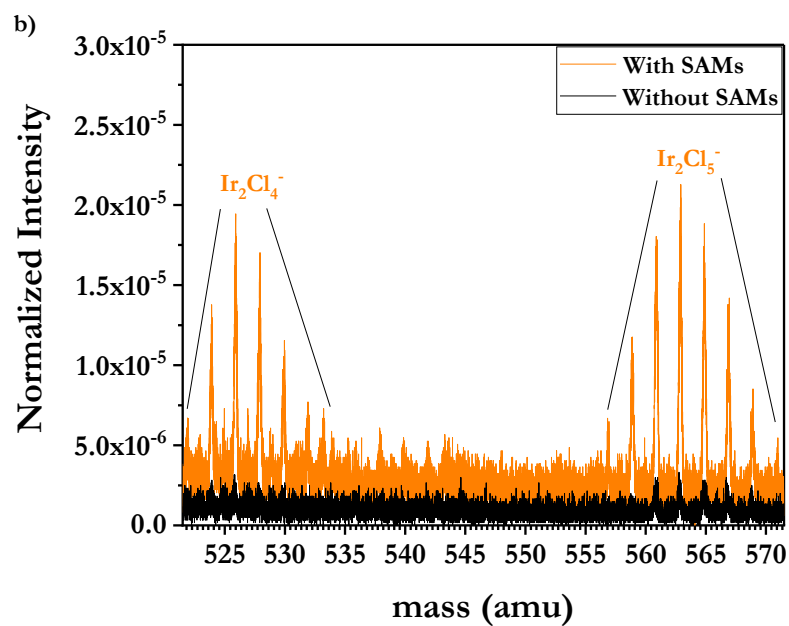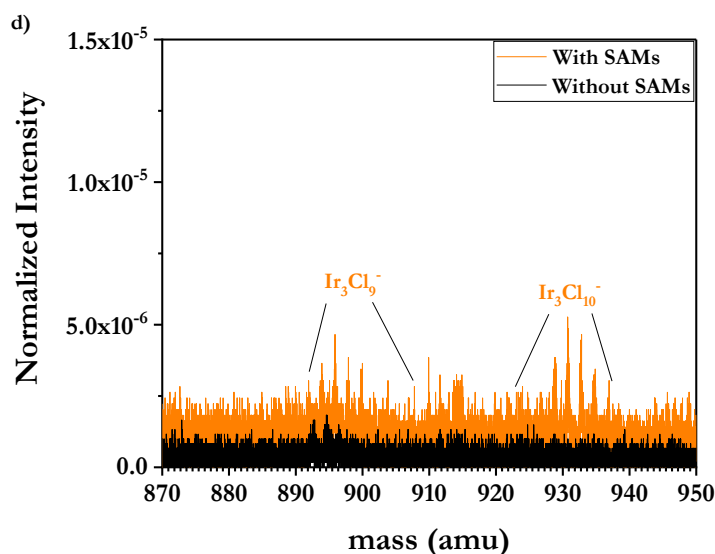
Figure 35. Mass spectra of precleaned Au functionalized with Im-C$_{11}$-SH SAMs and adsorbed Ir(IV) (orange line), and precleaned non-functionalized Au with adsorbed Ir(IV) (black line). [Ir]$_{init}$ = 5.2 μM, [HCl] = 0.55 M. (a) Mass range of 280-440 amu showing characteristic peaks of IrCl$_3^-$ and IrCl$_4^-$ clusters. (b) Mass range of 521.5 – 571.5 amu showing characteristic peaks of Ir$_2$Cl$_4^-$ and Ir$_2$Cl$_5^-$ clusters. (c) Mass range of 588 – 650 amu showing characteristic peaks of Ir$_2$Cl$_6^-$ and Ir$_2$Cl$_7^-$ clusters. (d) Mass range of 870 – 950 amu showing characteristic peaks of Ir$_3$Cl$_9^-$ and Ir$_3$Cl$_{10}^-$ clusters.

In Figure 35b-d, it can be noticed that the intensities of the named clusters turned out to be much higher for samples where the Ir(IV) sorption occurred on gold-coated glass chips functionalized with Im-C$_{11}$-SH SAMs compared to non-functionalized ones. For example, the sum net yield for the peaks corresponding to Ir$_2$Cl$_5^-$ clusters (557-571 amu) observed on precleaned Au functionalized with Im-C$_{11}$-SH SAMs, and precleaned Au without Im-C$_{11}$-SH SAMs is $5.41 \cdot 10^{-3}$, and $4.58 \cdot 10^{-4}$, respectively. The net yield is the total yield with the background subtraction. The difference of one order of magnitude indicates more quantitative Ir(IV) sorption on functionalized gold-coated glass chips rather than on non-functionalized ones.

Ir$_2$Cl$_6^-$ was chosen as a primary cluster to measure the coverage of Im-C$_{11}$-SH SAMs with Ir(IV). The named cluster will give a more accurate result since by itself it can form Ir$_2$Cl$_4^-$ and

$Ir_2Cl_5^-$ clusters during the fragmentation. Also, its intensity is much higher than that for $Ir_2Cl_7^-$ which is observed in Figure 35c. $IrCl_3^-$, $IrCl_4^-$, $Ir_3Cl_9^-$ and $Ir_3Cl_{10}^-$ clusters were not taken into consideration for the calculation of K due to low statistics.

At first, impacts, where $Ir_2Cl_4^-$ (522-534 amu) or $Ir_2Cl_5^-$ (557-571 amu) ions were detected, were selected to obtain a sum coincidence spectrum. As it was discussed earlier, such selection enhances the accuracy of co-localized species identification on complex surfaces [94, 95]. The peaks with the low mass intensity were not taken into consideration. After this, the total yield of co-emitted $Ir_2Cl_6^-$ ion (596 amu), $Y_{tot}(Ir_2Cl_6^-)$, was divided by the coincidence yield of $Ir_2Cl_6^-$ ion, $Y_{coinc}(Ir_2Cl_6^-)$:

$$K = \frac{Y_{tot}\ (Ir_2Cl_6^-)}{Y_{coinc}\ (Ir_2Cl_6^-)} \cdot 100\% \qquad \text{Eq. 11}$$

The results are represented in Table 11.

Table 11. Measured Ion Yields of $Ir_2Cl_6^-$ clusters used to measure the coverage of Im-C_{11}-SH SAMs on precleaned Au.

Type of Au substrate	$Y_{tot}(Ir_2Cl_6^-)$	$Y_{coinc}(Ir_2Cl_6^-)$	K (%)
With SAMs	0.002543	0.003852	66.0±3.4
Without SAMs	0.001932	0.004509	43±6

In the Ir(IV) sorption experiments, the coverage of Au with Im-C_{11}-SH was measured to be $(90 \pm 5)\%$ according to Eq. 5. The SAMs deposition was performed once.

3.2.2   Measurement of the surface saturation of non-functionalized and functionalized gold-coated chips with Ir(IV)

During the INAA analysis, the initial Ir(IV) concentration was varied in the range of 0.5 – 5.2 µM in 0.55 M HCl to study the surface saturation of gold-coated silicon or glass chips functionalized with Im-C_{11}-SH SAMs deposited from a 5 mM ethanolic thiol solution, and non-functionalized gold-coated chips. The substrates were submerged in Ir(IV) solutions for approximately 21 h.

A doubly charged complex $[IrCl_6]^{2-}$ is a predominant species in an aqueous solution [41, 42]. Therefore, its molar mass was used to measure the number of Ir(IV) molecules in the aqueous phase.

The surface saturation (SS) of Im-C_{11}-SH SAMs with Ir(IV) was measured using the following equation:

$$SS = \frac{N_{Ir \text{ init}} - N_{Ir \text{ eq}}}{A \cdot N_{\text{SAMs}}} \cdot 100\%,$$ Eq. 12

where $N_{Ir \text{ init}}$ is the initial number of Ir(IV) molecules in solution before sorption;

$N_{Ir \text{ eq}}$ is the number of Ir(IV) molecules in solution after sorption;

A is the area of a chip that is equal to 1 cm^2;

N_{SAMs} which equals $4.5 \cdot 10^{14}$ molecules/cm^2 is the typical surface density of molecules for alkanethiolate SAMs when the maximum coverage is obtained [52].

Figure 36 illustrates that the surface saturation of Im-C_{11}-SH SAMs with Ir(IV) increases with an increase of the initial Ir(IV) concentration. A possible reason is that there is no driving force for the sorption to occur on the surface when the initial Ir(IV) concentration is too low. Under such conditions, Ir(IV) is mostly complexing with hydrophilic Cl^- ions, and as a result, the Ir(IV) complex stays in solution. When the initial Ir(IV) concentration is high enough in the solution, the

concentration results in the Ir(IV) sorption on the substrate surface. The highest surface saturation of $(77 \pm 12)\%$ was obtained at 5.4 µM initial Ir(IV) concentration.
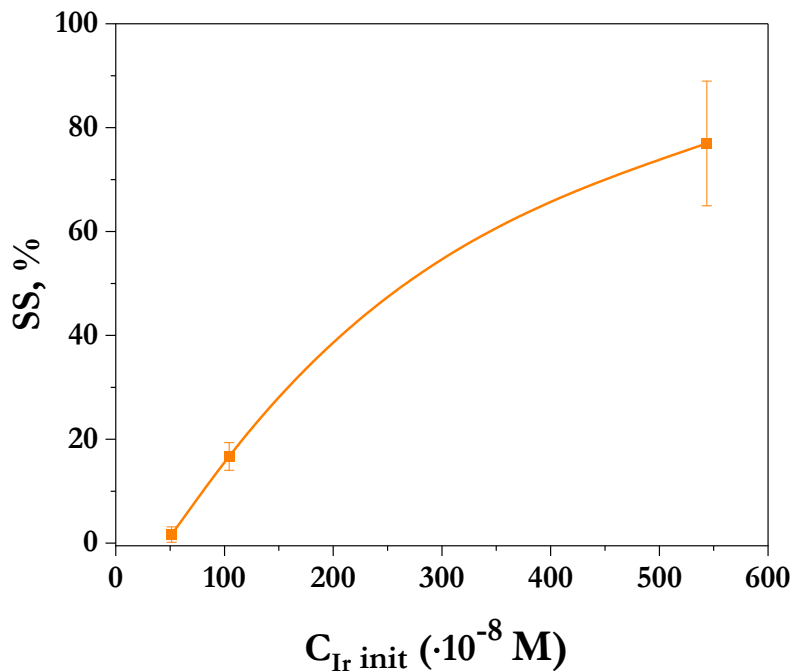
Figure 36. The surface saturation of Im-C$_{11}$-SH SAMs with Ir(IV) as a function of the initial Ir(IV) concentration in 0.55 M HCl solutions. The line is drawn to guide the eye.

INAA results for functionalized and non-functionalized gold-coated chips are summarized in Table 12 and Table 13, respectively. Ir(IV) was barely adsorbed on precleaned gold-coated chips without SAMs which can be seen in Table 13, the highest surface saturation of <20% was observed at 5.4 µM initial Ir(IV) concentration.

Table 12. The measured concentration of Ir(IV) in 0.55 M HCl solutions before and after sorption, and comparison of the surface saturation of functionalized gold-coated chips with Ir(IV).

	Substrate		
	Im-C$_{11}$-SH SAMs on precleaned gold-coated chips		
$C_{Ir\ init}$ ($\cdot 10^{-8}$ M)	51.35$\pm$0.26[a]	104.4$\pm$0.5[b]	543.1$\pm$3.2[a]
$C_{Ir\ eq}$ ($\cdot 10^{-8}$ M)	50.93$\pm$0.26	100.2$\pm$0.5	514.3$\pm$3.1
V_{Ir}, mL	2	3	3
ΔN_{Ir} ($\cdot 10^{14}$ molecules)	0.08$\pm$0.07	0.75$\pm$0.12	3.5$\pm$0.5
N_{SAMs} ($\cdot 10^{14}$ molecules/cm^2) [52]	4.5		
SS (%)	1.7$\pm$1.5	16.7$\pm$2.7	77$\pm$12

a – silicon chip coated with 100 nm of gold

b – glass chip coated with 50 nm of gold

Table 13. The measured concentration of Ir(IV) in 0.55 M HCl solutions before and after sorption, and comparison of the surface saturation of non-functionalized gold-coated chips with Ir(IV).

	Substrate		
	Precleaned gold-coated chips without SAMs		
$C_{Ir\ init}$ ($\cdot 10^{-8}$ M)	51.35$\pm$0.26[a]	104.4$\pm$0.5[b]	543.1$\pm$3.2[a]
$C_{Ir\ eq}$ ($\cdot 10^{-8}$ M)	50.98$\pm$0.26	102.1$\pm$0.5	540.0$\pm$3.2
V_{Ir}, mL	2	3	3
ΔN_{Ir} ($\cdot 10^{14}$ molecules)	<1.3	0.40$\pm$0.12	<0.9
N_{SAMs} ($\cdot 10^{14}$ molecules/cm^2) [52]	4.5		
SS (%)	<2.9	9.0$\pm$2.7	<20

a – silicon chip coated with 100 nm of gold

b – glass chip coated with 50 nm of gold

Similarly, the surface saturation with Ir(IV) was studied on gold-coated glass chips functionalized with MDDA SAMs deposited from a 5 mM ethanolic thiol solution. The substrates were submerged in Ir(IV) solutions with concentrations of 0.5 and 5.2 µM in 0.55 M HCl for approximately 21 h. The surface saturation was measured according to Eq. 12. The results summarized in Table 14 show that the highest surface saturation of $(84 \pm 16)\%$ was measured at 5.4 µM initial Ir(IV) concentration. The surface saturation decreases with a decrease in the initial Ir(IV) concentration.

Table 14. The measured concentration of Ir(IV) in 0.55 M HCl solutions before and after sorption, and comparison of the surface saturation of functionalized gold-coated glass chips with Ir(IV).

	Substrate	
	MDDA SAMs on precleaned gold-coated glass chips	
$C_{Ir\ init}$ ($\cdot 10^{-8}$ M)	51.71 ± 0.26	543.1 ± 3.2
$C_{Ir\ eq}$ ($\cdot 10^{-8}$ M)	51.56 ± 0.21	522.1 ± 2.2
V_{Ir}, mL	3	3
ΔN_{Ir} ($\cdot 10^{14}$ molecules)	<0.09	3.8 ± 0.7
N_{SAMs} ($\cdot 10^{14}$ molecules/cm^2) [52]	4.5	
SS (%)	<2.0	84 ± 16

INAA was also performed to study the Rh sorption, but the uncertainties of the measurements were very high. The cross-sections of the ^{191}Ir(n,g)^{192}Ir and the ^{103}Rh(n,g)^{104m}Rh reactions performed during the INAA analysis are 954 ± 10 b and 145 ± 2 b, respectively [141]. The difference of approximately one order of magnitude can explain less production of ^{104m}Rh compared to ^{192}Ir as well as fewer counts in the ^{104m}Rh photopeak as shown in Figure 37.
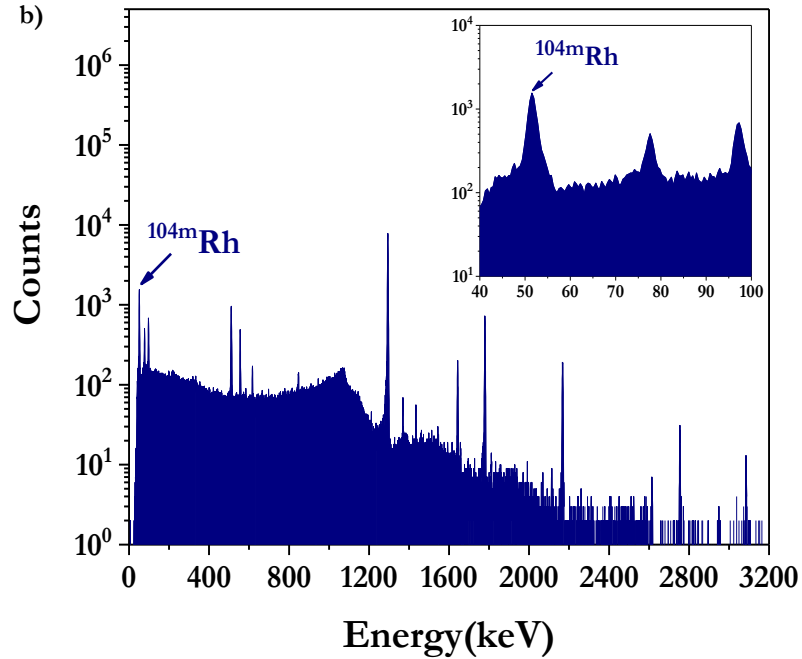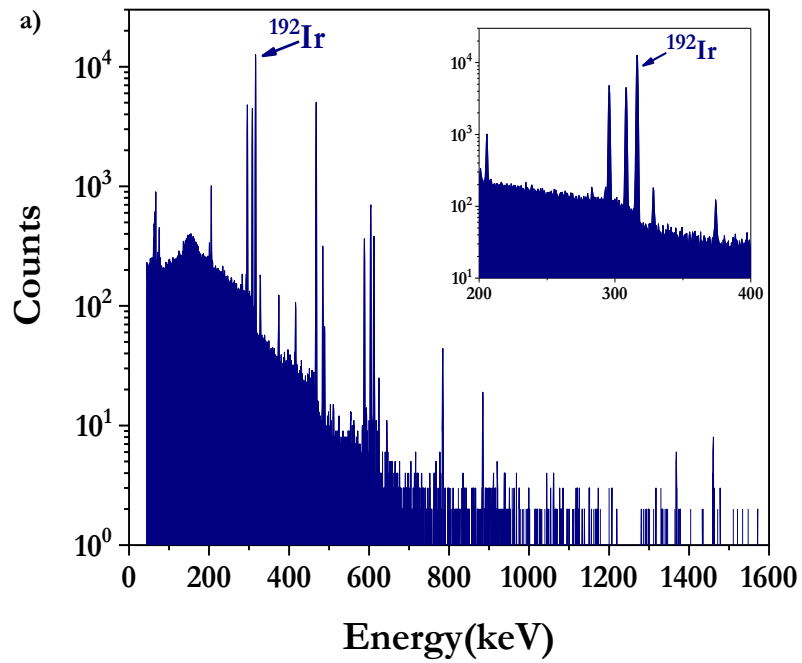
Figure 37. Gamma-ray spectra of (a) ^{192}Ir and (b) ^{104m}Rh as measured with an HPGe detector showing full energy photopeaks at 316.51 keV and 51.42 keV, respectively. The insets of the spectra show the positions of the named photopeaks.

Additionally, the gamma-ray branching ratio for ^{104m}Rh, which is 48% [142], is much lower than that for ^{192}Ir which is 83% [143]. All of the mentioned above explain the increased uncertainties during Rh measurements.

3.3   Conclusion

In this work, the surface characterization of gold-coated silicon chips functionalized with 1-(11-mercaptoundecyl)imidazole and 12-mercaptododecanoic acid self-assembled monolayers was performed. For Im-C$_{11}$-SH SAMs, AFM revealed that the SAMs deposition, as well as the liquid-UVPO treatment, do not affect the surface morphology and topology. The surface roughness values remain in the order of 1.20-1.25 nm. NP-SIMs showed that the highest surface coverage of $(99 \pm 6)\%$ was reached when the SAMs deposition was performed from a 5mM Im-C$_{11}$-SH solution. Precleaning of gold-coated silicon chips using the liquid-UVPO treatment allowed the use of surfaces free of numerous contaminants. The XPS stability study of Im-C$_{11}$-SH and MDDA SAMs under ambient laboratory conditions indicated that the functionalized gold-coated chips remain stable within at least a month of their storage in closed wafer carrier trays, wrapped with aluminum foil. This makes it possible to use Im-C$_{11}$-SH and MDDA SAMs for the functionalization of gold-coated silicon detectors utilized during online cyclotron-based experiments. Also, the liquid-UVPO treatment was found to be an effective technique to regenerate the gold surfaces covered with Im-C$_{11}$-SH SAMs. Finally, ellipsometry results proved the with a thickness of 1.690 ± 0.014 nm on the surface of gold. After one week of sample storage, the thickness remained relatively the same which excludes degradation processes during this period. NP-SIMS and INAA illustrated the successful sorption of Rh(III) and Ir(IV), respectively, on precleaned functionalized gold-coated chips. The coverage of Im-C$_{11}$-SH SAMs with Rh(III) was

measured to be (81.3 ± 3.8)% using NP-SIMS. INAA results led to the conclusion that Ir(IV) can be adsorbed from 5.4 μM Ir(IV) solutions in 0.55 M HCl on gold-coated silicon chips functionalized with Im-C$_{11}$-SH SAMs and gold-coated glass chips functionalized with MDDA SAMs with the surface saturation of (77 ± 12)% and (84 ± 16)%, respectively. The observed sensitivity of the functionalized gold-coated chips to the Rh(III) and Ir(IV) sorption allows to use the functionalized gold-coated silicon detectors during online cyclotron-based experiments.

3.4 Online Cyclotron-Based Experiments

The results of the experiment aimed at three fusion-evaporation reactions: ^{118}Sn(^{40}Ar, 5n)^{153}Er, ^{165}Ho(^{40}Ar, 5n)^{200}At, and ^{141}Pr(^{40}Ar, 5n)^{176}Ir utilizing non-functionalized and functionalized silicon detectors are discussed in this chapter. Details of the performed nuclear reactions as well as technical details of the experimental setup are discussed in Section 2.3.3.

3.4.1 Radionuclide detection on non-functionalized and functionalized silicon detectors

The effect of the detector position in the detector chamber, and the detector material on the ^{152,153}Er, $^{199-201}$At, and $^{173-176}$Ir rates was investigated. The materials tested were bare silicon (Bare Si), gold-coated silicon (Si+Au), gold-coated silicon functionalized with Im-C$_{11}$-SH SAMs (C11-Im), and gold-coated silicon functionalized with MDDA SAMs (MDAA). Four configurations: A, B, C, and D presented in Figure 38 were tested by cycling detectors through each position inside the detector chamber. So, each detector had the possibility to be in each position once.

Positions

	4	3	2	1	
Configuration A	C11-Im	MDDA	Si+Au	Si	
Configuration B	Si+Au	Si	C11-Im	MDDA	**He flow** ←
Configuration C	Si	Si+Au	MDDA	C11-Im	
Configuration D	MDDA	C11-Im	Si	Si+Au	
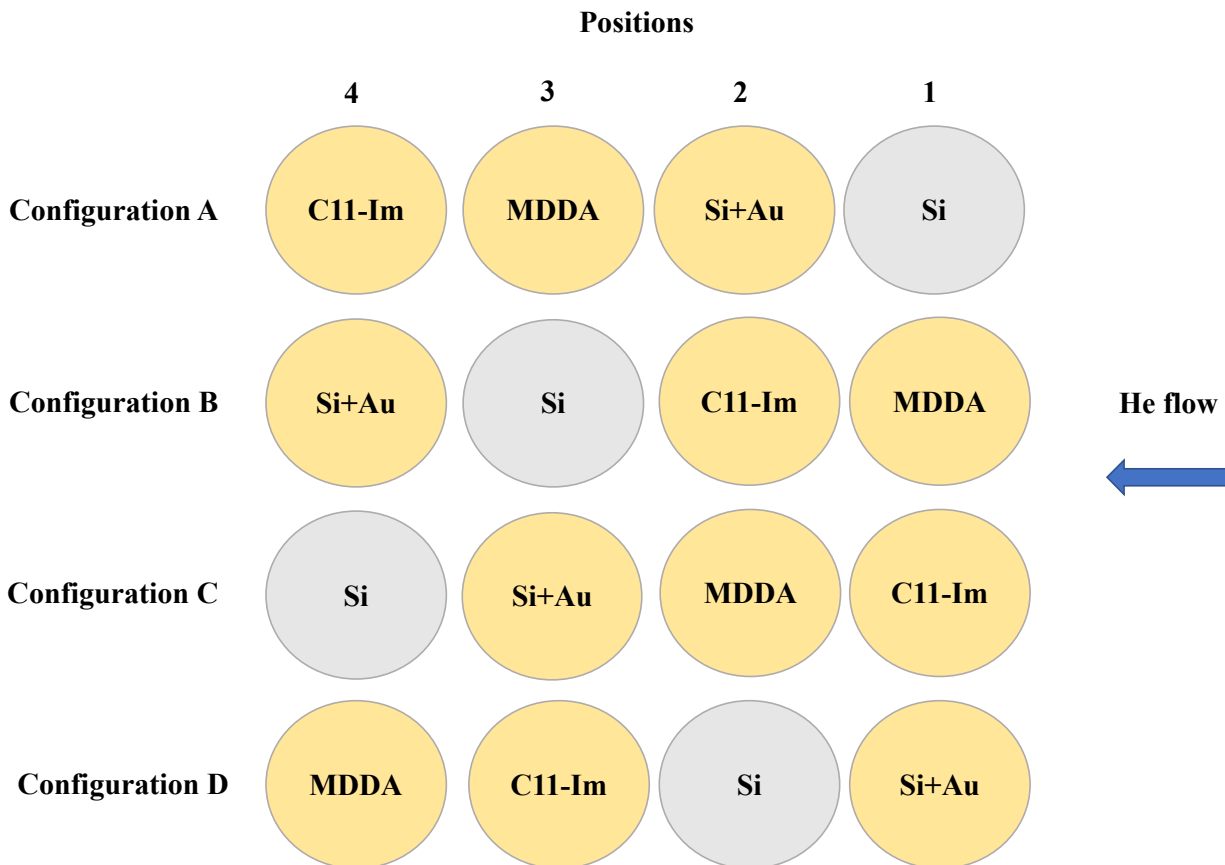
Figure 38. A schematic diagram of four configurations tested during the experiment. The blue arrow shows the entrance of the sRTC.

3.4.1.1 Multiple-peak Fit Analysis

The obtained ^{152,153}Er, $^{199-201}$At, and $^{173-176}$Ir spectra shown in Figure 42, Figure 44, and Figure 46 as black histograms contain wide peaks. This suggests that several components might be present: products of a performed nuclear reaction, as well as their decay products whose α-decay lines overlap. The multiple-peak fit makes it possible to distinguish the components by fitting them individually [144]. In the present case, an asymmetric double-sigmoidal function was used in Origin® to fit the experimental data, and individual peaks of nuclides were obtained as depicted in Figure 42, Figure 44, and Figure 46.

The asymmetric double-sigmoidal function is defined as:

$$y = y_o + A \cdot \frac{1}{1+e^{-\frac{x-x_c+\frac{\omega_1}{2}}{\omega_2}}} \cdot \left(1 - \frac{1}{1+e^{-\frac{x-x_c-\frac{\omega_1}{2}}{\omega_3}}}\right), \qquad \text{Eq. 13}$$

where y_o is the offset, x_c is the centroid of a nuclide peak, A is the amplitude, ω_1 is the full width at half maximum, ω_2 is the variance of the low-energy side, ω_3 is the variance of the high-energy side. ω_1, ω_2, ω_3 are the width parameters that were determined from calibration spectra of ^{152,153}Er, $^{199-201}$At, and $^{173-176}$Ir.

A calibration spectrum for ^{152,153}Er shown in Figure 39 as a black histogram was collected on the Bare Si detector that was placed vertically in the detector chamber. The detector surface is perpendicular to the trajectory of produced ions of interest in such a position. The rotating degrader was set to 80 degrees. The sRTC was kept under a vacuum. All of these settings give the possibility to observe the highest count rate of ^{152,153}Er. Utilizing Eq. 13, the best fit was obtained when centroids of a parent nuclide and its β^+-decay daughter nuclide were selected: 4804 keV for ^{152}Er and 4386 keV for ^{152}Ho, respectively [145]. The solid green and orange curves represent individual α-decay lines of the named nuclides, respectively. The solid pink curve is the cumulative fit peak which is in good agreement with the original histogram. Fitting the calibration spectrum allowed the three width parameters to be determined as listed in Table 15. The values are shared for each peak within the same calibration spectrum.
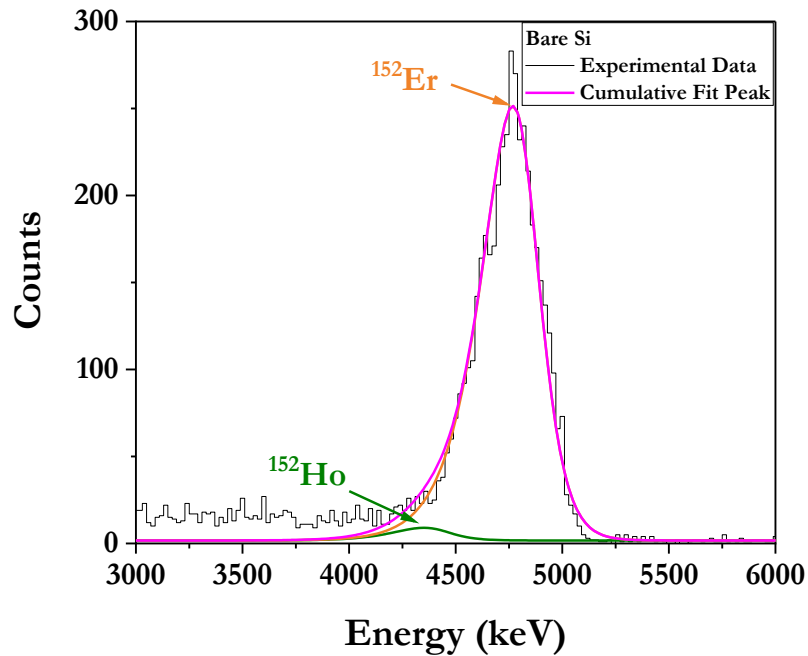
Figure 39. ^{152}Er calibration spectrum (black histogram) collected on the vertical Bare Si detector with the rotating degrader at 80 degrees. Bin width: 20 keV. The peaks were fitted using Eq. 13.

A calibration spectrum for $^{199-201}$At shown in Figure 40 as a black histogram was collected on the Bare Si detector that was placed vertically in the detector chamber. The rotating degrader was set to 90 degrees. The sRTC was kept under a vacuum. Utilizing Eq. 13, the best fit was obtained when centroids of parent nuclides were selected: 6342 keV for ^{201}At [146], 6465 keV for ^{200}At [112], and 6643 keV for ^{199}At [147]. The solid green, blue, and orange curves represent individual α-decay lines of the named nuclides, respectively. The solid pink curve is the cumulative fit peak which is in good agreement with the original histogram. The three width parameters were determined as listed in Table 15.
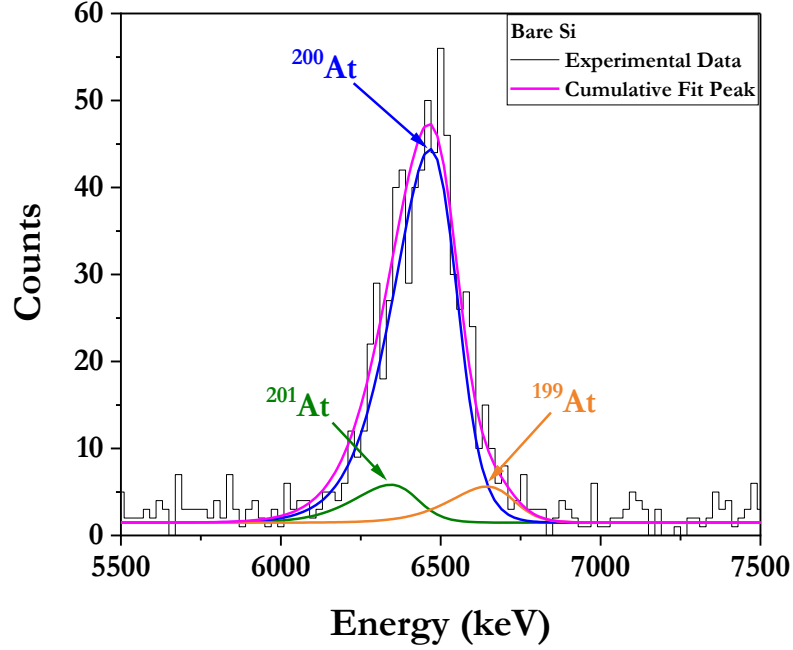
Figure 40. $^{199-201}$At calibration spectrum (black histogram) collected on the vertical Bare Si detector with the rotating degrader at 90 degrees. Bin width: 20 keV. The peaks were fitted using Eq. 13.

A calibration spectrum for $^{173-176}$Ir illustrated in Figure 41 is a sum of $^{173-176}$Ir spectra collected on the Bare Si, the Si+Au, the C11-Im detectors in configuration D, and the Bare Si, the Si+Au detectors in configuration A. In addition, for each of the named detectors, $^{173-176}$Ir spectra collected at every rotating degrader angle were summed up to obtain a final spectrum. The summation was done to enable the fitting of the data with low statistics. The sRTC was filled with He gas under the pressure of 350 Torr. Utilizing Eq. 13, the best fit was obtained when centroids of parent nuclides were selected: 5118 keV for ^{176}Ir [108], 5275 keV for ^{174}Ir [148], and 5406 keV for ^{173,175}Ir. The energy for ^{173,175}Ir is presented as an average of 5418 keV and 5393 keV for ^{173}Ir [149] and ^{175}Ir [150], respectively. Also, the centroid of the ^{153}Er granddaughter nuclide was selected: 3967 keV for ^{149}Tb [151]. The ^{152}Er β^+-decay granddaughter nuclide, ^{152}Dy, at 3628 keV might also be observed, but the α-branching ratio is only 0.1% for which reason this nuclide's

centroid was not selected for fitting [145]. The nuclear reaction $^{141}Pr(^{40}Ar, 5n)^{176}Ir$ was performed after $^{118}Sn(^{40}Ar, 5n)^{153}Er$, this is why the long-lived nuclides ^{149}Tb and ^{152}Dy with half-lives of 4.118±0.025 h [151] and 2.38±0.02 h [145], respectively, can be observed in the $^{173-176}Ir$ spectra. The three width parameters obtained after the multiple-peak fit analysis of the $^{152,153}Er$ calibration spectrum were used to fit the $^{173-176}Ir$ calibration spectrum. The assumption was made based on the fact that both Er and Ir are non-volatile elements. It was not possible to determine width parameters from the $^{173-176}Ir$ calibration spectrum due to low statistics. The solid green, blue, orange, and red curves represent individual α-decay lines of the named nuclides, respectively. The solid pink curve is the cumulative fit peak which is in good agreement with the original histogram. The peak that is attributed to ^{149}Tb (red curve) is overlapping with the cumulative fit peak, as a result, it is represented by the pink curve. Three width parameters were determined as listed in Table 15.
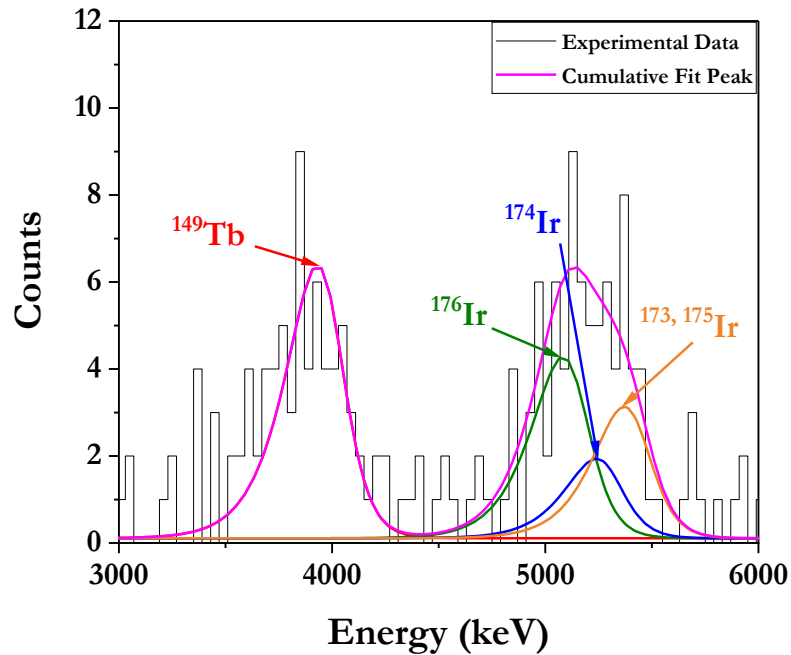
Figure 41. Sum of $^{173-176}Ir$ spectra collected on the Bare Si, the Si+Au, the C11-Im detectors in configuration D, and the Bare Si, the Si+Au detectors in configuration A (black histogram). All rotating degrader angles have been summed up. Bin width: 40 keV. The peaks were fitted using Eq. 13.

Table 15. Alpha-decay information for the studied nuclides and the determined fit parameters.

	Nuclide								
	^{152}Ho	^{152}Er	^{201}At	^{200}At	^{199}At	^{149}Tb	^{176}Ir	^{174}Ir	$^{173,\,175}$Ir
x_c, keV	4386	4804	6342	6465	6643	3967	5118	5275	5406
$T_{1/2}$	161.8±0.3 s	10.3±0.1 s	83±2 s	43±1 s	6.92±0.13 s	4.118±0.025 h	8.6±0.4 s	7.9±0.6 s	^{173}Ir: 9.3±0.6 s ^{175}Ir: 9±2 s
I, %	12	91	59	57	90	17	2.6	0.5	^{173}Ir: 4 ^{175}Ir: 0.9
y_o	1.70±0.14		1.47±0.11			0.109±0.017			
A	21±9	704±59	7±12	69±25	8±6	17.7±0.6	11.7±1.1	5.1±1.7	8.5±1.2
ω_1	58.7±17.6		146±47			59			
ω_2	124.4±3.3		80±23			124			
ω_3	66.1±2.2		37±14			66			

Fixing the determined width parameters and the centroids of possible nuclides present in a spectrum being analyzed allows to perform the multiple-peak fit and obtain individual α-decay lines as a result. The fitted ^{152,153}Er, $^{199-201}$At, and $^{173-176}$Ir spectra are shown in Figure 42, Figure 44, and Figure 46 and discussed in the next section.

3.4.1.2 ^{152,153}Er detection on non-functionalized and functionalized silicon detectors

Figure 42 shows the ^{152,153}Er spectra as black histograms collected on the Bare Si and the Si+Au detectors in configuration A with the rotating degrader at 55 degrees. At such an angle, the highest rate of ^{152,153}Er was detected. The multiple-peak fit analysis of these spectra allowed to distinguish the peaks of parent nuclides: ^{153}Er at 4674 keV [110] and ^{152}Er at 4804 keV [145], as well as their decay products. The ^{153}Er long-lived granddaughter nuclide, ^{149}Tb, at 3967 keV is observed. Also, the ^{153}Er β^+-decay daughter nuclide, ^{153}Ho, at 3910 keV might be observed, but the α-branching ratio is only 0.05% for which reason this nuclide's centroid was not selected for fitting. Lastly, the peak of the ^{152}Er β^+-decay daughter nuclide, ^{152}Ho, at 4386 keV was distinguished as well. The solid blue, orange, red, and green curves represent individual α-decay lines of the named nuclides, respectively.

The pink curve is the cumulative peak which is in good agreement with the original histogram. The α-decay information for the studied nuclides and the width parameters used to perform the multiple-peak fit analysis are presented in Table 16. The width parameters were determined from the ^{152}Er calibration spectrum and shared for all peaks within the analyzed spectrum. Likewise, the fit was performed for two other spectra collected on the MDDA and the C11-Im detectors within this configuration, as well as all for spectra collected in three other configurations at the same rotating degrader angle.
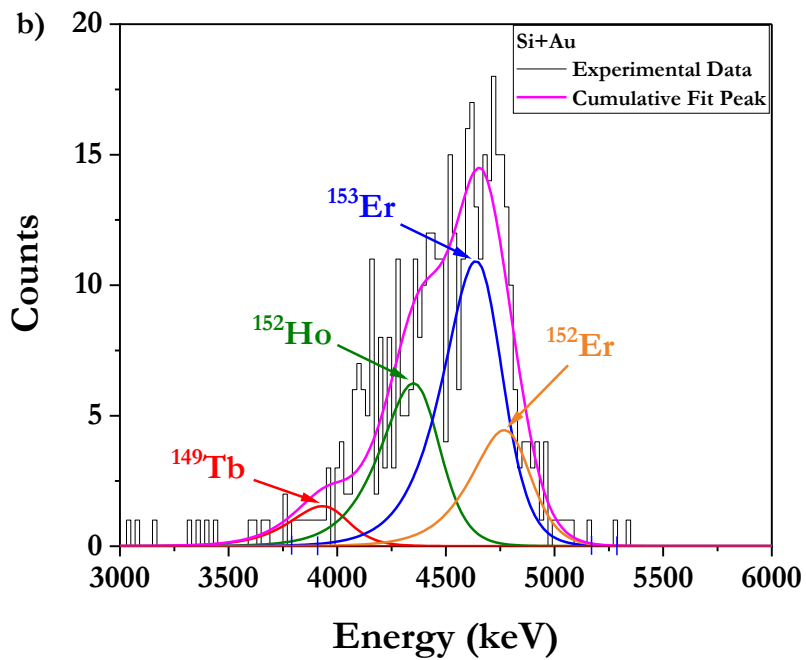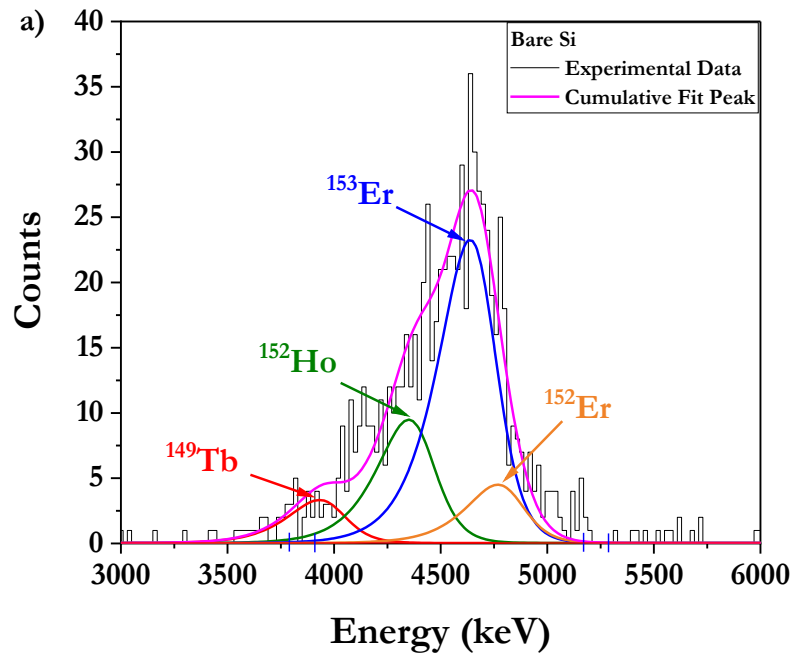
Figure 42. ^{152,153}Er spectra (black histograms) collected on: (a) the Bare Si detector, (b) the Si+Au detector in configuration A with the rotating degrader at 55 degrees. Bin width: 20 keV. The peaks were fitted using Eq. 13.

Table 16. Alpha-decay information for the studied nuclides and the width parameters used to perform the multiple-peak fit analysis of ^{152,153}Er spectra.

	Nuclide			
	^{149}Tb	^{152}Ho	^{152}Er	^{153}Er
x_c, keV	3967	4386	4804	4674
$T_{1/2}$	4.118±0.025 h	161.8±0.3 s	10.3±0.1 s	37.1±0.2 s
I, %	17	12	91	53
ω_1	58.7			
ω_2	124.4			
ω_3	66.1			

The next step was to integrate the peaks of ^{152}Er and ^{153}Er. The obtained area of each peak was divided by the bin width (20 keV in this case) to calculate the number of counts for ^{152}Er and ^{153}Er separately. Then, the normalized ^{152,153}Er count rate was calculated by dividing the sum of ^{152}Er and ^{153}Er counts by the mean of Rutherford scattering events. The general equations that were used to calculate the normalized ^{152,153}Er, $^{199-201}$At, and $^{173-176}$Ir rates can be described as follows:

$$C = \frac{P}{B} \qquad \text{Eq. 14}$$

$$R = \frac{\sum_{i=1}^{n} C_i}{RS_m} \qquad \text{Eq. 15}$$

$$RS_m = \frac{RS_E + RS_W}{2}, \qquad \text{Eq. 16}$$

where C is the number of counts of a nuclide, P is the peak area, B is the bin width, R is the normalized rate of a nuclide, $\sum_{i=1}^{n} C_i$ is the sum of isotopes' counts representing the total number of counts for one element, n is the number of isotopes of one element that were detected and used to calculate the total number of counts, RS_m is the mean of Rutherford scattering events, RS_E and RS_W is the number of Rutherford scattering events collected on the Rutherford East and

West detectors, respectively, that were obtained by integrating the corresponding peaks in the Rutherford East and West spectra.

To calculate the absolute error of the normalized rate, the following equations were used:

$$\delta R = R \cdot \sqrt{\left(\frac{\delta \sum_{i=1}^{n} C_i}{\sum_{i=1}^{n} C_i}\right)^2 + \left(\frac{\delta RS_m}{RS_m}\right)^2} \qquad \text{Eq. 17}$$

$$\delta C_n = \sqrt{C_n} \qquad \text{Eq. 18}$$

$$\delta \sum_{i=1}^{n} C_i = \sqrt{(\delta C_1)^2 + (\delta C_2)^2 + \cdots + (\delta C_n)^2} = \sqrt{C_1 + C_2 + \cdots + C_n} \qquad \text{Eq. 19}$$

$$\delta RS_{E \ or \ W} = \sqrt{RS_{E \ or \ W}} \qquad \text{Eq. 20}$$

$$\delta RS_m = \frac{\sqrt{(\delta RS_E)^2 + (\delta RS_W)^2}}{2} = \frac{\sqrt{RS_E + RS_W}}{2} \qquad \text{Eq. 21}$$

The results are summarized Table 17 and Figure 43.

Table 17. ^{152,153}Er rate obtained on detectors with four different materials at four different positions. Some values are zero due to low data statistics.

	Bare Si		MDDA		Si+Au		C11-Im		Sum	
	R, $\cdot 10^{-2}$	δR, $\cdot 10^{-2}$	R, $\cdot 10^{-2}$	δR, $\cdot 10^{-2}$	R, $\cdot 10^{-2}$	δR, $\cdot 10^{-2}$	R, $\cdot 10^{-2}$	δR, $\cdot 10^{-2}$	R, $\cdot 10^{-2}$	δR, $\cdot 10^{-2}$
Position 1	1.80	0.08	0.144	0.024	2.16	0.08	1.28	0.06	5.40	0.13
Position 2	1.07	0.06	0.72	0.05	1.00	0.06	0	0	2.79	0.10
Position 3	0	0	0.366	0.036	0.66	0.05	0.352	0.033	1.38	0.07
Position 4	0.168	0.023	0.208	0.026	0.122	0.022	0.149	0.023	0.65	0.05

The 3D plot depicted in Figure 43 shows the ^{152,153}Er rate as a function of the detector position in the detector chamber and the detector material. It represents all possible configurations

tested in the experiment. Overall, there were four detectors with four different materials at four different positions.

Figure 43. 3D plot of the ^{152,153}Er rate as a function of the detector position and material. The rotating degrader was set to 55 degrees.

The highest ^{152,153}Er rate was observed on the Bare Si (red curve) and the Si+Au detectors (pink curve). On the MDDA (blue curve) and the C11-Im (green curve) detectors, the ^{152,153}Er rate was lower. This means that the non-chemically modified Bare Si and Si+Au detectors have better efficiency in ^{152,153}Er sorption rather than the chemically modified MDDA and C11-Im detectors.

The Sum curve (navy blue curve) represents the sum of the ^{152,153}Er rate collected on four different detector materials at each position. The ^{152,153}Er rate decreases exponentially as the ions of interest first interact with a detector at position 1 and reach a detector at position 4 at last. The slope of the sum curve is provided in Section 3.4.1.5. This observation indicated that the plurality of the product gets sorbed on the first detector in the detector chamber.

3.4.1.3   [199-201]At detection on non-functionalized and functionalized silicon detectors

Figure 44 shows the [199-201]At spectra as black histograms collected on the MDDA and the C11-Im detectors in configuration C with the rotating degrader at 45 degrees. At such an angle, the highest rate of [199-201]At was detected. The multiple-peak fit analysis of these spectra allowed to distinguish peaks of parent nuclides: [201]At at 6342 keV [146], [200]At at 6465 keV [112], and [199]At 6643 keV [147]. The peak at 5952 keV primarily corresponds to the [199]At β^+-decay daughter nuclide, [199]Po, with the α-branching ratio of 12% [147]. The β^+-decay products of [200]At and [201]At: [200]Po at 5862 keV [112] and [201]Po at 5683 keV [146] might also be observed, their α-branching ratios are 11.1% and 1.6%, respectively. The solid green, blue, orange, and red curves represent individual α-decay lines of the named nuclides, respectively. The pink curve is the cumulative peak which is in good agreement with the original histogram.

The α-decay information for the studied nuclides and the width parameters used to perform the multiple-peak fit analysis are presented in Table 18. The three width parameters were determined from the [199-201]At calibration spectrum and shared for all peaks within the analyzed spectrum. Likewise, the fit was performed for two other spectra collected on the Bare Si and the Si+Au detectors within this configuration, as well as all for spectra collected in three other configurations at the same rotating degrader angle.

Figure 44. $^{199\text{-}201}$At spectra (black histograms) collected on: (a) the MDDA detector, (b) the C11-Im detector in configuration C with the rotating degrader at 45 degrees. Bin width: 40 keV. The peaks were fitted using Eq. 13.

Table 18. Alpha-decay information for the studied nuclides and the width parameters used to perform the multiple-peak fit analysis of $^{199\text{-}201}$At spectra.

	Nuclide			
	^{199}Po	^{201}At	^{200}At	^{199}At
x_c, keV	5952	6342	6465	6643
$T_{1/2}$	5.47±0.15 m	83±2 s	43±1 s	6.92±0.13 s
I, %	12	59	57	90
ω_1	150			
ω_2	80			
ω_3	40			

Similar to the ^{152,153}Er data analysis, the peak areas of ^{201}At, ^{200}At, and ^{199}At, obtained after the integration of the corresponding peaks, were divided by the bin width (40 keV in this case) to calculate the number of counts for ^{201}At, ^{200}At, and ^{199}At separately. The bin width was increased due to low statistics. Then, the normalized $^{199\text{-}201}$At rate was calculated by dividing the sum of ^{201}At, ^{200}At, and ^{199}At counts by the mean of Rutherford scattering events. The calculation was performed utilizing Eq. 14-16. The results are summarized in Table 19 and Figure 45.

Table 19. $^{199\text{-}201}$At rate obtained on detectors with four different materials at four different positions.

	Bare Si		MDDA		Si+Au		C11-Im		Sum	
	R, $\cdot 10^{-4}$	δR, $\cdot 10^{-4}$	R, $\cdot 10^{-4}$	δR, $\cdot 10^{-4}$	R, $\cdot 10^{-3}$	δR, $\cdot 10^{-3}$	R, $\cdot 10^{-4}$	δR, $\cdot 10^{-4}$	R, $\cdot 10^{-3}$	δR, $\cdot 10^{-3}$
Position 1	6.5	1.0	7.6	1.2	1.09	0.11	7.3	0.9	3.22	0.21
Position 2	4.2	0.7	3.8	0.7	0.72	0.10	1.2	0.5	1.64	0.15
Position 3	0.66	0.35	2.0	0.5	0.52	0.08	1.6	0.4	0.95	0.11
Position 4	1.8	0.5	1.06	0.36	0.32	0.08	1.3	0.4	0.74	0.11

The 3D plot depicted in Figure 45 shows the $^{199\text{-}201}$At rate as a function of the detector position in the detector chamber and the detector material.
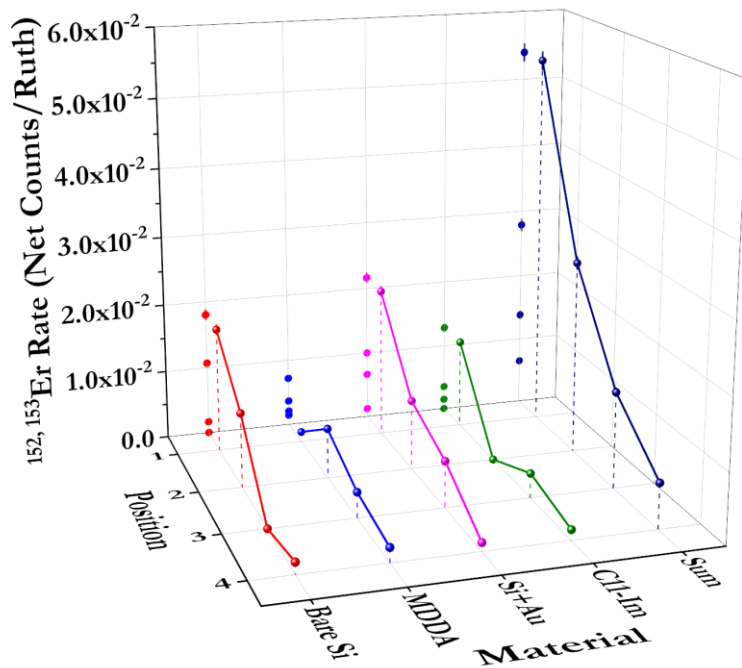

Figure 45. 3D plot of the $^{199\text{-}201}$At rate as a function of the detector position and material. The rotating degrader was set to 45 degrees.

The highest $^{199\text{-}201}$At rate was observed on the Si+Au detector (pink curve). Other materials were equally effective in the $^{199\text{-}201}$At sorption.

The trend for the Sum (navy blue curve) is similar to that for ^{152,153}Er, but the slope is different which is discussed in Section 3.4.1.5.

3.4.1.4 $^{173-176}$Ir detection on non-functionalized and functionalized silicon detectors

Figure 46 shows the $^{173-176}$Ir spectra as black histograms collected on the Bare Si and the Si+Au detectors in configuration D with all rotating degrader angles summed up. It means that for each of the named detectors, $^{173-176}$Ir spectra collected at every rotating degrader angle were summed up to obtain a final spectrum. The summation was done to enable the fitting of the data with low statistics. The multiple-peak fit analysis of these spectra made it possible to distinguish the peaks of parent nuclides: 5118 keV for ^{176}Ir [108], 5275 keV for ^{174}Ir [148], and 5406 keV for ^{173,175}Ir [149, 150]. Also, the peak at 3967 keV is attributed primarily to ^{149}Tb which is a granddaughter nuclide of ^{153}Er [151] which was produced during a previous experiment. The peak of ^{152}Dy, which is a β^+-decay granddaughter nuclide of ^{152}Er, at 3628 keV might also be observed, but the α-branching ratio is only 0.1% [145]. The solid green, blue, orange, and red curves represent individual α-decay lines of the named nuclides, respectively. The pink curve is the cumulative peak which is in good agreement with the original histogram. The peak that is attributed to ^{149}Tb (red curve) is overlapping with the cumulative fit peak, as a result, it is represented by the pink curve.

The α-decay information for the studied nuclides and the width parameters used to perform the multiple-peak fit analysis are presented in Table 15. The width parameters determined from the ^{152,153}Er calibration spectrum were used to fit the $^{173-176}$Ir spectra and shared for all peaks within the analyzed spectrum. As it was discussed in Section 3.4.1.1, the width parameters could not be determined from the $^{173-176}$Ir calibration spectrum due to low statistics. Likewise, the fit was performed for two other spectra collected on the MDDA and the C11-Im detectors within this configuration, as well as all for spectra collected in three other configurations with all rotating degrader angles summed up.
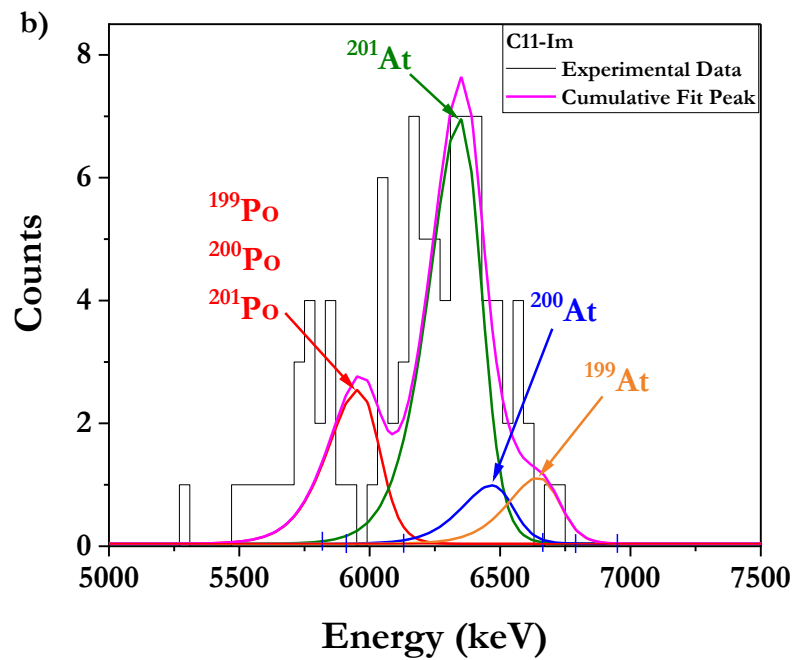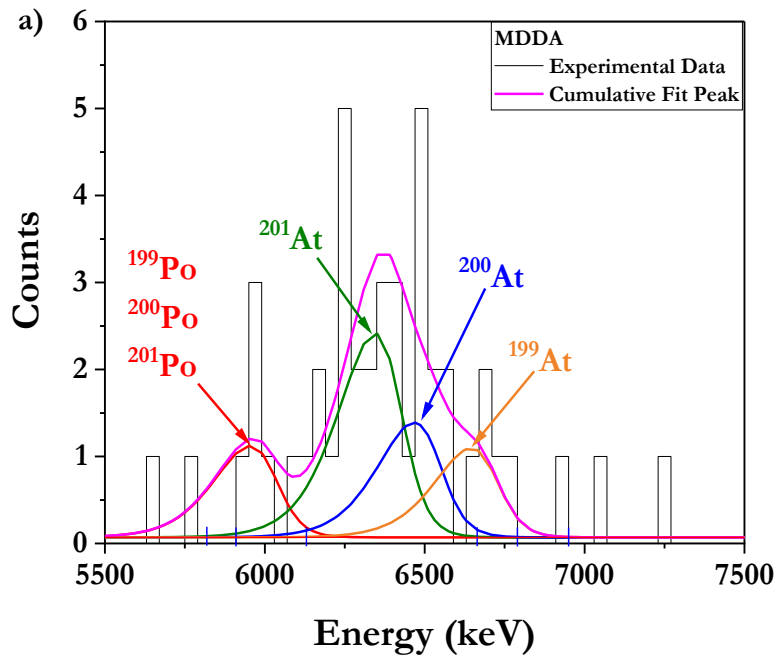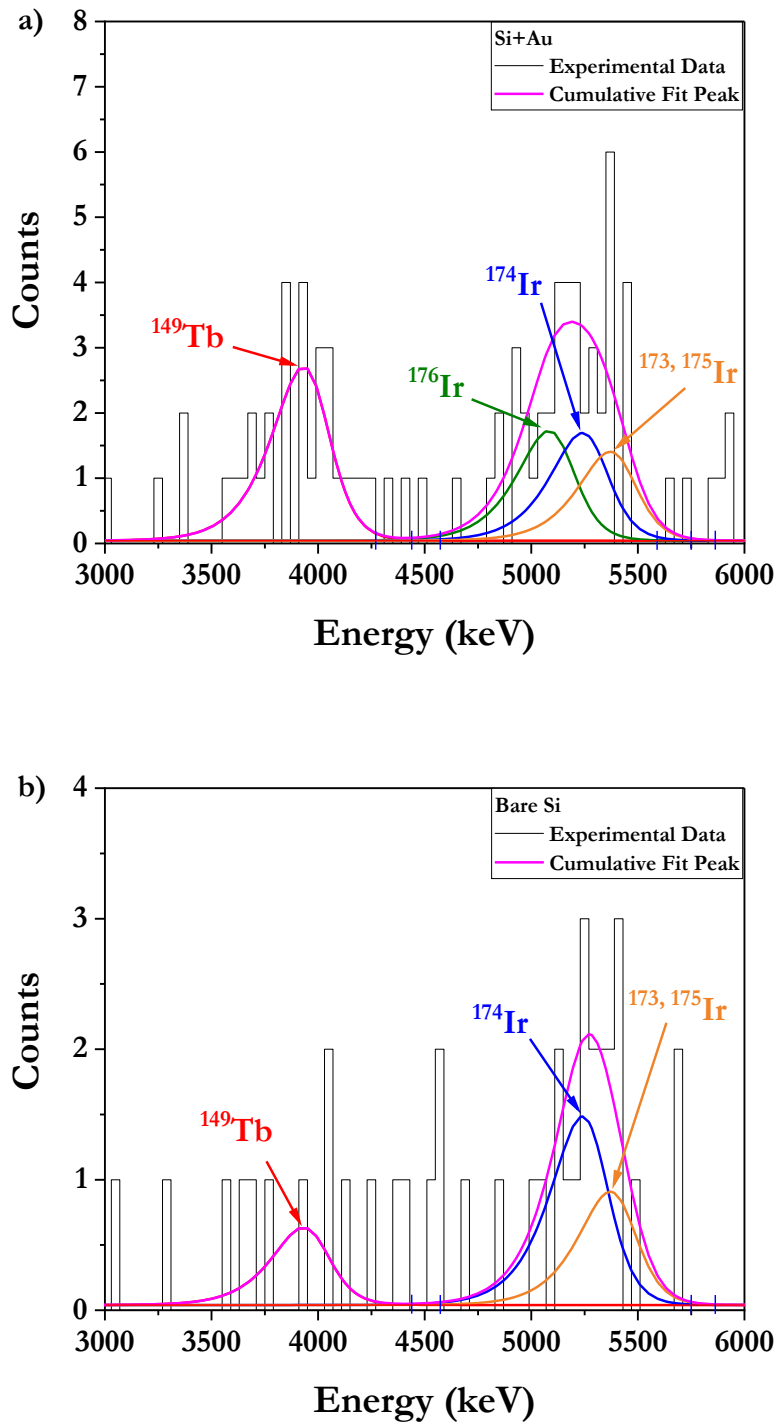
Figure 46. [173-176]Ir spectra (black histograms) collected on: (a) the Bare Si detector, (b) the Si+Au detector in configuration D. All rotating degrader angles summed up. Bin width: 40 keV. The peaks were fitted using Eq. 13.

Similar to the ^{152,153}Er and the $^{199-201}$At data analyses, the peak areas of ^{176}Ir, ^{174}Ir, and ^{173,175}Ir, obtained after the integration of the corresponding peaks were divided by the bin width (40 keV in this case) to calculate the number of counts for ^{176}Ir, ^{174}Ir, and $^{173,\,175}$Ir separately. The bin width was increased due to low statistics. Then, the normalized $^{173-176}$Ir rate was calculated by dividing the sum of ^{176}Ir, ^{174}Ir, and $^{173,\,175}$Ir counts by the mean of Rutherford scattering events. The calculation was performed utilizing Eq. 14-16. The results are summarized in Table 20 and Figure 47.

Table 20. $^{173-176}$Ir rate obtained on detectors with four different materials at four different positions. For some materials, the rates are zero because they could not be determined due to low statistics.

	Bare Si		MDDA		Si+Au		C11-Im		Sum	
	R, $\cdot10^{-5}$	δR, $\cdot10^{-5}$	R	δR	R, $\cdot10^{-5}$	δR, $\cdot10^{-5}$	R, $\cdot10^{-5}$	δR, $\cdot10^{-5}$	R, $\cdot10^{-4}$	δR, $\cdot10^{-4}$
Position 1	6.9	1.5	0	0	9.1	1.4	9.8	2.2	2.57	0.29
Position 2	4.5	1.0	0	0	5.4	1.3	5.2	1.2	1.50	0.20
Position 3	2.6	0.8	0	0	3.5	1.3	3.7	0.9	0.99	0.18
Position 4	0	0	0	0	0	0	1.1	0.6	0.11	0.06

The 3D plot depicted in Figure 47 shows the $^{173-176}$Ir rate as a function of the detector position in the detector chamber and the detector material.
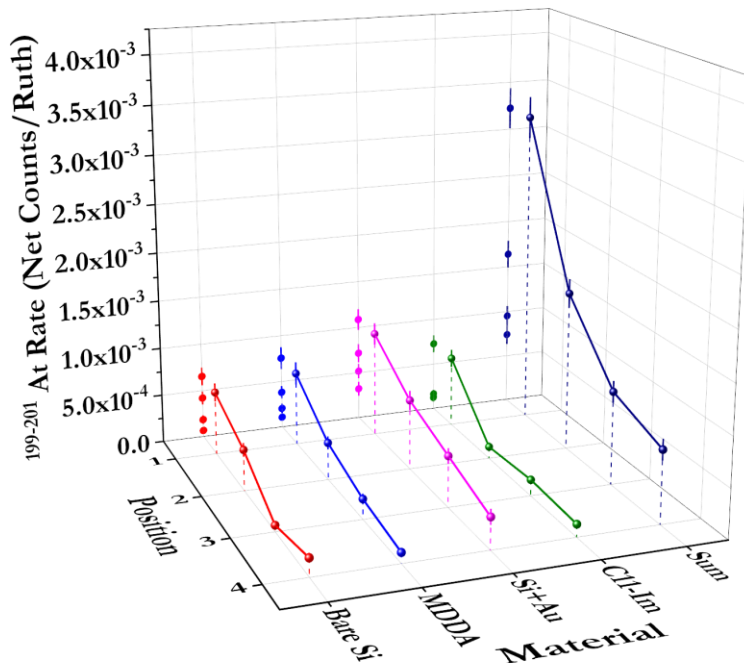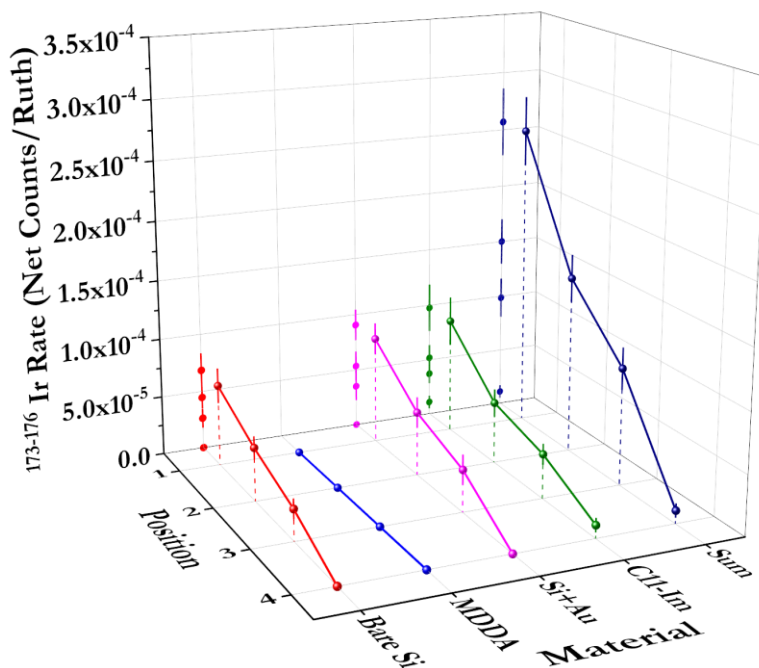

Figure 47. 3D plot of the $^{173-176}$Ir rate as a function of the detector position and material. All rotating degrader angles summed up.

All materials were equally effective in the $^{173-176}$Ir sorption. In the case of the MDDA detector, the $^{173-176}$Ir rate could not be determined.

The trend for the Sum (navy blue curve) is similar to that for ^{152,153}Er and $^{199-201}$At. However, the slope is different, and a more rapid decrease in the $^{173-176}$Ir rate is observed at position 4. The comparison of the sum curves is discussed in Section 3.4.1.5.

Results demonstrated that changing the detector position and material changes the sorption of nuclides under this study. In addition, the highest rate was observed at position 1 regardless of the material.

3.4.1.5   Er, At, and Ir chemical behavior study

Furthermore, the chemical behavior study of the online-produced nuclides was performed. Figure 48 illustrates three curves obtained for $^{152,\ 153}$Er (red), $^{199-201}$At (blue), and $^{173-176}$Ir (purple) after fitting the sum of the count rates as a function of position using an exponential function in Origin®. The offset was set to zero. The ^{152,153}Er rate obtained in configuration B is an outlier and was not included in calculations to plot Figure 48. The exponential function can be defined as:

$$y = y_0 + Ae^{-R_o x} = y_0 + Ae^{\lambda x}, \qquad \text{Eq. 22}$$

where y_0 is the offset, A is the initial value, $\lambda = -R_o$ is the rate constant parameter, i.e. the slope of a curve.

In the present study, λ is characteristic of the chemical behavior of elements in the sRTC. The λ values for ^{152,153}Er, $^{199-201}$At, and $^{173-176}$Ir are 0.72±0.05, 0.55±0.07, and 0.84±0.22, respectively. The comparison of the λ values summarized in Table 21 and the corresponding curves in Figure 48 confirmed that Ir and Er are non-volatile elements, whereas At is a volatile element.

Table 21. Comparison of the rate constant parameters for $^{173-176}$Ir, ^{152,153}Er, and $^{199-201}$At.

Nuclide	Chemistry	λ
$^{173-176}$Ir	Non-volatile	0.84±0.22
^{152,153}Er		0.72±0.05
$^{199-201}$At	Volatile	0.55±0.07

When the retention time of a nuclide is longer than its half-life, it gets sorbed mostly on the detector in the first position and decays almost immediately. As a result, a more steep slope of a curve and, respectively, a higher λ value are observed. This describes the non-volatile behavior of Ir and Er. Oppositely, when the retention time of a nuclide is shorter than its half-life, it moves further in the detector chamber up to the fourth position before it decays. As a result, a more gentle

slope of a curve and, respectively, a smaller λ value is observed. This describes the volatile behavior of At.
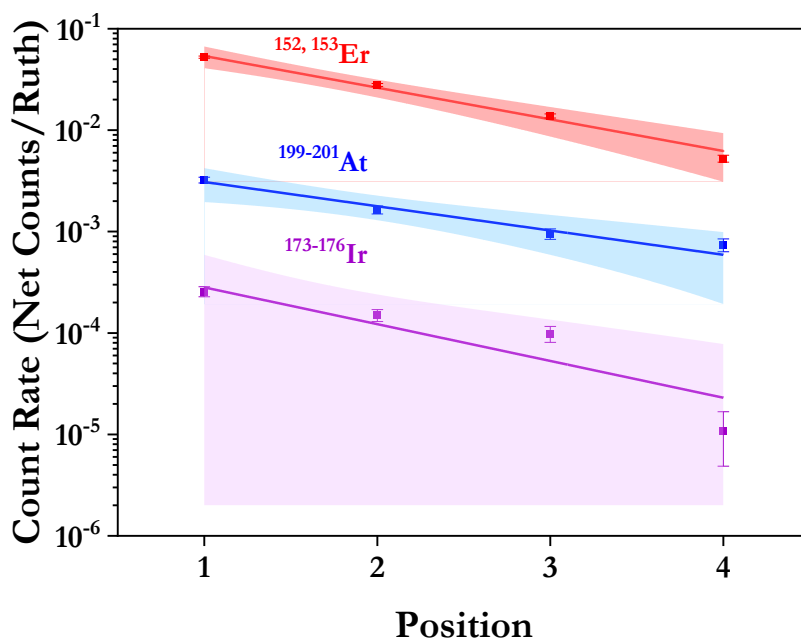
Figure 48. The count rate of $^{152, 153}$Er (red squares), $^{199-201}$At (blue squares), and $^{173-176}$Ir (purple squares) as a function of the detector position. The data were fitted using Eq. 22, the offset was set to zero. Shades represent 95% confidence bands.

The results suggest there are two possible processes: ions of interest can be sorbed on the surface of the detector, or they can decay in flight. Figure 49 shows the sum of the count rates collected on four detectors at each configuration for $^{152, 153}$Er (red squares), $^{199-201}$At (blue squares), and $^{173-176}$Ir (purple squares). The ^{152,153}Er rate obtained in configuration B is an outlier and was not included in Figure 49. The data were fitted using the linear function with the slope set to zero to find the average of the count rates for $^{152, 153}$Er (red curve), $^{199-201}$At (blue curve), and $^{173-176}$Ir (purple curve) collected at each configuration.
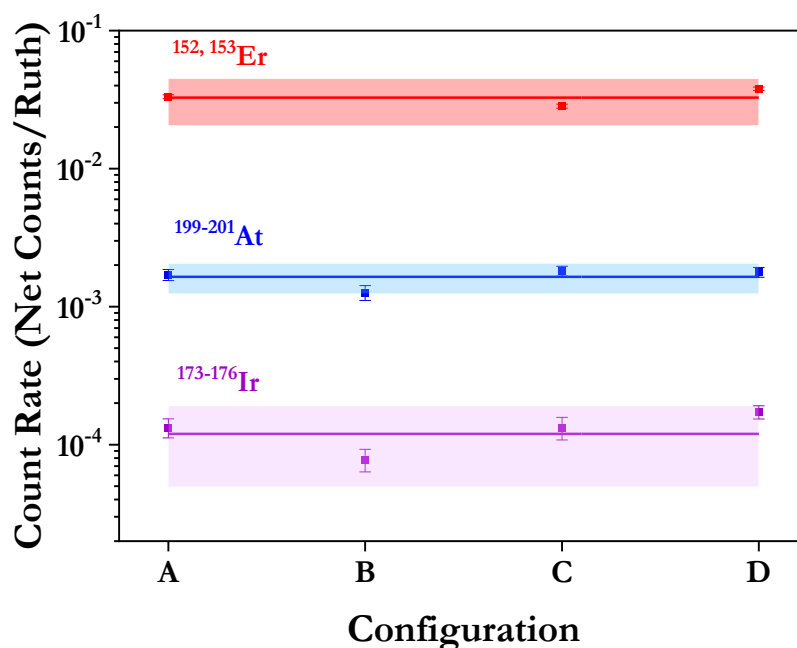
Figure 49. The count rate of $^{152, 153}$Er (red squares), $^{199-201}$At (blue squares), and $^{173-176}$Ir (purple squares) as a function of the detector configuration. The data were fitted using the linear function with the slope set to zero. Shades represent 95% confidence bands. $^{152, 153}$Er rate at configuration B is an outlier and was not included in calculations.

The results indicate that the total activity was constant regardless of the configuration. Therefore, if one detector has a higher rate than another detector within one configuration, it means that the variations are due to the interactions with the detector surface.

The sum of the count rates collected on each detector at four positions for three nuclides as a function of the detector material is depicted in Figure 50. It summarizes the ideas discussed above about the Si+Au and the Bare Si detectors being the most effective materials in the ^{152,153}Er sorption, whereas other materials are equally effective. The ^{152,153}Er rate obtained in configuration B is an outlier and was not included in Figure 50. In the case of $^{199-201}$At, only the Si+Au detector showed the preference in the $^{199-201}$At sorption, equal efficiency is observed for three other

materials. Three materials are equally effective in the $^{173-176}$Ir sorption, however, the count rate could not be determined on the MDDA detector due to low statistics.
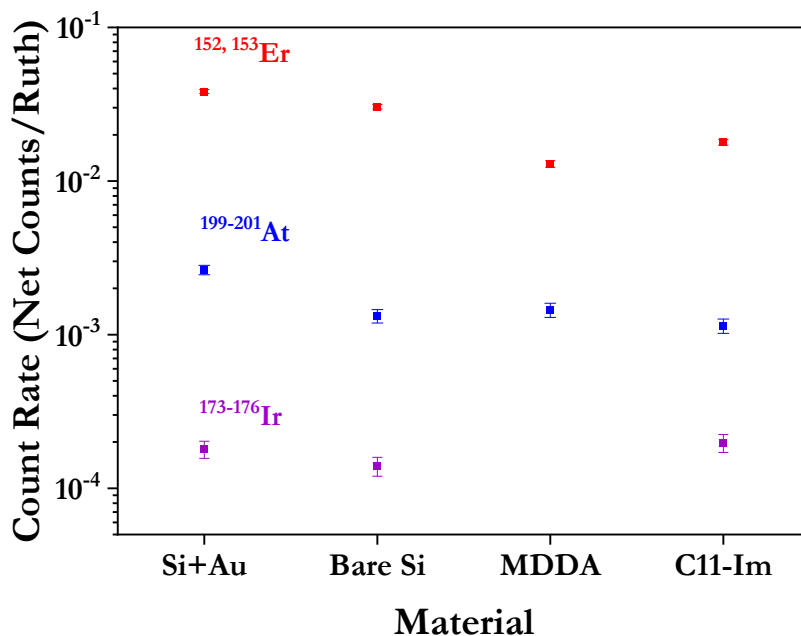
Figure 50. The count rate of $^{152,\ 153}$Er (red squares), $^{199-201}$At (blue squares), and $^{173-176}$Ir (purple squares) as a function of the detector material. Due to low statistics, $^{173-176}$Ir count rate on the MDDA detector could not be determined.

3.4.1.6   Detector resolution study

It was important to study whether the coating of a detector with gold, the SAMs deposition, and the detector usage during online cyclotron-based experiments influence the detector resolution. Alpha spectroscopy was used to collect alpha spectra of a four-peak alpha source on a silicon detector before and after it was coated with gold, as well as after it was functionalized with Im-C$_{11}$-SH SAMs and used during the online cyclotron-based experiment. The corresponding spectra are presented in Figure 51.
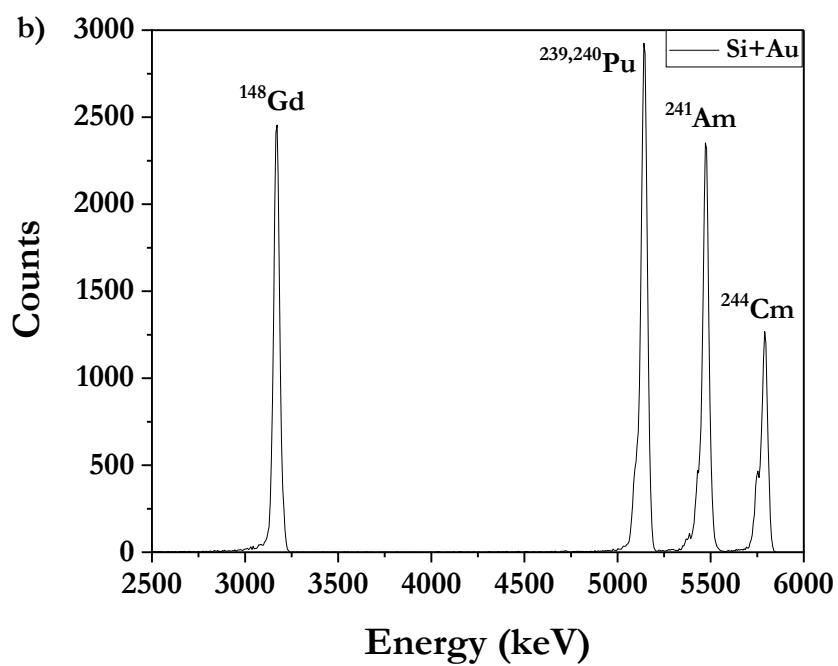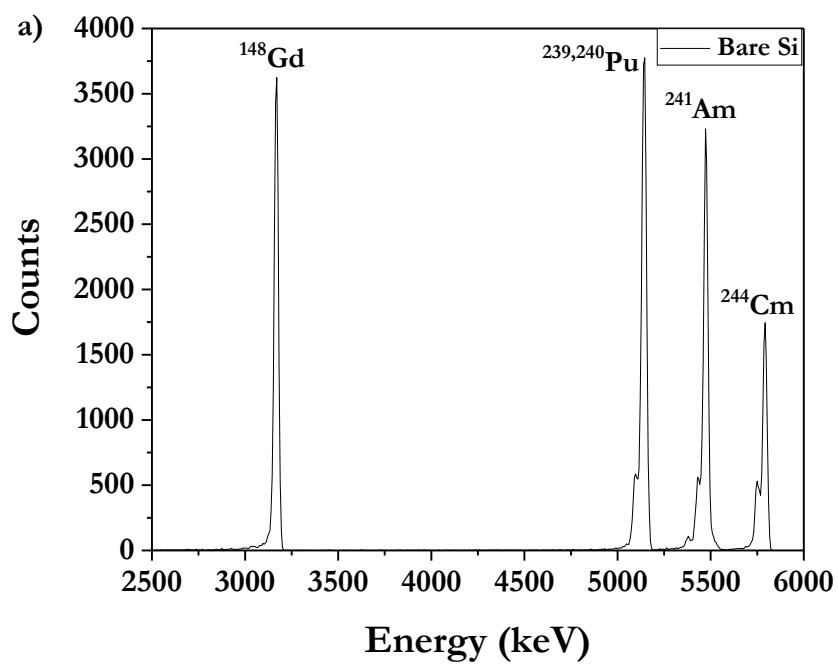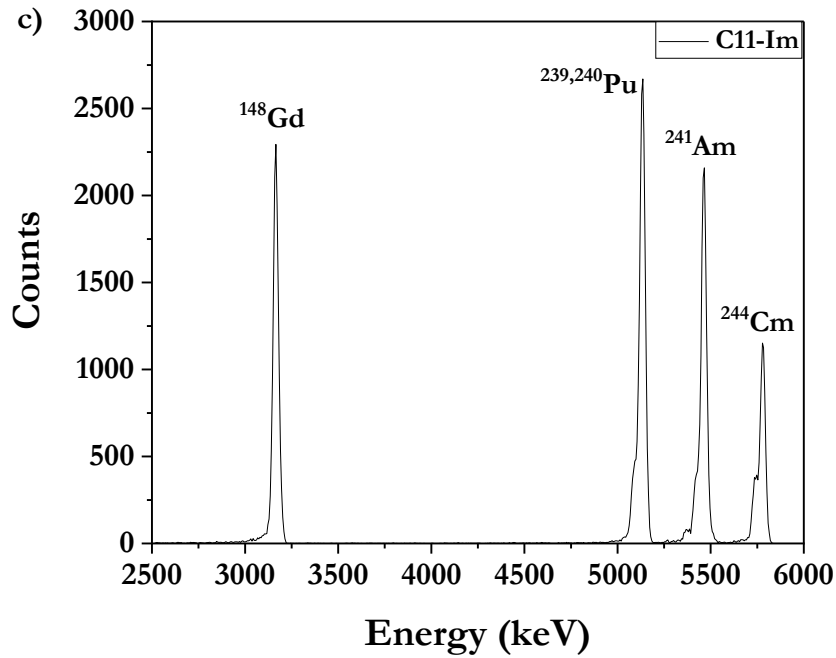
Figure 51. Alpha spectra of a four-peak alpha source collected on (a) the Bare Si; (b) the Si+Au; (c) the C11-Im detectors to measure their resolution.

The full width at half maximum (FWHM) of [148]Gd, [239,240]Pu, [241]Am, and [244]Cm peaks comprising the four-peak alpha source was measured in Genie™ 2000 Gamma Analysis Software. Then, the resolution (R_s) of the detector was measured using the following equation:

$$R_s = \frac{FWHM}{x_c}$$ Eq. 23

The detector resolution data and the centroids of peaks of the four-peak alpha source are summarized in Table 22.

Table 22. Detector resolution data extracted from alpha spectra of a four-peak alpha source collected on the silicon detector with different materials.

		Detector					
		Si	Si + Au	C11-Im after the online experiment	Si	Si + Au	C11-Im after the online experiment
Nuclide	x_c, keV	FWHM, keV			R_s, %		
^{148}Gd	3182.8	21.2	36.0	32.7	0.7	1.13	1.03
^{239}Pu	5156.6	24.4	38.5	34.7	0.5	0.75	0.67
^{241}Am	5485.6	21.2	36.9	32.5	0.39	0.67	0.59
^{244}Cm	5804.8	21.7	37.6	32.7	0.37	0.65	0.56

The FWHM and the R_s values did not increase drastically after the coating of the detector with gold, its subsequent functionalization with C11-Im SAMs, and its usage in the online experiment. These results suggest that functionalized gold-coated silicon detectors can produce well-resolved peaks of radionuclides that are alpha emitters. Additionally, they can be reused in the next online experiments having relatively the same resolution.

3.4.1.7   Conclusion

Promising results were obtained during the production of ^{152,153}Er, $^{199\text{-}201}$At, and $^{173\text{-}176}$Ir which demonstrated that changing the detector position and material changes the nuclide sorption. The highest ^{152,153}Er rate was observed on the gold-coated silicon detector and the bare silicon detectors. The highest ^{199,200,201}At rate was observed on the gold-coated detector, while others produced equal efficiency. For $^{173\text{-}176}$Ir all materials produced equal efficiency. The chemical behavior study of online-produced ^{152,153}Er, $^{199\text{-}201}$At, and $^{173\text{-}176}$Ir confirmed the non-volatile character of Er and Ir and the volatile character of At. It also revealed that detectors in the first position collected the plurality of the product. Alpha spectroscopy demonstrated that the functionalization of the detector surface as well as its usage during online cyclotron-based experiments do not result in the worse resolution of the detector, making it possible to reuse them.

CHAPTER IV

CONCLUSIONS

In the first part of this dissertation, the characterization of Im-C$_{11}$-SH and MDDA SAMs on gold-coated substrates was performed utilizing different surface science techniques. The surface morphology and topology of the functionalized gold substrates were not affected by the Im-C$_{11}$-SH SAMs deposition and the liquid-UVPO treatment used to preclean the substrates or remove the SAMs. This finding done with AFM allows reusing gold-coated substrates several times without damaging the properties of gold. The optimization of the SAMs deposition procedure revealed that the highest surface coverage of $(99 \pm 6)\%$ can be reached when 5mM ethanolic thiol solutions are used to prepare thiolate SAMs on gold. The Im-C$_{11}$-SH and MDDA SAMs were shown to be stable within at least a month of their storage in closed wafer carrier trays, wrapped with aluminum foil. This was an important result that gave a possibility to use Im-C$_{11}$-SH and MDDA SAMs for the functionalization of gold-coated silicon detectors utilized during online cyclotron-based experiments which typically can last up to one month. The obtained thickness of Im-C$_{11}$-SH SAMs proved the presence of a single thiolate monolayer on the surface of gold. The successful results were obtained during the studies of Ir(IV) and Rh(III) sorption from hydrochloric acid solutions. The coverage of Im-C$_{11}$-SH SAMs with Rh(III) was measured to be $(81.3 \pm 3.8)\%$ using NP-SIMS. The INAA results led to the conclusion that Ir(IV) can be adsorbed on Im-C$_{11}$-SH and MDDA SAMs with the surface saturation of $(77 \pm 12)\%$ and $(84 \pm 16)\%$, respectively. Knowing that the functionalized gold-coated chips are sensitive to the Ir(IV) and Rh(III) sorption let us assume that the named SAMs deposited on gold-coated silicon detectors would be effective in binding online-produced elements in the gas phase during cyclotron-based experiments.

In the second part of this dissertation, two cyclotron-based experiments were performed to test the newly developed detector setup. The results of the second experiment were described in detail in this dissertation. The sRTC was designed and used for the first time to study the chemistry of the online-produced elements, such as Ir, Er, and At. The sRTC window could maintain the pressure difference of around 350 Torr. Due to several technical issues, the count rate for Ir was significantly lower than that for Er and At. The efficiency of the thiolate-functionalized surfaces in the element adsorption was found to be comparable to that of the bare Si and the gold-coated Si detectors. Promising results were obtained during the chemical study of ^{152,153}Er, $^{199-201}$At, and $^{173-176}$Ir demonstrating the role of the detector position and its coating on the nuclide sorption. An exponential decrease of the count rate as a function of the detector position was observed for the named nuclides. The distinct distribution of the volatile and the non-volatile elements within the detector setup was obtained. The resolution of the detectors remained in the same range after the SAMs deposition as well as after their application during online cyclotron-based experiments. This allows using the named detectors multiple times in the future.

Overall, the designed detector system can be potentially applied in the future to study the adsorption properties of online-produced superheavy elements and compare them to those of their lighter homologs.

CHAPTER V

FUTURE WORK

Despite the promising results obtained during the first attempt to use the thiolate-functionalized gold-coated silicon detectors in cyclotron-based experiments, several improvements can be implemented Secondly, the size of the sRTC funnel can be decreased which will narrow the distribution of the produced ions of interest and increase the probability of their detection on the detectors located at the end of the detector chamber. Thirdly, the chemistry studies inside the sRTC were conducted under ambient temperature. In the future, the effect of other temperatures or the temperature gradient within the detector setup could be studied. The consumption of He gas which was 500-1800 standard cubic centimeters per minute can be decreased. The better design of the sRTC box can eliminate the leakage of He gas throughout an experiment. Finally, the search for potential molecules (for example, thiols based on crown ethers) which will selectively bind one element over another can be performed.

The following student in our group will study the sorption of polonium on funtionalized gold-coated silicon detectors in the gas phase. The choice of the element was dictated by its high alpha branching ratio. The student is going to functionalize the surfaces with dithiol molecules that are potentially effective in sorbing polonium.

REFERENCES

[1]   R. Eichler *et al.*, Chemical Characterization of Element 112, Nature **447**, 72 (2007). doi:10.1038/nature05761

[2]   R. Eichler *et al.*, Thermochemical and Physical Properties of Element 112, Angew. Chem. Int. Ed. **47**, 3262 (2008). doi:10.1002/anie.200705019

[3]   S. N. Dmitriev *et al.*, Pioneering Experiments on the Chemical Properties of Element 113, Mendeleev Commun. **24**, 253 (2014). doi:10.1016/j.mencom.2014.09.001

[4]   A. Yakushev *et al.*, First Study on Nihonium (Nh, Element 113) Chemistry at TASCA, Front. Chem. **9**, 1 (2021). doi:10.3389/fchem.2021.753738

[5]   *Periodic Table of Chemical Elements*, retrieved 7 August 2022, available at https://www.acs.org/content/acs/en/education/whatischemistry/periodictable.html.

[6]   G. Choppin, J.-O. Liljenzin, J. Rydberg, and C. Ekberg, *Radiochemistry and Nuclear Chemistry*, 4th ed., (Academic Press, Elsevier Inc., Kidlington, Oxford, UK; Amsterdam, The Netherlands, 2013).

[7]   M. L. Terranova and O. A. P. Tavares, The Periodic Table of the Elements: The Search for Transactinides and Beyond, Rend. Lincei Sci. Fis. Nat. **33**, 1 (2022). doi:10.1007/s12210-022-01057-w

[8]   M. Schädel, Chemistry of Superheavy Elements, Angew. Chem. Int. Ed. **45**, 368 (2006). doi:10.1002/anie.200461072

[9]   K. Morita *et al.*, Experiment on the Synthesis of Element 113 in the Reaction $^{209}Bi(^{70}Zn,n)^{278}113$, J. Phys. Soc. Japan **73**, 2593 (2004). doi:10.1143/JPSJ.73.2593

[10]   K. Morita, SHE Research at RIKEN/GARIS, Nucl. Phys. A **944**, 30 (2015). doi:10.1016/j.nuclphysa.2015.10.007

[11]   P. J. Karol, R. C. Barber, B. M. Sherrill, E. Vardaci, and T. Yamazaki, Discovery of the Element with Atomic Number $Z = 118$ Completing the 7th Row of the Periodic Table (IUPAC Technical Report), Pure Appl. Chem. **88**, 155 (2016). doi:10.1515/pac-2015-0501

[12]   S. Hofmann, The Discovery of Elements 107 to 112, EPJ Web Conf. **131**, 1 (2016). doi:10.1051/epjconf/201613106001

[13]   Y. Oganessian, Synthesis and Decay Properties of Superheavy Elements, Pure Appl. Chem. **78**, 889 (2006). doi:10.1351/pac200678050889

[14] V. Pershina, Relativity in the Electronic Structure of the Heaviest Elements and Its Influence on Periodicities in Properties, Radiochim. Acta **107**, 833 (2019). doi:doi:10.1515/ract-2018-3098

[15] A. Yakushev *et al.*, First Study on Nihonium (Nh, Element 113) Chemistry at TASCA, Front. Chem. **9**, (2021). doi:10.3389/fchem.2021.753738

[16] P. Pyykkö, in *Advances in Quantum Chemistry*, vol. 11, edited by P.-O. Löwdin (Academic Press, 1978), pp. 353–409. doi:10.1016/S0065-3276(08)60241-5

[17] A. Türler and V. Pershina, Advances in the Production and Chemistry of the Heaviest Elements, Chem. Rev. **113**, 1237 (2013). doi:10.1021/cr3002438

[18] G. Münzenberg *et al.*, Observation of One Correlated α-Decay in the Reaction ^{58}Fe on ^{209}Bi→^{267}109, Z. Phys. **309**, 89 (1982). doi:10.1007/BF01420157

[19] K. J. Moody, in *The Chemistry of Superheavy Elements*, edited by M. Schädel and D. Shaughnessy (Springer-Verlag, Berlin, Heidelberg, 2014), pp. 1–81. doi:10.1007/978-3-642-37466-1_1

[20] S. Hofmann, in *The Chemistry of Superheavy Elements*, edited by M. Schädel (Kluwer Academic Publishers, Dordrecht, 2003), pp. 1–29.

[21] G. Münzenberg *et al.*, Evidence for Element 109 from One Correlated Decay Sequence Following the Fusion of ^{58}Fe with ^{209}Bi, Z. Phys. **315**, 145 (1984). doi:10.1007/BF01419373

[22] G. Münzenberg *et al.*, New Results on Element 109, Z. Phys. **330**, 435 (1988). doi:10.1007/BF01290131

[23] *The SHIP Setup*, retrieved 24 July 2022, available at https://www.gsi.de/work/forschung/nustarenna/nustarenna_divisions/she_physik/experimental_setup/ship.

[24] S. Hofmann, F. P. Heßberger, V. Ninov, P. Armbruster, G. Münzenberg, C. Stodel, A. G. Popeko, A. V. Yeremin, S. Saro, and M. Leino, Excitation Function for the Production of ^{265}108 and ^{266}109, Z. Phys. **358**, 377 (1997). doi:10.1007/s002180050343

[25] S. L. Nelson, K. E. Gregorich, I. Dragojević, J. Dvořák, P. A. Ellison, M. A. Garcia, J. M. Gates, L. Stavsetra, M. N. Ali, and H. Nitsche, Comparison of Complementary Reactions in the Production of Mt, Phys. Rev. C **79**, 027605 (2009). doi:10.1103/PhysRevC.79.027605

119

[26] S. Hofmann *et al.*, The New Element 111, Z. Phys. **350**, 281 (1995). doi:10.1007/BF01291182

[27] S. Hofmann *et al.*, New Results on Elements 111 and 112, Eur. Phys. J. A **14**, 147 (2002). doi:10.1140/epja/i2001-10119-x

[28] Y. T. Oganessian *et al.*, Eleven New Heaviest Isotopes of Elements Z = 105 to Z = 117 Identified among the Products of ^{249}Bk+^{48}Ca Reactions, Phys. Rev. C **83**, 054315 (2011). doi:10.1103/PhysRevC.83.054315

[29] Y. T. Oganessian *et al.*, New Insights into the ^{243}Am + ^{48}Ca Reaction Products Previously Observed in the Experiments on Elements 113, 115, and 117, Phys. Rev. Lett. **108**, 022502 (2012). doi:10.1103/PhysRevLett.108.022502

[30] Y. T. Oganessian *et al.*, Synthesis of Elements 115 and 113 in the Reaction ^{243}Am + ^{48}Ca, Phys. Rev. C **72**, 034611 (2005). doi:10.1103/PhysRevC.72.034611

[31] Y. T. Oganessian *et al.*, Synthesis of the Isotope ^{282}113 in the ^{237}Np+^{48}Ca Fusion Reaction, Phys. Rev. C **76**, 011601 (2007). doi:10.1103/PhysRevC.76.011601

[32] B. Fricke, in *Recent Impact of Physics on Inorganic Chemistry*, edited by B. C. Tofield and B. Fricke (Springer, Berlin, Heidelberg, 1975), pp. 89–144.

[33] P. Pyykkö and M. Atsumi, Molecular Single-Bond Covalent Radii for Elements 1-118, Chem. Eur. J. **15**, 186 (2009). doi:10.1002/chem.200800987

[34] P. Pyykkö, S. Riedel, and M. Patzschke, Triple-Bond Covalent Radii, Chem. Eur. J. **11**, 3511 (2005). doi:10.1002/chem.200401299

[35] X. Wang and L. Andrews, Infrared Spectra of Rhodium Hydrides in Solid Argon, Neon, and Deuterium with Supporting Density Functional Calculations, J. Phys. Chem. A **106**, 3706 (2002). doi:10.1021/jp013624f

[36] M. Iliaš and V. Pershina, Carbonyl Compounds of Rh, Ir, and Mt: Electronic Structure, Bonding and Volatility, Phys. Chem. Chem. Phys. **22**, 18681 (2020). doi:10.1039/D0CP02118K

[37] A. Türler, R. Eichler, and A. Yakushev, Chemical Studies of Elements with Z⩾104 in Gas Phase, Nucl. Phys. A **944**, 640 (2015). doi:10.1016/j.nuclphysa.2015.09.012

[38] A. Yakushev and R. Eichler, Gas-Phase Chemistry of Element 114, Flerovium, EPJ Web Conf. **131**, 07003 (2016). doi:10.1051/epjconf/201613107003

[39] U. S. Geological Survey, *Mineral Commodity Summaries 2022* (Reston, VA, 2022), pp. 1–202, available at http://pubs.er.usgs.gov/publication/mcs2022. doi:10.3133/mcs2022

[40] N. T. Nassar and S. M. Fortier, *Methodology and Technical Input for the 2021 Review and Revision of the U.S. Critical Minerals List*, Report 2021-1045 (Reston, VA, 2021), pp. 1–31, available at http://pubs.er.usgs.gov/publication/ofr20211045. doi:10.3133/ofr20211045

[41] M. N. Le, M. S. Lee, and G. Senanayake, A Short Review of the Separation of Iridium and Rhodium from Hydrochloric Acid Solutions by Solvent Extraction, J. Solution Chem. **47**, 1373 (2018). doi:10.1007/s10953-018-0770-8

[42] V. Zakusilova, G. Zante, E. E. Tereshatov, C. M. Folden III, and M. Boltoeva, Extraction and Separation of Iridium(IV) and Rhodium(III) from Hydrochloric Acid Media by a Quaternary Ammonium-Based Hydrophobic Eutectic Solvent, Sep. Purif. Technol. **278**, 118814 (2021). doi:10.1016/j.seppur.2021.118814

[43] P. P. Sun and M. S. Lee, Separation of Ir(IV) and Rh(III) from Mixed Chloride Solutions by Solvent Extraction, Hydrometallurgy **105**, 334 (2011). doi:10.1016/j.hydromet.2010.11.008

[44] T. H. Nguyen and M. S. Lee, Effect of HCl Concentration on the Oxidation of LIX 63 and the Subsequent Separation of Pd(II), Pt(IV), Ir(IV) and Rh(III) by Solvent Extraction, Korean J. Met. Mater. **54**, 768 (2016). doi:10.3365/KJMM/24.2016.54.10.768

[45] F. L. Bernardis, R. A. Grant, and D. C. Sherrington, A Review of Methods of Separation of the Platinum-Group Metals through Their Chloro-Complexes, React. Funct. Polym. **65**, 205 (2005). doi:10.1016/j.reactfunctpolym.2005.05.011

[46] L. Svecova, N. Papaïconomou, and I. Billard, Rh(III) Aqueous Speciation with Chloride as a Driver for Its Extraction by Phosphonium Based Ionic Liquids, Molecules **24**, 1391 (2019). doi:10.3390/molecules24071391

[47] E. Benguerel, G. P. Demopoulos, and G. B. Harris, Speciation and Separation of Rhodium(III) from Chloride Solutions: A Critical Review, Hydrometallurgy **40**, 135 (1996). doi:10.1016/0304-386X(94)00086-I

[48]   I. Y. Lesch and I. G. Rubel, *Some Data on the Thermodynamics of Platinum Metal Compounds*, in Proceedings of Gipronickel Institute of Research and Development (Leningrad, 1964 (Russian)), pp. 26–49

[49]   D. Cozzi and F. Pantani, The Polarographic Behaviour of Rhodium(III) Chlorocomplexes, J. Inorg. Nucl. Chem. **8**, 385 (1958). doi:10.1016/0022-1902(58)80205-5

[50]   C. Vericat, M. E. Vela, G. Corthey, E. Pensa, E. Cortés, M. H. Fonticelli, F. Ibañez, G. E. Benitez, P. Carro, and R. C. Salvarezza, Self-Assembled Monolayers of Thiolates on Metals: A Review Article on Sulfur-Metal Chemistry and Surface Structures, RSC Adv. **4**, 27730 (2014). doi:10.1039/C4RA04659E

[51]   C. Vericat, M. E. Vela, G. Benitez, P. Carro, and R. C. Salvarezza, Self-Assembled Monolayers of Thiols and Dithiols on Gold: New Challenges for a Well-Known System, Chem. Soc. Rev. **39**, 1805 (2010). doi:10.1039/B907301A

[52]   J. C. Love, L. A. Estroff, J. K. Kriebel, R. G. Nuzzo, and G. M. Whitesides, Self-Assembled Monolayers of Thiolates on Metals as a Form of Nanotechnology, Chem. Rev. **105**, 1103 (2005). doi:10.1021/cr0300789

[53]   J. L. Wilbur and G. M. Whitesides, in *Nanotechnology*, edited by G. Timp (Springer-Verlag, New York, NY, 1999). doi:10.1007/978-1-4612-0531-9

[54]   A. Ulman, Formation and Structure of Self-Assembled Monolayers, Chem. Rev. **96**, 1533 (1996). doi:10.1021/cr9502357

[55]   J. Telegdi, Formation of Self-Assembled Anticorrosion Films on Different Metals, Materials **13**, (2020). doi:10.3390/ma13225089

[56]   G. A. Somorjai and Y. Li, *Introduction to Surface Chemistry and Catalysis*, 2nd ed., (Wiley, Hoboken, NJ, 2010).

[57]   K. W. Kolasinski, *Surface Science: Foundations of Catalysis and Nanoscience*, 4th ed., (Wiley, Hoboken, NJ, USA, 2020).

[58]   L. Qi, H. Tian, and H.-Z. Yu, Binary Thiolate DNA/Ferrocenyl Self-Assembled Monolayers on Gold: A Versatile Platform for Probing Biosensing Interfaces, Anal. Chem. **90**, 9174 (2018). doi:10.1021/acs.analchem.8b01655

[59]   T. Ito, H. Coceancigh, Y. Yi, J. N. Sharma, F. C. Parks, and A. H. Flood, Nanoporous Thin Films Formed from Photocleavable Diblock Copolymers on Gold Substrates Modified

with Thiolate Self-Assembled Monolayers, Langmuir **36**, 9259 (2020). doi:10.1021/acs.langmuir.0c01572

[60]   S. Brown, J. D. Sayler, and S. J. Sibener, Influence of Structural Dynamics on the Kinetics of Atomic Hydrogen Reactivity with Low-Temperature Alkanethiolate Self-Assembled Monolayers, J. Phys. Chem. C **125**, 24406 (2021). doi:10.1021/acs.jpcc.1c07487

[61]   A. Asyuda, S. Das, and M. Zharnikov, Thermal Stability of Alkanethiolate and Aromatic Thiolate Self-Assembled Monolayers on Au(111): An X-ray Photoelectron Spectroscopy Study, J. Phys. Chem. C **125**, 21754 (2021). doi:10.1021/acs.jpcc.1c06984

[62]   R. Urcuyo, E. Cortés, A. A. Rubert, G. Benitez, M. L. Montero, N. G. Tognalli, A. Fainstein, M. E. Vela, and R. C. Salvarezza, Aromatic and Aliphatic Thiol Self-Assembled Monolayers on Au: Anchoring and Delivering Copper Species, J. Phys. Chem. C **115**, 24707 (2011). doi:10.1021/jp207875g

[63]   L. V. Protsailo, W. R. Fawcett, D. Russell, and R. L. Meyer, Electrochemical Characterization of the Alkaneselenol-Based SAMs on Au(111) Single Crystal Electrode, Langmuir **18**, 9342 (2002). doi:10.1021/la0203483

[64]   J. Ossowski *et al.*, Thiolate Versus Selenolate: Structure, Stability, and Charge Transfer Properties, ACS Nano **9**, 4508 (2015). doi:10.1021/acsnano.5b01109

[65]   J. Ossowski, J. Rysz, A. Terfort, and P. Cyganik, Relative Stability of Thiolate and Selenolate SAMs on Ag(111) Substrate Studied by Static SIMS. Oscillation in Stability of Consecutive Chemical Bonds, J. Phys. Chem. C **121**, 459 (2017). doi:10.1021/acs.jpcc.6b10762

[66]   T. M. Owens, B. J. Ludwig, D. R. Fosnacht, J. M. Bartolin, N. Homann, N. J. Wells, B. G. Orr, and M. M. Banaszak Holl, Octylgermane on Gold: Synthesis, Oxidation, and Pattern Formation, Langmuir **20**, 11422 (2004). doi:10.1021/la0490846

[67]   S.-H. Song, P. Koelsch, T. Weidner, M. S. Wagner, and D. G. Castner, Sodium Dodecyl Sulfate Adsorption onto Positively Charged Surfaces: Monolayer Formation with Opposing Headgroup Orientations, Langmuir **29**, 12710 (2013). doi:10.1021/la401119p

[68]   Z. Wang, J. Chen, S. Oyola-Reynoso, and M. Thuo, Empirical Evidence for Roughness-Dependent Limit in Observation of Odd–Even Effect in Wetting Properties of Polar Liquids on n-Alkanethiolate Self-Assembled Monolayers, Langmuir **32**, 8230 (2016). doi:10.1021/acs.langmuir.6b02159

[69] S. W. Han, S. J. Lee, and K. Kim, Self-Assembled Monolayers of Aromatic Thiol and Selenol on Silver: Comparative Study of Adsorptivity and Stability, Langmuir **17**, 6981 (2001). doi:10.1021/la010464q

[70] J. Rechmann, M. Krzywiecki, and A. Erbe, Carbon–Sulfur Bond Cleavage During Adsorption of Octadecane Thiol to Copper in Ethanol, Langmuir **35**, 6888 (2019). doi:10.1021/acs.langmuir.9b00686

[71] D.-Q. Zhang, X.-M. He, Q.-R. Cai, L.-X. Gao, and G. S. Kim, pH and Iodide Ion Effect on Corrosion Inhibition of Histidine Self-Assembled Monolayer on Copper, Thin Solid Films **518**, 2745 (2010). doi:10.1016/j.tsf.2009.10.150

[72] Y. Qiang, H. Li, and X. Lan, Self-Assembling Anchored Film Basing on Two Tetrazole Derivatives for Application to Protect Copper in Sulfuric Acid Environment, J. Mater. Sci. Technol. **52**, 63 (2020). doi:10.1016/j.jmst.2020.04.005

[73] G. Kumar, C.-H. Lien, M. J. Janik, and J. W. Medlin, Catalyst Site Selection Via Control over Noncovalent Interactions in Self-Assembled Monolayers, ACS Catal. **6**, 5086 (2016). doi:10.1021/acscatal.6b01074

[74] H. Solodenko, P. Stender, and G. Schmitz, Atom Probe Study of 1-Octadecanethiol Self-Assembled Monolayers on Platinum (111) and (200) Surfaces, Microsc. Microanal., 1 (2021). doi:10.1017/S1431927621012654

[75] K. Senthil kumar, L. Jiang, and C. A. Nijhuis, Fabrication of Ultra-Smooth and Oxide-Free Molecule-Ferromagnetic Metal Interfaces for Applications in Molecular Electronics under Ordinary Laboratory Conditions, RSC Adv. **7**, 14544 (2017). doi:10.1039/C6RA27280K

[76] G. Mani, D. M. Johnson, D. Marton, V. L. Dougherty, M. D. Feldman, D. Patel, A. A. Ayon, and C. M. Agrawal, Stability of Self-Assembled Monolayers on Titanium and Gold, Langmuir **24**, 6774 (2008). doi:10.1021/la8003646

[77] Y. Feng, S. Chen, J. You, and W. Guo, Investigation of Alkylamine Self-Assembled Films on Iron Electrodes by SEM, FT-IR, EIS and Molecular Simulations, Electrochim. Acta **53**, 1743 (2007). doi:10.1016/j.electacta.2007.08.035

[78] Y. Paz, Self-Assembled Monolayers and Titanium Dioxide: From Surface Patterning to Potential Applications, Beilstein J. Nanotechnol. **2**, 845 (2011). doi:10.3762/bjnano.2.94

[79]   A. Raman, R. Quiñones, L. Barriger, R. Eastman, A. Parsi, and E. S. Gawalt, Understanding Organic Film Behavior on Alloy and Metal Oxides, Langmuir **26**, 1747 (2010). doi:10.1021/la904120s

[80]   C. E. Taylor and D. K. Schwartz, Octadecanoic Acid Self-Assembled Monolayer Growth at Sapphire Surfaces, Langmuir **19**, 2665 (2003). doi:10.1021/la026218b

[81]   H. S. Kato, S. Yoshimoto, A. Ueda, S. Yamamoto, Y. Kanematsu, M. Tachikawa, H. Mori, J. Yoshinobu, and I. Matsuda, Strong Hydrogen Bonds at the Interface between Proton-Donating and -Accepting Self-Assembled Monolayers on Au(111), Langmuir **34**, 2189 (2018). doi:10.1021/acs.langmuir.7b03451

[82]   J. Wei, H. Liu, A. R. Dick, H. Yamamoto, Y. He, and D. H. Waldeck, Direct Wiring of Cytochrome C's Heme Unit to an Electrode: Electrochemical Studies, J. Am. Chem. Soc. **124**, 9591 (2002). doi:10.1021/ja025518c

[83]   A. J. Zaitouna and R. Y. Lai, Design and Characterization of a Metal Ion–Imidazole Self-Assembled Monolayer for Reversible Immobilization of Histidine-Tagged Peptides, Chem. Commun. **47**, 12391 (2011). doi:10.1039/C1CC15510E

[84]   C.-S. Chen, K.-N. Chang, Y.-H. Chen, C.-K. Lee, B. Y.-J. Lee, and A. S.-Y. Lee, Development of a Label-Free Impedance Biosensor for Detection of Antibody–Antigen Interactions Based on a Novel Conductive Linker, Biosens. Bioelectron. **26**, 3072 (2011). doi:10.1016/j.bios.2010.11.051

[85]   X. Yang *et al.*, DNA-Modified Liquid Crystal Droplets, Biosensors **12**, 275 (2022). doi:10.3390/bios12050275

[86]   C. Magallanes, B. M. Aguirre, G. A. González, and L. P. Méndez De Leo, Interaction of Aqueous Cu(II) with Carboxylic Acid and Alcohol Terminated Self Assembled Monolayers: Surface and Interfacial Characterization, Surf. Sci. **692**, 121529 (2020). doi:10.1016/j.susc.2019.121529

[87]   V. Ivanova, M. Manolova, and D. Kolb, Palladium and Platinum Deposition onto 4-Mercaptopyridine SAMs, Solid State Phenom. **121-123**, 363 (2007). doi:10.4028/www.scientific.net/SSP.121-123.363

[88]   J. Kochana, K. Starzec, M. Wieczorek, P. Knihnicki, M. Góra, A. Rokicińska, P. Kościelniak, and P. Kuśtrowski, Study on Self-Assembled Monolayer of Functionalized

Thiol on Gold Electrode Forming Capacitive Sensor for Chromium(VI) Determination, J. Solid State Electrochem. **23**, 1463 (2019). doi:10.1007/s10008-019-04236-2

[89]   N. Papaiconomou, I. Billardde, and E. Chaine, Extraction of Iridium(IV) from Aqueous Solutions Using Hydrophilic/Hydrophobic Ionic Liquids, RSC Adv. **4**, 48260 (2014). doi:10.1039/c4ra06991a

[90]   Y. Yan, Q. Wang, Z. Xiang, and Y. Yang, Separation of Pt(IV), Pd(II), Ru(III), and Rh(III) from Chloride Medium Using Liquid–Liquid Extraction with Mixed Imidazolium-Based Ionic Liquids, Sep. Sci. Technol. **53**, 2064 (2018). doi:10.1080/01496395.2018.1440304

[91]   S. V. Verkhoturov, M. J. Eller, R. D. Rickman, S. Della-Negra, and E. A. Schweikert, Single Impacts of C_{60} on Solids: Emission of Electrons, Ions and Prospects for Surface Mapping, J. Phys. Chem. C **114**, 5637 (2010). doi:10.1021/jp9073703

[92]   M. J. Eller, S. V. Verkhoturov, S. Della-Negra, and E. A. Schweikert, SIMS Instrumentation and Methodology for Mapping of Co-Localized Molecules, Rev. Sci. Instrum. **84**, 103706 (2013). doi:10.1063/1.4824199

[93]   M. J. Eller, S. V. Verkhoturov, and E. A. Schweikert, Testing Molecular Homogeneity at the Nanoscale with Massive Cluster Secondary Ion Mass Spectrometry, Anal. Chem. **88**, 7639 (2016). doi:10.1021/acs.analchem.6b01466

[94]   C.-K. Liang, Doctor of Philosophy Thesis, Texas A&M University (2014), available at https://hdl.handle.net/1969.1/153571.

[95]   M. J. Eller, Doctor of Philosophy Thesis, Texas A&M University (2012), available at https://hdl.handle.net/1969.1/148366.

[96]   S. Verkhoturov, S. Geng, B. Czerwinski, A. Young, and A. Delcorte, Single Impacts of keV Fullerene Ions on Free Standing Graphene: Emission of Ions and Electrons from Confined Volume, J. Chem. Phys. **143**, 164302 (2015). doi:10.1063/1.4933310

[97]   N. Fairley, *CasaXPS Manual 2.3.15: Introduction to XPS and AES*, (Casa Software Ltd., 2009).

[98]   N. Fairley, *CasaXPS Manual 2.3.15: CasaXPS Processing Software for XPS Spectra*, (Casa Software Ltd., 2009).

[99]   T. M. Willey, A. L. Vance, T. van Buuren, C. Bostedt, L. J. Terminello, and C. S. Fadley, Rapid Degradation of Alkanethiol-Based Self-Assembled Monolayers on Gold in Ambient Laboratory Conditions, Surf. Sci. **576**, 188 (2005). doi:10.1016/j.susc.2004.12.022

[100] M. Prato, R. Moroni, F. Bisio, R. Rolandi, L. Mattera, O. Cavalleri, and M. Canepa, Optical Characterization of Thiolate Self-Assembled Monolayers on Au(111), J. Phys. Chem. C **112**, 3899 (2008). doi:10.1021/jp711194s

[101] C. D. Bain, E. B. Troughton, Y. T. Tao, J. Evall, G. M. Whitesides, and R. G. Nuzzo, Formation of Monolayer Films by the Spontaneous Assembly of Organic Thiols from Solution onto Gold, J. Am. Chem. Soc. **111**, 321 (1989). doi:10.1021/ja00183a049

[102] R. R. Greenberg, P. Bode, and E. A. De Nadai Fernandes, Neutron Activation Analysis: A Primary Method of Measurement, Spectrochim. Acta B: At. Spectrosc. **66**, 193 (2011). doi:10.1016/j.sab.2010.12.011

[103] B. N. Johnson and R. Mutharasan, Regeneration of Gold Surfaces Covered by Adsorbed Thiols and Proteins Using Liquid-Phase Hydrogen Peroxide-Mediated UV-Photooxidation, J. Phys. Chem. C **117**, 1335 (2013). doi:10.1021/jp307983e

[104] MilliporeSigma, *1-(11-Mercaptoundecyl)imidazole,* 723088, available at https://www.sigmaaldrich.com/US/en/product/aldrich/723088.

[105] MilliporeSigma, *12-Mercaptododecanoic acid,* 675067, available at https://www.sigmaaldrich.com/US/en/product/aldrich/675067?gclid=CjwKCAjwlqOXBh BqEiwA-hhitPEthpnY5KuVC6gh4vfT8I6OFWR2QMja2e6Jq8nR8yQP95HXD5s5choCZAMQAv D_BwE.

[106] S. Yamamoto *et al.*, Direct Evidence of Interfacial Hydrogen Bonding in Proton-Electron Concerted 2D Organic Bilayer on Au Substrate, e-J. Surf. Sci. Nanotechnol. **17**, 49 (2019). doi:10.1380/ejssnt.2019.49

[107] H. Kusawake, T. Saito, A. Yokoyama, K. Takesako, N. Takahashi, H. Baba, Y. Ohkubo, and A. Shinohara, Angular-Momentum Effect in the Fusion Reaction of ^{141}Pr with ^{40}Ar Projectiles, Radiochim. Acta **69**, 65 (1995). doi:10.1524/ract.1995.69.2.65

[108] B. Singh, Nuclear Data Sheets for A = 172, Nucl. Data Sheets **75**, 199 (1995). doi:10.1006/ndsh.1995.1025

[109] H. Gauvin, Y. Le Beyec, and N. T. Porile, Nuclear Reactions of ^{118}Sn, ^{121}Sb, and ^{127}I with Argon Ions, Nucl. Phys. A **223**, 103 (1974). doi:10.1016/0375-9474(74)90279-6

[110] B. Singh, Nuclear Data Sheets for A=149, Nucl. Data Sheets **102**, 1 (2004). doi:10.1016/j.nds.2004.05.001

[111] A. N. Andreev, D. D. Bogdanov, A. V. Eremin, A. P. Kabachenko, Y. A. Muzychka, O. A. Orlova, B. I. Pustyl'nik, G. M. Ter-Akop'yan, V. I. Chepigin, and S. Sharo, Cross Sections for Production of Neutron-Deficient Isotopes of At and Po in Ho+Ar, Tb+Ca, and Ta+Mg Reactions, Yad. Fiz. **52**, 640 (1990).

[112] H. Xiaolong, Nuclear Data Sheets for A = 196, Nucl. Data Sheets **108**, 1093 (2007). doi:10.1016/j.nds.2007.05.001

[113] *Target Ladders*, retrieved 3 August 2022, available at https://cyclotron.tamu.edu/folden/media/.

[114] W. Parker and R. Falk, Molecular Plating: A Method for the Electrolytic Formation of Thin Inorganic Films, Nucl. Instrum. Methods **16**, 355 (1962). doi:10.1016/0029-554X(62)90142-8

[115] W. Parker, H. Bildstein, N. Getoff, H. Fischer-Colbrie, and H. Regal, Molecular Plating II a Rapid and Quantitative Method for the Electrodeposition of the Rare-Earth Elements, Nucl. Instrum. Methods **26**, 61 (1964). doi:10.1016/0029-554X(64)90050-3

[116] D. C. Aumann and G. Müllen, Preparation of Targets of Ca, Ba, Fe, La, Pb, Tl, Bi, Th and U by Electrodeposition from Organic Solutions, Nucl. Instrum. Methods **115**, 75 (1974). doi:10.1016/0029-554X(74)90427-3

[117] D. A. Mayorov, E. E. Tereshatov, T. A. Werke, M. M. Frey, and C. M. Folden III, Heavy-Ion Beam Induced Effects in Enriched Gadolinium Target Films Prepared by Molecular Plating, Nucl. Instrum. Methods Phys. Res. B **407**, 256 (2017). doi:10.1016/j.nimb.2017.07.012

[118] A. Ghiorso, Recoil Spectrometer for the Detection of Single Atoms, J. Radioanal. Nucl. Chem. **124**, 407 (1988). doi:10.1007/BF02041331

[119] A. Ghiorso, S. Yashita, M. E. Leino, L. Frank, J. Kalnins, P. Armbruster, J. P. Dufour, and P. K. Lemmertz, Sassy, a Gas-Filled Magnetic Separator for the Study of Fusion Reaction Products, Nucl. Instrum. Methods Phys. Res. A: Accel. Spectrom. Detect. Assoc. Equip. **269**, 192 (1988). doi:10.1016/0168-9002(88)90877-7

[120] J. J. Ressler *et al.*, SASSYER: An Old Instrument for New Physics at Yale, Nucl. Instrum. Methods Phys. Res. B **204**, 141 (2003). doi:10.1016/S0168-583X(02)01906-7
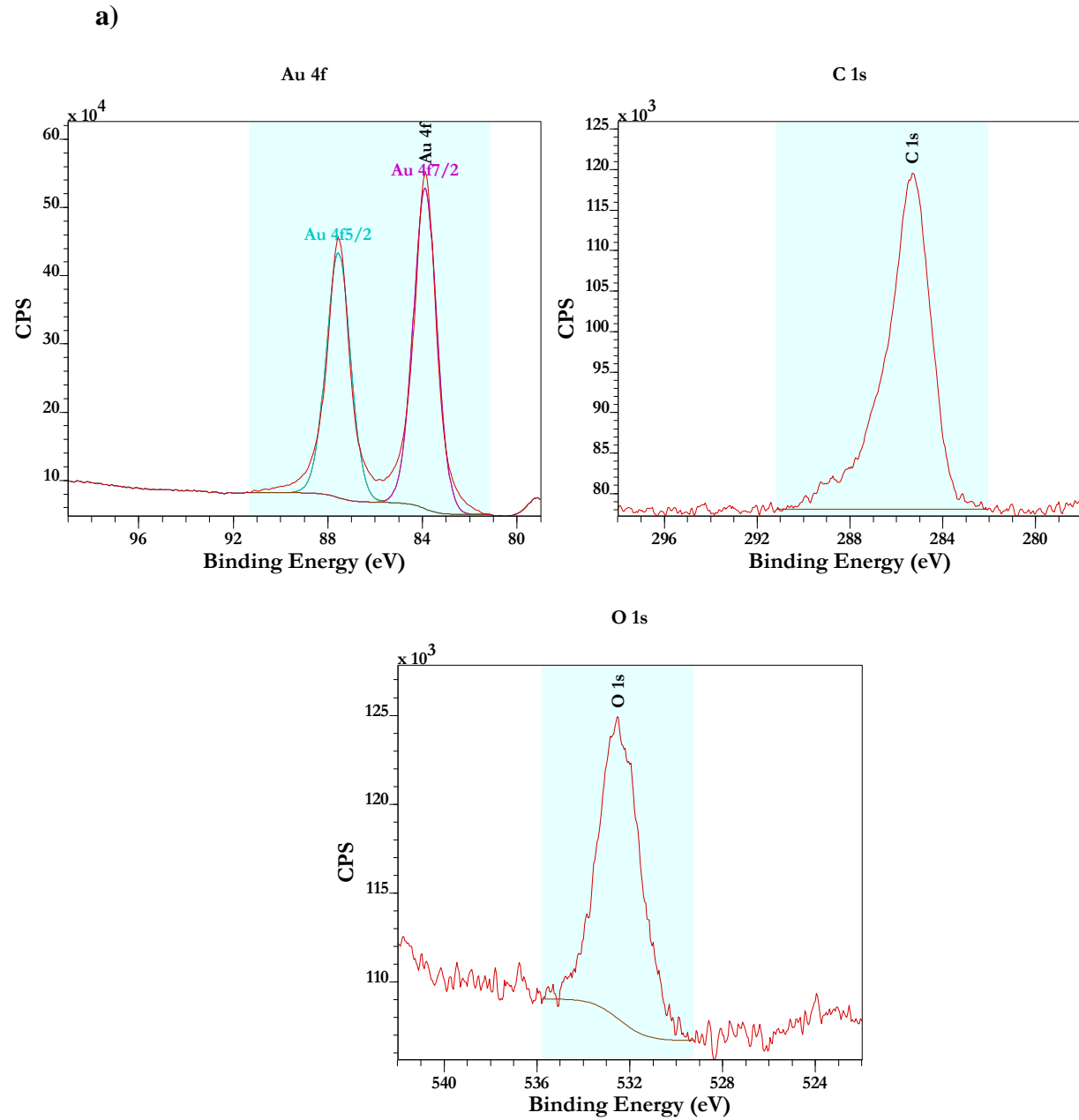
[121] C. M. Folden III, *Characterization of the Aggie Gas-Filled Separator*, Cyclotron Institute, Texas A&M University (2020-2021, unpublished), available at https://cyclotron.tamu.edu/progress-reports/2020-2021/2%20Heavy%20Ion%20Reactions/II_12_13_folden_Characterization%20of%20the%20AGGIE%20gas-filled%20separator.pdf.

[122] R. Yan, A. Terfort, and M. Zharnikov, Modification of Alkanethiolate Self-Assembled Monolayers by Ultraviolet Light: The Effect of Wavelength, J. Phys. Chem. C **125**, 1855 (2021). doi:10.1021/acs.jpcc.0c09438

[123] N. J. Brewer, S. Janusz, K. Critchley, S. D. Evans, and G. J. Leggett, Photooxidation of Self-Assembled Monolayers by Exposure to Light of Wavelength 254 nm: A Static SIMS Study, J. Phys. Chem. B **109**, 11247 (2005). doi:10.1021/jp0443299

[124] L. Houssiau and P. Bertrand, TOF–SIMS Study of Alkanethiol Adsorption and Ordering on Gold, Appl. Surf. Sci. **175–176**, 399 (2001). doi:10.1016/S0169-4332(01)00132-5

[125] T. L. Barr and S. Seal, Nature of the Use of Adventitious Carbon as a Binding Energy Standard, J. Vac. Sci. Technol. A **13**, 1239 (1995). doi:10.1116/1.579868

[126] F. Mangolini, J. B. McClimon, F. Rose, and R. W. Carpick, Accounting for Nanometer-Thick Adventitious Carbon Contamination in X-ray Absorption Spectra of Carbon-Based Materials, Anal. Chem. **86**, 12258 (2014). doi:10.1021/ac503409c

[127] C.-K. Liang, S. Verkhoturov, and L.-J. Chen, Size-Dependent Emission of Negative Ions from Gold Nanoparticles Bombarded with C_{60} and Au_{400}, Int. J. Mass Spectrom. **334**, 43 (2013). doi:10.1016/j.ijms.2012.10.003

[128] M. A. Park, K. A. Gibson, K. Quinones, and M. A. Schweikert, Coincidence Counting in Time-of-Flight Mass Spectrometry: A Test for Chemical Microhomogeneity, Science **248**, 988 (1990). doi:10.1126/science.248.4958.988

[129] D. S. Verkhoturov, B. P. Crulhas, M. J. Eller, Y. D. Han, S. V. Verkhoturov, Y. Bisrat, A. Revzin, and E. A. Schweikert, Nanoprojectile Secondary Ion Mass Spectrometry for Analysis of Extracellular Vesicles, Anal. Chem. **93**, 7481 (2021). doi:10.1021/acs.analchem.1c00689

[130] M. J. Eller, J. M. Sandoval, S. V. Verkhoturov, and E. A. Schweikert, Nanoprojectile Secondary Ion Mass Spectrometry for Nanometrology of Nanoparticles and Their Interfaces, Anal. Chem. **94**, 7868 (2022). doi:10.1021/acs.analchem.2c00303

[131] M. Zharnikov and M. Grunze, Modification of Thiol-Derived Self-Assembling Monolayers by Electron and X-ray Irradiation: Scientific and Lithographic Aspects, J. Vac. Sci. Technol. B **20**, 1793 (2002). doi:10.1116/1.1514665

[132] *XPS Reference Table of Elements*, retrieved 19 April 2022, available at https://www.jp.xpssimplified.com/elements/sulfur.php.

[133] V. Feyer, O. Plekan, S. Ptasińska, M. Iakhnenko, N. Tsud, and K. C. Prince, Adsorption of Histidine and a Histidine Tripeptide on Au(111) and Au(110) from Acidic Solution, J. Phys. Chem. C **116**, 22960 (2012). doi:10.1021/jp307463z

[134] D. A. Offord, S. B. Sachs, M. S. Ennis, T. A. Eberspacher, J. H. Griffin, C. E. D. Chidsey, and J. P. Collman, Synthesis and Properties of Metalloporphyrin Monolayers and Stacked Multilayers Bound to an Electrode Via Site Specific Axial Ligation to a Self-Assembled Monolayer, J. Am. Chem. Soc. **120**, 4478 (1998). doi:10.1021/ja973528l

[135] Z. Safaei, A. Shiroudi, E. Zahedi, and M. Sillanpää, Atmospheric Oxidation Reactions of Imidazole Initiated by Hydroxyl Radicals: Kinetics and Mechanism of Reactions and Atmospheric Implications, Phys. Chem. Chem. Phys. **21**, 8445 (2019). doi:10.1039/C9CP00632J

[136] E. Cortés, A. A. Rubert, G. Benitez, P. Carro, M. E. Vela, and R. C. Salvarezza, Enhanced Stability of Thiolate Self-Assembled Monolayers (SAMs) on Nanostructured Gold Substrates, Langmuir **25**, 5661 (2009). doi:10.1021/la804251a

[137] G. Yang, N. A. Amro, Z. B. Starkewolfe, and G. Y. Liu, Molecular-Level Approach to Inhibit Degradations of Alkanethiol Self-Assembled Monolayers in Aqueous Media, Langmuir **20**, 3995 (2004). doi:10.1021/la0499160

[138] R. K. Gupta, M. P. Srinivasan, and R. Dharmarajan, Synthesis of 16-Mercaptohexadecanoic Acid Capped Gold Nanoparticles and their Immobilization on a Substrate, Mater. Lett. **67**, 315 (2012). doi:10.1016/j.matlet.2011.09.047

[139] J. A. Woollam Co. Inc., in *CompleteEASE^{TM} Data Analysis Manual* (2011).

[140] *Ellipsometry Tutorial*, retrieved 4 March 2021, available at https://www.jawoollam.com/resources/ellipsometry-tutorial.

[141] S. F. Mughabghab, Thermal Neutron Capture Cross Sections Resonance Integrals and G-Factors (2003), available at https://www.osti.gov/etdeweb/servlets/purl/20332542.
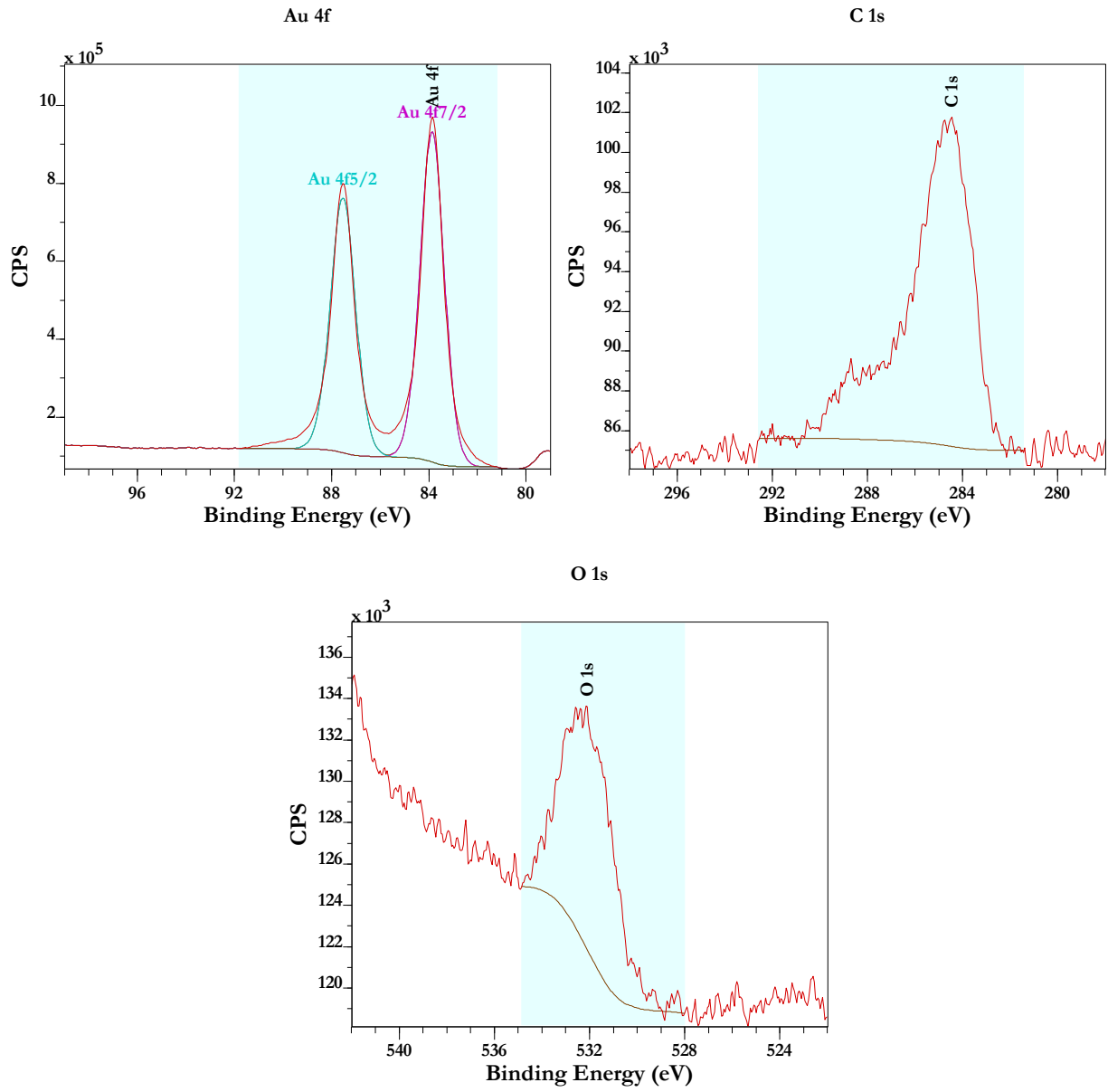
[142] J. Blachot, Nuclear Data Sheets for A = 104, Nucl. Data Sheets **108**, 2035 (2007). doi:10.1016/j.nds.2007.09.001

[143] C. M. Baglin, Nuclear Data Sheets for A = 192, Nucl. Data Sheets **113**, 1871 (2012). doi:10.1016/j.nds.2012.08.001

[144] S. Götz *et al.*, Rapid Extraction of Short-Lived Isotopes from a Buffer Gas Cell for Use in Gas-Phase Chemistry Experiments, Part II: On-Line Studies with Short-Lived Accelerator-Produced Radionuclides, Nucl. Instrum. Methods Phys. Res. B **507**, 27 (2021). doi:10.1016/j.nimb.2021.09.004

[145] N. Nica, Nuclear Data Sheets for A = 148, Nucl. Data Sheets **117**, 1 (2014). doi:10.1016/j.nds.2014.02.001

[146] H. Xiaolong and Z. Chunmei, Nuclear Data Sheets for A=197, Nucl. Data Sheets **104**, 283 (2005). doi:10.1016/j.nds.2005.01.001

[147] H. Xiaolong and K. Mengxiao, Nuclear Data Sheets for A = 195, Nucl. Data Sheets **121**, 395 (2014). doi:10.1016/j.nds.2014.09.003

[148] C. M. Baglin, E. A. McCutchan, S. Basunia, and E. Browne, Nuclear Data Sheets for A=170, Nucl. Data Sheets **153**, 1 (2018). doi:10.1016/j.nds.2018.11.001

[149] C. M. Baglin, Nuclear Data Sheets for A = 169, Nucl. Data Sheets **109**, 2033 (2008). doi:10.1016/j.nds.2008.08.001

[150] C. M. Baglin and E. A. McCutchan, Nuclear Data Sheets for A=171, Nucl. Data Sheets **151**, 334 (2018). doi:10.1016/j.nds.2018.08.002

[151] E. Browne and J. K. Tuli, Nuclear Data Sheets for A = 145, Nucl. Data Sheets **110**, 507 (2009). doi:10.1016/j.nds.2009.02.001
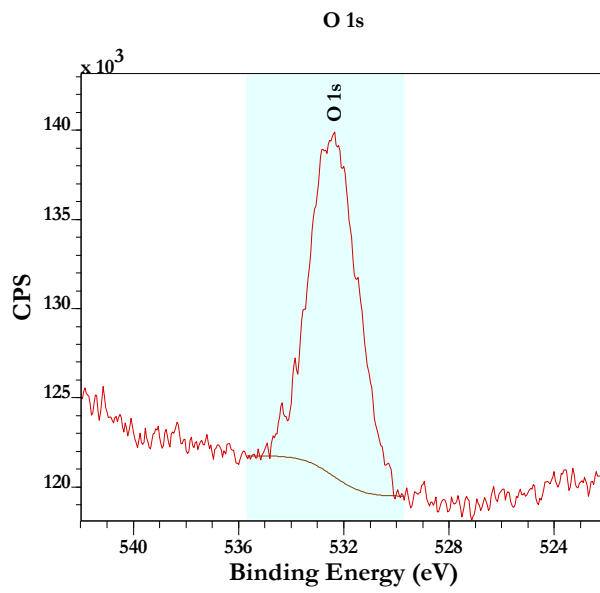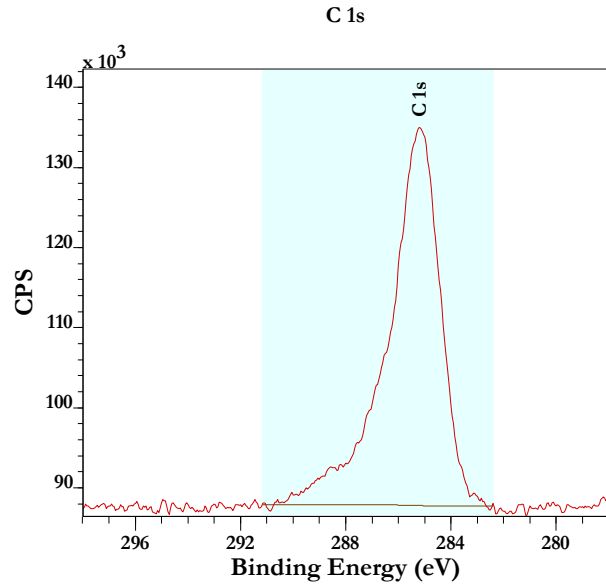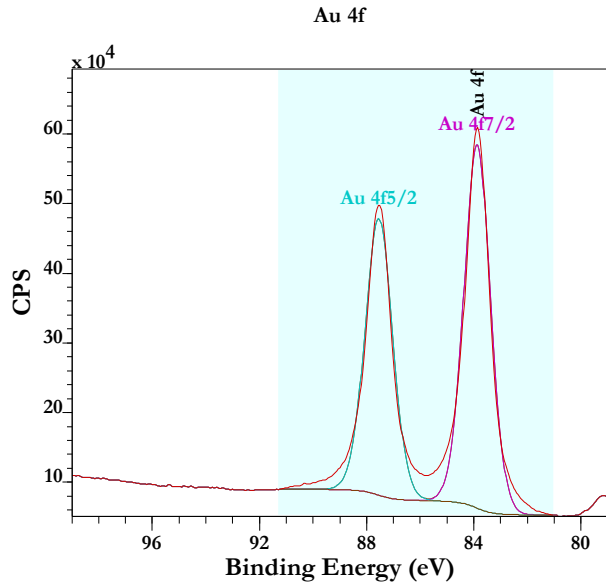
APPENDIX

The results of the XPS analysis are described in Section 3.1.3. Additional XPS spectra are presented below.

a)

b)

Au 4f

C 1s

O 1s

c)

d)

Au 4f

Au 4f

Au 4f7/2

Au 4f5/2

CPS

$70_{\_}$ x 10^4

60

50

40

30

20

10

96   92   88   84   80

Binding Energy (eV)

C 1s

C 1s

x 10^3

140

135

130

125

120

115

110

105

100

95

90

CPS

296   292   288   284   280

Binding Energy (eV)

O 1s

O 1s

x 10^3

140

135

130

125

120

CPS

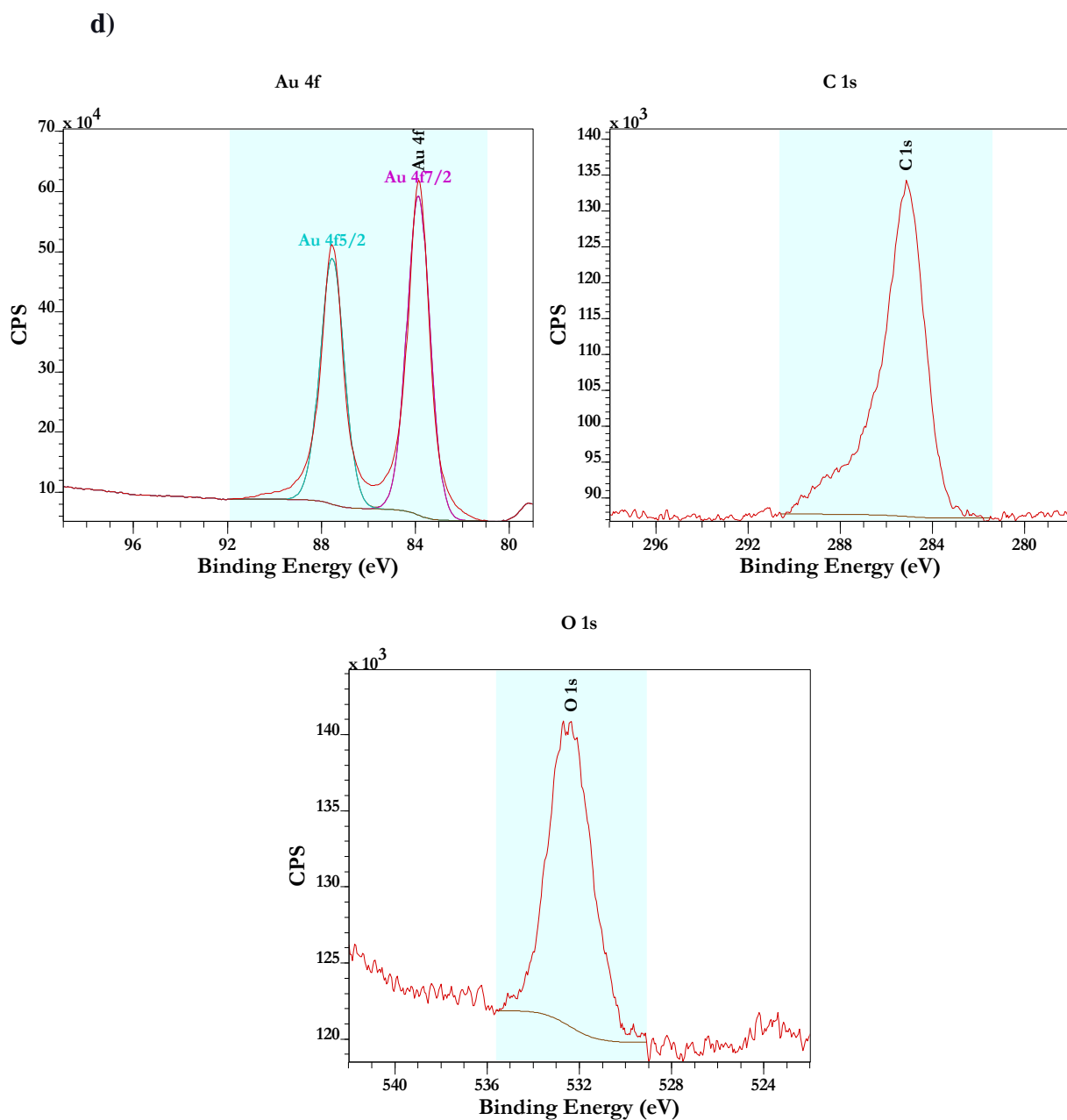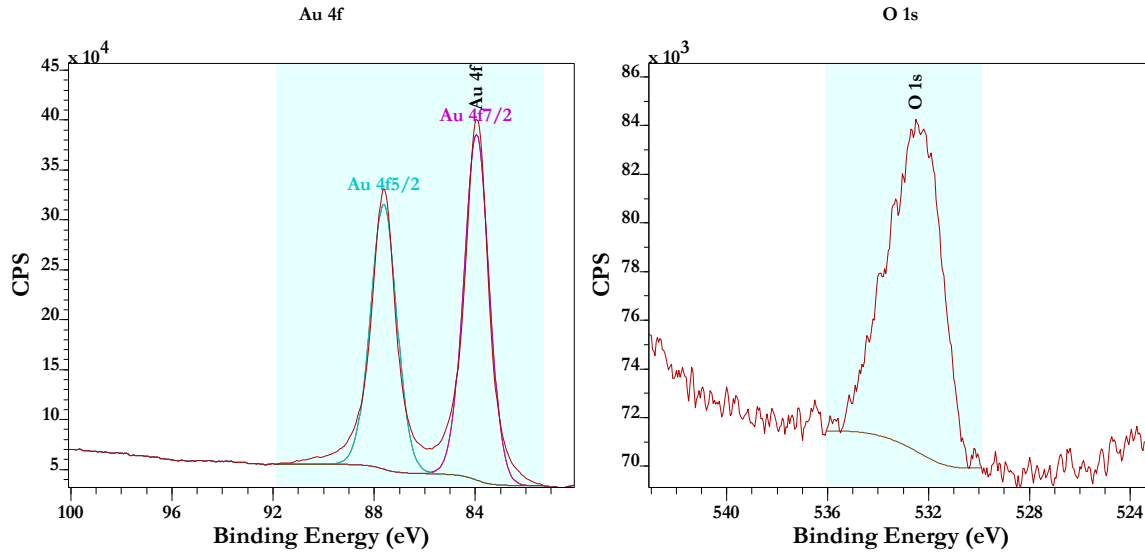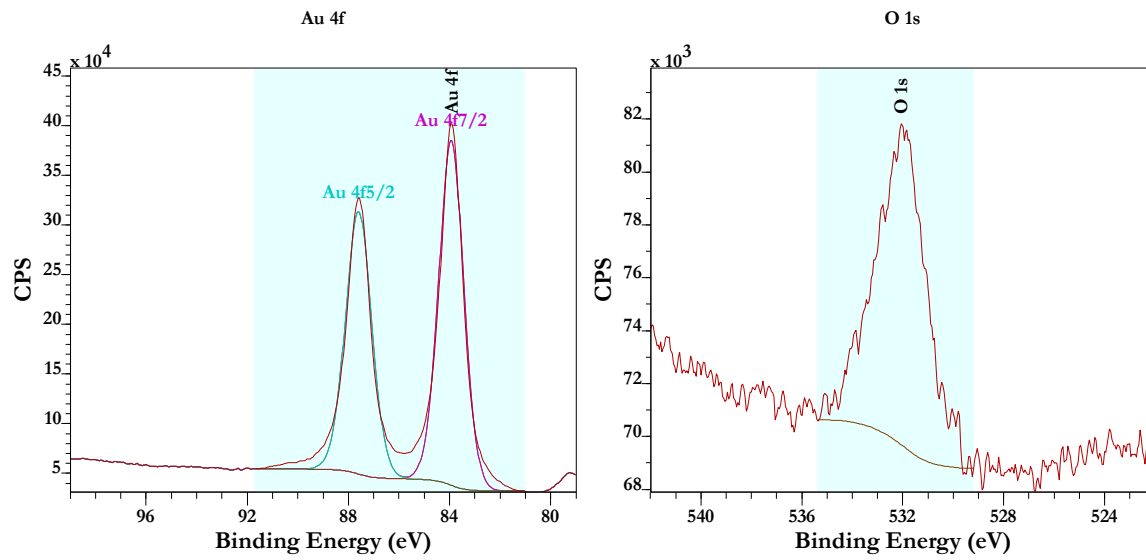540   536   532   528   524

Binding Energy (eV)

Figure A1. Gold 4f, carbon 1s, and oxygen 1s XPS for Im-C_{11}-SH SAMs on precleaned Au; one SAMs deposition: (a) the freshly prepared SAMs; (b) SAMs removed using the liquid-UVPO treatment; (c) the freshly prepared sample stored for two weeks; (d) the freshly prepared sample stored for one month.
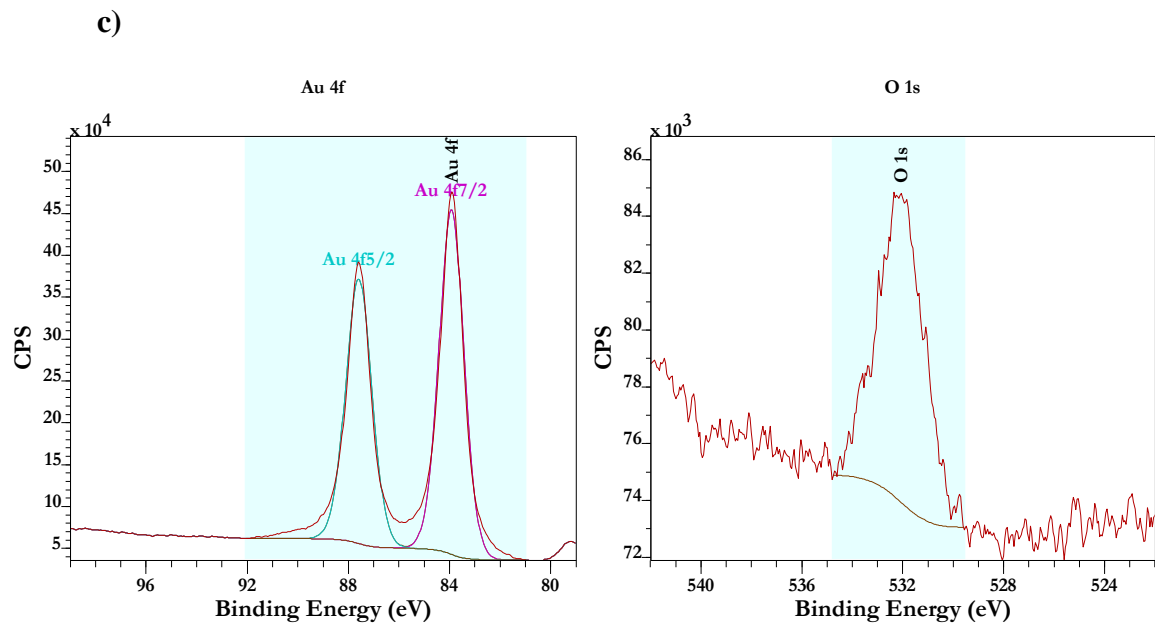
c)

Figure A2. Gold 4f and oxygen 1s XPS for MDDA SAMs on precleaned Au; one SAMs deposition: (a) the freshly prepared SAMs; (b) the freshly prepared sample stored for one week; (c) the freshly prepared sample stored for one month.

Vira ZAKUSILOVA

Characterization and Application of Alkanethiolate Self-Assembled Monolayers on Gold-Coated Silicon Detectors for the Metal Sorption

Résumé

Cette thèse contribue aux développements pour les futures expériences visant l'élément 109, le meitnerium. Elle porte sur la préparation de silice fonctionnalisée et son application pour la séparation des éléments. Ces matériaux qu'imitent des détecteurs au silicium permettront de comparer la réactivité du meitnerium et de ses homologues, l'Ir et le Rh, vis-à-vis de ces surfaces lors d'expériences on-line. Pour la fonctionnalisation, nous avons employé la méthodologie basée sur la formation de monocouches auto-assemblée d'organothiols, le 1-(11-mercaptoundécyl)imidazole et l'acide 12-mercaptododécanoïque. Nous avons démontré que ces monocouches obtenues sont stables au moins pendant un mois et leur surface est saturée après l'absorption de l'Ir(IV) et Rh(III) à partir de solution aqueuse acide. La deuxième partie de la thèse porte sur l'étude de la sorption de l'Ir, l'erbium et l'astate sur les surfaces de matériaux préparés lors des expériences au cyclotron. Les résultats démontrent que la position du détecteur et son revêtement jouent un rôle important.

Mots-clés: Silice fonctionnalisée, Monocouches auto-assemblées d'organothiols, Sorption de l'iridium et le rhodium, Expériences on-line au cyclotron

Résumé en anglais

In this work, thiolate-functionalized gold-coated silicon detectors were proposed as new materials for the comparison of the sorption properties of superheavy elements and their lighter homologs produced during online cyclotron-based experiments. The first part of the dissertation discusses the functionalization of gold-coated silicon substrates with 1-(11-mercaptoundecyl)imidazole and 12-mercaptododecanoic acid self-assembled monolayers. The functionalized surfaces were characterized offline utilizing several surface science techniques. The successful results showed the studied substrates are stable for at least one month and demonstrate the surface saturation with Ir(IV) and Rh(III) adsorbed from hydrochloric acid solutions. The second part of the dissertation discusses the new detector setup developed to study the sorption of online-produced Ir, Er, and At. The promising results demonstrated the role of the detector position and its coating on the element sorption.

Keywords: Functionalized silicon, Self-assembled monolayers of organothiols, Sorption of iridium and rhodium, Online cyclotron-based experiments